

©2008

Leonard Alexander Kahl, Jr.

ALL RIGHTS RESERVED

PHYTOPLANKTON PHYSIOLOGY AND EXPORT FLUX

By

LEONARD ALEXANDER KAHL, JR.

A Dissertation submitted to the  
Graduate School-New Brunswick  
Rutgers, The State University of New Jersey  
in partial fulfillment of the requirements

for the degree of

Doctor of Philosophy

Graduate Program in Oceanography

written under the direction of

Oscar Schofield

and approved by

---

Oscar Schofield

---

Paul G. Falkowski

---

Robert Chant

---

Hans G. Dam

---

Zoe V. Finkel

---

Richard D. Ludescher

New Brunswick, New Jersey  
October, 2008

## ABSTRACT OF THE DISSERTATION

Phytoplankton Physiology and Export Flux

by

Leonard Alexander Kahl, Jr.

Dissertation Director:

Oscar Schofield

The oceanic biological pump represents one of the Earth's major carbon sinks for atmospheric CO<sub>2</sub> and is primarily driven by the flocculation in, and subsequent sedimentation of phytoplankton from the sea surface. Sticking efficiency, crucial to flocculation processes, was estimated within a laboratory mesocosm mimicking energy levels in the ocean on a calm day. The sticking efficiency of the diatom *Thalassiosira pseudonana* varied as a result of physiological state. During the periods of high sticking efficiency, physiological changes included: (1) diminished phytoplankton photosynthetic quantum efficiency, (2) an increase in super-oxide dismutase protein expression, reflecting oxidative stress, and (3) the induction of a biochemical cascade initiating autocatalytic programmed cell death. Additionally, during the period of high physiological stress on the diatoms, there was an increase in the presence of both bacteria and extracellular organic matter. Further study found that as the organic matter exuded by phytoplankton degraded, via breaking of beta-glycoside linkages between polysaccharide monomers, it is transformed from discrete gel-like

structures into a net-like matrix. This transition towards a more net-like organic matrix increases the probability of the formation of more rapidly settling marine aggregates. These results were then applied to a 1-D export flux model which showed the dependence of export flux dynamics on organic matter exuded by phytoplankton. These simulations revealed that a low initial sticking efficiency allows a significant increase in the critical concentration of algal cells. Such an increase in the number of cells during bloom initiation, when followed by an increase in sticking efficiency during the maintenance and senescent phases, resulted in enhanced and pulse-like carbon export events. Organic matter exuded by phytoplankton also increases seawater viscosity resulting in a 7-25% decrease in export flux. This decrease in export flux results from a convergence of settling speeds between large and small particles as viscosity increases, reducing coagulation due to differential settling. Furthermore, coupling a 1-D export model with a mechanistic model of phytoplankton physiology and cellular exudation, driven by typical oceanic light and nutrient regimes, showed that cell size provides considerable control over the mechanisms controlling the flux of particulate carbon from the sea surface.

## **Preface and Acknowledgements**

The idea for this thesis was hatched during a car-ride to the Rutgers field station in Tuckerton, New Jersey in late 2003 with Oscar. Without his mentorship, support, and trust, this thesis would never have been completed. By the time we published the first chapter of this thesis along with Assaf Vardi and Oscar (Kahl et al. 2008), we found ourselves in the midst of more questions than at the beginning. For much of the physics-oriented work in the first chapter I am thankful that Bob Chant willingly provided guidance. Also during that time, my officemates Tuo Shi, Matt Oliver, and Zoe Finkel helped bring me deep into the realm of phytoplankton biogeochemistry. Of those three, Zoe would end up becoming interested enough to serve on this thesis committee and offer some of the most keen and constructive insights for this work. Moreover, the other outside committee member Hans Dam kindly loaned an instrument from his lab without reservation or strings attached. And, in addition to traveling to New Jersey for each of my thesis presentations, he provided a rich body of knowledge regarding the inner workings of the early research into phytoplankton exudates. Exploration into and characterization of such exudates would not have been possible without the help of Rick Ludescher from the Food Science department. His willingness to sit down and discuss natural polymers was essential for

exploring the fundamental nature of phytoplankton exudates. Of course this thesis could not have been completed without Paul's insistence that I reach out to work with food scientists, nor without his regular queries as to my progress. Others who were instrumental in executing the lab work described in this thesis are; Kevin Wyman, Char Fuller, Piotr Nawrot, and an exceptional undergraduate assistant, Mike Garzio. Intellectually, Oscar and Paul are a formidable team for one to work with. At times, whether sought or not, the two of them offered the ideal counter-pressure to one another's input on this research, writing, social engineering, politics, and life in general. There is no other place where a young scientist can be embraced by both the future and history of earth science with such a vivid sense of living in the now while working for the benefit of tomorrow. I also thank my closest friend, Bryan Kirk, for his ability to provide reasonable advice and for providing sustained motivation. Finally, the love and support of my parents, Leonard and Lauri, and my grandmother Betsie cannot be overstated. And, without the compassion, companionship, and unwavering devotion to completing this together, I am eternally indebted to Elizabeth.

## Table of Contents

<b>ABSTRACT OF THE DISSERTATION.....</b>	<b>ii</b>
<b>PREFACE AND ACKNOWLEDGEMENTS.....</b>	<b>iv</b>
<b>TABLE OF CONTENTS.....</b>	<b>vi</b>
<b>LIST OF TABLES.....</b>	<b>viii</b>
<b>LIST OF FIGURES.....</b>	<b>ix</b>
<b>INTRODUCTION.....</b>	<b>1</b>
<b>1 THE EFFECT OF PHYSIOLOGY ON EXPORT FLUX.....</b>	<b>5</b>
1.1 BACKGROUND.....	5
1.2 METHODS.....	7
<i>1.2.1 mesocosm design.....</i>	<i>7</i>
<i>1.2.2 mesocosm environment.....</i>	<i>7</i>
<i>1.2.3 particle size distribution.....</i>	<i>10</i>
<i>1.2.4 phytoplankton physiology.....</i>	<i>12</i>
<i>1.2.5 caspase activity.....</i>	<i>13</i>
<i>1.2.6 SOD expression.....</i>	<i>14</i>
<i>1.2.7 TEP abundance.....</i>	<i>14</i>
<i>1.2.8 bacterial abundance.....</i>	<i>15</i>
<i>1.2.9 sticking efficiency.....</i>	<i>16</i>
1.3 RESULTS.....	21

1.4 DISCUSSION.....	30
<i>1.4.1 algal cell physiology and sticking efficiency.....</i>	<i>31</i>
<i>1.4.2 sticking efficiency and export flux.....</i>	<i>38</i>
1.5 TABLES.....	43
1.6 FIGURES.....	47
<b>2 THE NATURE AND ROLE OF PHYTOPLANKTON EXUDATE..</b>	<b>57</b>
2.1 BACKGROUND.....	57
2.2 METHODS.....	58
<i>2.2.1 cell counts.....</i>	<i>60</i>
<i>2.2.2 photosynthetic efficiency.....</i>	<i>60</i>
<i>2.2.3 viscosity.....</i>	<i>61</i>
<i>2.2.4 sticking efficiency.....</i>	<i>62</i>
<i>2.2.5 exudate isolation and characterization.....</i>	<i>64</i>
2.3 RESULTS AND DISCUSSION.....	67
2.4 FIGURES.....	77
<b>3 PHYSIOLOGY AND EXUDATION, A MODEL.....</b>	<b>85</b>
3.1 BACKGROUND.....	85
3.2 MODEL DESCRIPTION.....	87
<i>3.2.1 carbon pathways into and out of the cell.....</i>	<i>87</i>
<i>3.2.2 carbon pathways within the cell.....</i>	<i>90</i>



3.3 RESULTS AND DISCUSSION.....	93
3.4 TABLES.....	100
3.5 FIGURES.....	105
<b>CONCLUSION.....</b>	<b>117</b>
<b>REFERENCES.....</b>	<b>119</b>
<b>CURRICULUM VITAE.....</b>	<b>128</b>

## List of Tables

Table 1.1, Rates of fluid shear and estimated sticking efficiency in phytoplankton aggregation studies.....	43
Table 1.2, Table of mathematical symbols.....	45
Table 1.3, Predicted and measured $C_{CR}$ and a comparison with values estimated from the experiment.....	46
Table 3.1, Table of parameters shown in figure 3.1.....	100
Table 3.2, Table of symbols used in the photosynthesis model.....	102
Table 3.3, Cell model results for large and small cells, each having high and low light and nutrient stress.....	103

Table 3.4, Growth rate ( $\mu$ ) and sticking efficiency ( $\alpha$ ) values used to couple the phytoplankton physiology/exudation model with a 1-D export flux model.....	104
--	-----

## List of Figures

Figure 1.1, A comparison of estimated energy levels during phytoplankton aggregation experiments.....	47
Figure 1.2, Channel cross-section of flow characteristics of the annular flume.....	49
Figure 1.3, Time lapse images of the <i>Thalassiosira pseudonana</i> bloom in the annular flume.....	50
Figure 1.4, Particle size evolution during a <i>Thalassiosira pseudonana</i> mesocosm experiment.....	51
Figure 1.5, Mesocosm measurements of; sticking efficiency, cell concentration, aggregated cell fraction, and bacteria counts.....	52
Figure 1.6, From the same mesocosm, a western blot of S.O.D. protein, sticking efficiency, caspase activity, and photosynthetic efficiency.....	53
Figure 1.7, Volume fraction and volume export flux for a 1-D particle aggregation model.....	54

Figure 1.8, A comparison of biomass export flux.....	55
Figure 2.1, Combined phytoplankton and bacteria cell counts from three <i>Thalassiosira pseudonana</i> batch cultures.....	77
Figure 2.2, Sticking efficiency and excess viscosity.....	78
Figure 2.3, Rheology of <i>Thalassiosira pseudonana</i> exudates.....	80
Figure 2.4, Mass spectrometry spectra of exudates isolated from <i>Thalassiosira pseudonana</i> .....	81
Figure 2.5, Fourier-transform infrared spectroscopy spectra of the exudates isolated from <i>Thalassiosira pseudonana</i> .....	82
Figure 2.6, Atomic Force Microscopy images of <i>Thalassiosira pseudonana</i> exudates.....	83
Figure 2.7, The effective diameter of isolated algal exudates.....	84
Figure 3.1, Box model of the carbon budget for a single cell.....	105
Figure 3.2, The allocation and transfer of intracellular carbon in the cellular box model.....	106
Figure 3.3, Physiology and exudate model results for a large cell with high light and high nutrients.....	107
Figure 3.4, Physiology and exudate model results for a small cell with high light and high nutrients.....	108

Figure 3.5, Physiology and exudate model results for a large cell with low light and high nutrients.....	109
Figure 3.6, Physiology and exudate model results for a small cell with low light and high nutrients.....	110
Figure 3.7, C Physiology and exudate model results for a large cell with high light and low nutrients.....	111
Figure 3.8, Physiology and exudate model results for a small cell with high light and low nutrients.....	112
Figure 3.9, Physiology and exudate model results for a large cell with low light and low nutrients.....	113
Figure 3.10, Physiology and exudate model results for a small cell with low light and low nutrients.....	114
Figure 3.11, Mean particle settling velocity and volume flux spectrum for a simulated bloom in the north central Pacific Ocean.....	115
Figure 3.12, Mean particle settling velocity and volume flux spectrum for a simulated bloom in the tropical Pacific Ocean.....	116

## Introduction

*The wrecks dissolve above us; their dust drops down from afar —  
Down to the dark, to the utter dark, where the blind white sea-snakes are.*

—from “The Deep-Sea Cables”  
by Rudyard Kipling

Over the course of the twentieth century, global industrialization has led to an increase in atmospheric CO<sub>2</sub> which has the potential to alter climate. The capacity of the oceans to absorb and sequester CO<sub>2</sub> is enormous and provides a major repository for removing the increased CO<sub>2</sub> from the atmosphere. As the primary agents of carbon transport to the lithosphere, terrestrial and aquatic plants each account for half of the world’s net primary production (NPP) (Field et al. 1998). The exchange of CO<sub>2</sub> between the atmosphere and the oceans is mediated by two phenomena, the solubility and biological pumps. At the core of the biological pump are primary producers such as phytoplankton; who function as a carbon conduit between the climatically influential atmosphere and carbon-storing lithosphere. The

large percentage of photosynthetic biomass contained within phytoplankton, and their high turnover rate, are two defining characteristics when compared to terrestrial plants. Because photosynthetic biomass is rich in carbon, the high rate of phytoplankton turnover in the surface ocean acts as a simultaneous modulator of 1) aquatic ecosystems and 2) the flux of carbon from the surface to the floor of the sea. Consequently, an increase in oceanic NPP will have the dual effect of increasing food availability at the base of aquatic ecosystems and also increasing the rate of removal of carbon from the earth's atmosphere. However, in such cases the higher order ecosystem responses and ultimate fate of photosynthetically reduced carbon are less than certain.

Because of their substantial role in global primary production, much attention has been focused on the variable yet significant amount of organic carbon produced by phytoplankton in the ocean's surface which is sequestered into the deep sea via the biological pump (Martin et al. 1987). And of this organic carbon, both the particulate (as phytoplankton biomass) and dissolved forms are crucial to efficient carbon sequestration. Indeed, despite the energetic inefficiency of not utilizing all of their photosynthetically – fixed carbon, phytoplankton prodigiously release dissolved organic matter into their surrounding environment. Such organic

matter has been broadly characterized (Leppard 1995) and is widely recognized as playing a crucial role in the formation of sequestration-enhancing marine aggregates such as marine snow (Alldredge et al. 1993; Alldredge and Silver 1988).

Dissolved organic carbon, when derived from phytoplankton, is primarily composed of polysaccharides, simple sugars (Myklestad 1974) and a substantially smaller fraction of proteins and amino acids (Myklestad and Haug 1972). However, the type, amount, and composition of phytoplankton-released organic matter is species specific and varies with nutrient status (Myklestad 1995). Despite widespread variability, dissolved organic matter exuded or released by phytoplankton are negatively charged and tend to aggregate due to cation bridging among their own polysaccharide polymers (Alldredge et al. 1993). Such aggregated polysaccharides provide a glue-like substrate that allows them to act as a catalyst in the coagulation of marine snow.

The formation of marine snow, agglomerated marine particles that are often dominated by aggregates of algal cells, is a process that plays a significant role in determining the sinking rate and efficiency of the export flux of organic carbon. The formation of marine aggregates is a function of; 1) the concentration of cells, 2) the physical forces that bring cells or

particles into contact with each other, and 3) the probability of successful adhesion following collision (Hunt 1980c). The last of these three factors – probability of successful adhesion upon collision of two particles – is termed “sticking efficiency”. The concentration of organic carbon at the ocean’s surface is a critical determinant of the potential flux of particulate carbon to the deep sea (Fowler and Knauer 1986). The form of the particulate carbon affects the sinking rate (Jackson and Burd 1998) and the efficiency (Turner 2002) with which the particulate material is remineralized during its downward transport. Genesis of marine snow generally occurs within phytoplankton blooms and the aggregates formed therein have relatively rapid settling velocities (Alldredge and Gotschalk 1988). While coagulation models have approximated sedimentation within small phytoplankton blooms (Kjørboe et al. 1994), such models are less reliable when used to predict export flux following large-scale phytoplankton blooms (Hill 1992), (Jackson et al. 2005). As a result, understanding the processes that regulate particle aggregation in the sea is central to improving our knowledge of large-scale oceanic carbon export.



# 1 The Effect of Physiology on Export Flux

## 1.1 BACKGROUND

Particle aggregation is a function of the size, collision frequency, and the sticking (or coalescence/coagulation) efficiency of the particles (McCave 1984). While collision frequency is a function of the turbulent energy within the water column, and the number and size of the particles present, the sticking efficiency of algal particles is believed to be a direct result of cellular exudation (Passow and Alldredge 1995b), cell morphology (Kjørboe et al. 1990), and surface properties (Waite et al. 1995). For cell-to-cell interactions the sticking efficiency (paraphrastically referred to as *stickiness*) is defined by the rate of coalescence, divided by the rate of collision (Hill and Nowell 1990). Despite its central importance to particle aggregation, the variability in sticking efficiency is the least-well understood yet significant parameter of algal aggregation models (Hill 1992), (Jackson 2005).

It has become increasingly clear that sticking efficiency is a dynamic property driven by cellular processes in phytoplankton and bacteria (Alldredge et al. 1995). Past efforts have demonstrated that sticking efficiency may vary by more than an order of magnitude (table 1.1). Unfortunately, phytoplankton aggregation experiments are generally conducted at turbulence levels that are several orders of magnitude higher

than the turbulence levels encountered during most phytoplankton blooms (fig. 1.1 and table 1.1). The unrealistic energy levels in experimental systems are also partly responsible for the difficulty in reproducing aggregation phenomena of natural phytoplankton communities as calm oceanic conditions appear to be ideal for the formation of large aggregates following phytoplankton blooms (Alldredge and Gotschalk 1989). Consequently, measurements of sticking efficiency under low shear conditions would be extremely important and might be expected to yield high values of sticking efficiency (Engel 2000).

Coagulation theory was used to estimate the sticking efficiency of a 23-day mesocosm monoculture of the diatom *Thalassiosira pseudonana*. In this mesocosm the sticking efficiency increased as the bloom aged. This increase in sticking efficiency was correlated with changes in the physiological state of the diatoms within the mesocosm. Variability of phytoplankton sticking efficiency, as was observed in this study, can result in enhanced bloom-associated particle export flux in the oceans.

## 1.2 METHODS

### *1.2.1 mesocosm design*

The experiment was replicated in two separate mesocosm experiments. Each experiment was conducted in a 1500-liter annular flume at Rutgers University's Institute of Marine and Coastal Science. The glass annular flume has an outer diameter of 3.99 meters and a channel width of 30 cm (Hentschel 2004). During the experiments, the flume had a water depth of 42cm and was illuminated with 24 - hour continuous light. The mean irradiance in the flume during the experiments was  $172 \mu\text{mol photon (m}^2 \text{ sec)}^{-1}$  and was provided by Philips cool white plus fluorescent bulbs. The light field for advanced bloom stage conditions was lower due to the significant absorption of light by the dense phytoplankton populations.

### *1.2.2 mesocosm environment*

The top, which rotates counter to the rotation of the bottom, drives the fluid flow within the flume. The flume temperature of both experiments was maintained at  $17 \pm 0.3$  °C via a titanium heat exchanger located in the counter-rotating top of the flume. The flume rotation speeds and temperature were both controlled via a data acquisition and process control system developed by Camile Products, CamileTG (version 3.7). The flume flow was

characterized using laser Doppler anemometry using Dantec Dynamics' FLOWare and measurements made with a Dantec 2-axis Laser Doppler Velocimeter (LDV). The LDV characterized 169 points, across the annular flume channel, to measure the horizontal and vertical velocity fields. There were 2000 validated measurements made by the LDV at each of the 169 fluid velocity sampling points. While the LDV has a precision of  $10^{-5}$  m (sec)<sup>-1</sup> unpublished studies in the IMCS annular flumes show that the uncertainty of the velocity measurements are less than  $10^{-4}$  m (sec)<sup>-1</sup> when at least 2000 samples are collected from a single point. Along-channel flow velocity was measured both vertically and horizontally by the LDV. Across-channel horizontal flow velocity (fig. 1.2 A) was characterized by using the continuity equation. To solve the continuity equation for across-channel velocity, we assumed that seawater in the flume was incompressible and that along channel flow was not divergent. The LDV sample points were spaced at a maximum distance of 1 cm apart in the center of the flume channel, and at a minimum distance of 2 mm near the flume walls. Due to the acceptance angle of the LDV laser in to the flume channel, we were not able to measure fluid velocities at heights less than 1.5 cm above the bottom of the flume. We calculated the shear rate ( $\gamma$ ) as the vertical gradient of the horizontal velocity, along the flume channel. Where buoyancy effects due to

temperature gradients are very small (as was the case in our annular flume), the mechanical turbulence kinetic energy (TKE) dissipation rate is calculated as  $\varepsilon = -\overline{u'w'} \frac{du}{dz}$  (see table 1.2 for definition of symbols). The spatially weighted mean shear rate of the flume (fig. 1.2 A) was used as an input variable for the model of sticking efficiency while the TKE dissipation rate of the flume (fig. 1.2 B) was used to provide a relative comparison to oceanic conditions.

The spatially weighted mean shear rate and TKE dissipation rate of the flume were,  $\gamma = 0.05 \text{ s}^{-1}$  and  $\varepsilon = 8.87 \times 10^{-7} \text{ m}^2 \text{ s}^{-3}$ . Additionally, the principal location of shear generation in the flume is from the counter-rotating top. Shear rates at the bottom of the flume, where algal cells and aggregates ultimately settled, were low. As a result, there was a thin, weak secondary flow along the boundaries of the flume channel. Over the duration of the experiments, the uni-modal shape and steadily declining y-intercept of the particle size distribution indicated that neither disaggregation nor Brownian pumping (McCave 1984) – the coagulation of previously undetectable particles into measurable size classes – were significant processes in the mesocosm. Once the algal aggregates settled on the bottom of the flume channel, they formed a cohesive mat. Throughout the experiment, there was no visible re-suspension of algal material from the

algal mat. The algal mat grew to an approximate thickness of 2 mm on the bottom of the flume channel over the course of the 23 - day experiment.

### *1.2.3 particle size distribution*

The initiation (logarithmic growth), maintenance (decreased growth), and senescence (decreased population level) phases of a population of *T. pseudonana* were followed over time within the flume. The bloom was initiated with a 20-liter inoculum of exponentially growing *T. pseudonana* cells into the f/10 medium in the mesocosm. During both experiments triplicate 50 ml samples were taken by hand once daily at 3 depths. The flume was sampled using a thin piece of PVC with 3 mounted 50 ml polypropylene centrifuge tubes. The centrifuge tubes were modified such that both ends of the tube required a cap. The tubes were mounted on the PVC to collect samples at 2 cm, 20 cm, and 40 cm above the flume bottom. Due to the fragile nature of algal aggregates, caution was exercised during extraction of the samples from the flume. Upon removal from the flume, the particle size and volume distributions were characterized via aperture impedance. We used a Beckman Coulter Counter Multisizer II with a 100 $\mu$ m orifice tube to analyze all samples within 2 - 10 minutes after being removed from the flume. If necessary, samples were carefully diluted using 0.2  $\mu$ m

filtered seawater. During cell concentration and volume fraction enumeration, particle coincidence (the coincident passage of more than 1 particle through the Coulter counter orifice) through the Coulter counter aperture did not exceed 7 % of the volume sampled. One drawback to the use of aperture impedance to determine aggregate size is the risk of particle break-up due to the high shear of the fluid as it passes through the orifice of the Multisizer (Gibbs 1982). We chose a 100  $\mu\text{m}$  Multisizer orifice for enumeration of particle characteristics because microscopic analysis from a preliminary flume-aggregation trial showed that aggregates of *T. pseudonana* cells (having an approximate equivalent spherical diameter of 3.5  $\mu\text{m}$ ) need to be comprised of about 25 *T. pseudonana* cells (equivalent spherical diameter of about 22  $\mu\text{m}$ ) to be adversely affected by high shear in the instrument orifice. Aggregates comprised of more than 25 cells were not observed during microscopy of a preliminary flume study. An aggregate comprised of 25 cells each having an equivalent spherical diameter (ESD) of 3.5  $\mu\text{m}$  would have a minimum ESD of 22  $\mu\text{m}$ . However, because of their fractal nature, the ESD of algal cell aggregates is expected to be somewhat larger than the predicted minimum value (Li and Logan 1995). The maximum floc sizes enumerated by the Multisizer during the experiment had ESDs between 30  $\mu\text{m}$  and 40  $\mu\text{m}$ . Although these values correspond with the

preliminary microscopy, the 100  $\mu\text{m}$  orifice used for PSD determination undoubtedly destroyed aggregates having an equivalent spherical diameter larger than 30  $\mu\text{m}$  or 40  $\mu\text{m}$ . As a result, our data may slightly underestimate the flocculation of algal cells in the flume.

The number of individual cells within aggregates was determined by employing a method similar to (Alldredge and Gotschalk 1989). Where aggregates were defined as particles having an ESD greater than  $2 \times 3.5\mu\text{m}$ , the samples were agitated to break apart any aggregates and the particle size distribution was subsequently measured using the Coulter Multisizer. The disaggregated cell counts were used to estimate 1) the specific growth rate of the culture and 2) the number of cells bound within aggregates within the culture. The numbers of individual cells, having an ESD approximately equal to 3.5  $\mu\text{m}$ , from both the agitated and raw samples were compared. An increase in the number of individual cells following agitation is proportional to the number of aggregate bound cells in the raw sample.

#### *1.2.4 phytoplankton physiology*

Photosynthetic efficiency of electron transport in photosystem II was determined by using a Fluorescence Induction and Relaxation (FIRE) fluorometer (Gorbunov and Falkowski 2004) as an indication of the



physiological health of a phytoplankton population (Kolber and Falkowski 1993). Cells were also harvested from the second experiment, for caspase activity and superoxide dismutase expression analyses, by means of centrifugation (10,000 x g, 4°C, 10 min) and immediately frozen in liquid nitrogen and storage in -80°C until processing.

#### *1.2.5 caspase activity*

Cells were resuspended in caspase activity buffer (50 mM N-Cyclohexyl-2-aminoethanesulfonic acid (pH 7.3), 100 mM NaCl, 10% sucrose, 0.1% 3-[(3-Cholamidopropyl)dimethylammonio]propanesulfonic acid, 10 mM dithiothreitol) and sonicated, and cellular debris was pelleted by means of centrifugation (16,000 x g; room temperature; 2 min) as described in Bidle et al. (Bidle et al. 2007). Cell extracts were incubated with 50 µM IETD-7-Amino-4-trifluoromethylcoumarin (Calbiochem, San Diego, CA) for 4 h at 25°C. Fluorescence was measured by using a Spectra Max Gemini XS plate reader (excitation wavelength = 400 nm, emission wavelength = 505 nm).

### 1.2.6 SOD expression

Sample protein concentration was quantified using the bicinchoninic acid method (kit made by Pierce Biotechnology) and 5 µg for each was loaded on a 15% SDS/PAGE gel and transfer on a PVDF membrane. The blots were then probed with anti-TpMnSOD (1:1000), raised against the recombinant MnSOD from *T. pseudonana* (Wolfe-Simon et al. 2006). An HRP conjugated to a polyclonal goat anti-rabbit IgG (Pierce; 1:30,000) was used, followed by chemoluminescence detection (SuperSignal; Pierce).

### 1.2.7 TEP abundance

Relative changes in Transparent Exopolymer Particles (TEP) were enumerated in triplicate following the spectrophotometric Alcian Blue staining technique of (Passow and Alldredge 1995a). However, rather than calibrate the concentration of TEP to a Xanthan gum standard curve, relative changes in the TEP abundance were monitored by normalizing all values of TEP to the lowest (and first) measured value (day 9). These qualitative estimates were used to assess changes in the levels of TEP.

### *1.2.8 bacterial abundance*

From each sample of the second mesocosm experiment, 15 ml were fixed with a final concentration of 0.2 % Formalin. Bacterial abundance was determined using a DNA-specific stain, 4,6-diamindino-2-phenylindole (DAPI). With minor modifications (we used black filters instead of staining) we followed the DAPI staining technique as described in (Porter and Feig 1980). The DAPI stained and mounted samples were stored at -4 °C for less than 2 weeks prior to enumeration. Imaging of the fixed sample slides was conducted using an Olympus BX60 light microscope at 100X magnification. An Olympus America camera controlled through Olympus MicroSuite software was mounted to the microscope to allow for the capture of five randomly located digital images from each stained slide. A 5 × 5 grid was randomly counted from each image. In both the random field selection and grid counting, a random number generator was used to provide the coordinates of the field to be imaged or the grid to be counted. We used the National Institute of Health's freely available image analysis software, *ImageJ*, for bacterial cell enumeration. The counts from each of the 5 grids were used to extrapolate the bacterial abundance for each triplicate sample.

### 1.2.9 sticking efficiency

Particle sticking efficiency,  $\alpha$ , is the ratio of successfully adhesive particle collisions to the total number of particle collisions which result from physically mediated interactions. The sticking efficiency of a system is manifest through time-dependent variations in the measured particle concentrations. The observed rate of coagulation can be compared to theoretical models of physically based coagulation processes to estimate the mean sticking efficiency in the natural system. While this method of estimating sticking efficiency has been successfully tested for clay particles (Hunt 1982) and colloids (Brunk et al. 1998), it has yet to be tested for systems containing algal cells.

In a system containing only algal cells (wherein mass is conserved) the particle size distribution changes as a result of cell growth ( $\mu$ , units of time<sup>-1</sup>), gravitational settling, and coagulation ( $\beta$ , units of time<sup>-1</sup>) (Jackson 1990). This is illustrated by a simplified formulation of Jackson's (1990) algal cell aggregation model (eq. 1.1)

$$(1.1) \quad \frac{dC}{dt} = \mu C - \frac{W}{Z} + \alpha \beta C$$

Where  $C$  is the volume concentration of cells (cells (volume)<sup>-1</sup>),  $t$  is time,  $W$  is the mean particle settling velocity (length (time)<sup>-1</sup>),  $Z$  is the

distance a settling particle must fall to be removed from or enter into the open system, and  $\beta C$  is a synthesis term of the coagulation processes (cells (volume)<sup>-1</sup> (time)<sup>-1</sup>) described in detail in Jackson (1990).

If biomass gains (cell growth) into and losses (cell settling) from an algal cell size distribution are taken into account, changes in the particle size distribution will reflect the rate of coagulation of algal cells (eq. 1.2).

$$(1.2) \quad \frac{dC}{dt} - \mu C - \frac{W}{Z} = \alpha \beta C$$

While direct measurement of algal cell coagulation is difficult, sticking efficiency can still be estimated if a suitable model of coagulation processes (where  $\beta_m C = \beta C$ ) is applied and equation 1.2 is further re-arranged into equation 1.3.

$$(1.3) \quad \alpha = \frac{\frac{dC}{dt} - \mu C + \frac{W}{Z} C}{\beta_m C}$$

The three terms in the numerator of equation 3 can be measured or calculated from first principles. At the 20 cm depth in the flume, cell volume concentration ( $dC (dt)^{-1}$ ) and growth ( $\mu C$ ) were directly measured. Using a simple model of Stoke's settling velocity, and volume balance over time between each of the 3 collection depths (40 cm, 20 cm, 2 cm), we were able to calculate the net effects of gravitational settling ( $WC (Z)^{-1}$ ) at the middle

(20 cm) of our three collection depths within the flume. We assumed that the density of the *T. pseudonana* cells was constant and that they were  $0.0288 \text{ g (cm)}^{-3}$  more dense ( $\Delta\rho$ ) than seawater (Waite and Nodder 2001).

To maintain a volume balance, we had to assume particle concentration was both horizontally homogenous and had a linear vertical gradient between our 3 discrete collection depths. However, based on the phytoplankton diffusion calculations of (Prieto et al. 2002), when measured on time scales less than several days, the water column in our annular flume was nearly homogenous. As a result measurements of mass balance at shorter time intervals, especially during the initiation and maintenance phases, were unreliable because there was not significant time for algal cells to settle between the points of the sampling grid. Consequently the model was initiated with data taken from samples collected about 6-7 days apart.

The denominator of equation 1.3 was calculated by using the Coulter Counter to measure the particle distribution at 20 cm depth. This continuous particle size distribution was then sectionalized, or binned into 10 discrete size-volume classes (Gelbard et al. 1980). The upper limit of each bin was twice the lower limit. Next, the sectionalized volume concentration was used to initiate the coagulation model of (Jackson and Lochmann 1992) such that the modeled rate of coagulation is represented by equation 1.4.

$$(1.4) \quad \beta_m C = \frac{1}{2} \sum_{i=1}^{l-1} \sum_{j=1}^{l-1} \beta_{i,j,l} Q_i Q_j - Q_l \sum_{i=1}^{l-1} \beta_{i,l} Q_i - \frac{1}{2} \beta_{l,l} Q_l^2 - Q_l \sum_{i=l+1}^s \beta_{i,l} Q_i$$

Here, the right side of equation 1.4 retains the nomenclature of Jackson & Lochmann (Jackson and Lochmann 1992), where  $i, j$ , and  $l$  are indices of the sectionalized particle size distribution,  $Q_i$ ,  $Q_j$ , and  $Q_l$  are the total volume of sections  $i, j$ , and  $l$ ,  $s$  is the number of sections, and  $\beta_{i,j,l}$ ,  $\beta_{i,l}$ , and  $\beta_{l,l}$  are coagulation coefficients that describe the interactions between particles in the sectionalized size distribution. Each coagulation coefficient represents the sum of all particle interactions resulting from Brownian motion ( $\beta_B$ ), differential settling ( $\beta_D$ ) and shear ( $\beta_S$ ) (McCave 1984). Brownian motion collisions are a result of the sub-microscale random motions of particles, also known as perikinetic interactions, while differential settling and fluid shear are orthokinetic interactions whereby particles collide as a result of hydrodynamics and differences between their relative velocities. We assumed that coagulation due to Brownian motion was not a significant mechanism of particle interaction ( $\beta_B = 0$ ), which was reasonable as evidence of Brownian pumping was not evident in the PSD measured in the flume. As a result, we only considered coagulation due to orthokinetic interactions ( $\beta_D$  and  $\beta_S$ ) in our estimate of algal cell sticking efficiency.

Substituting equation 1.4 into equation 1.3, and formally expressing the numerator to reflect the sectionalized approach (where  $m$  is biomass volume), equation 1.5 shows the form of equation 1.3 implemented to estimate the sticking efficiency of the *T. pseudonana* flume experiments.

(1.5)

$$\alpha = \frac{\frac{dQ_l}{dt} - \mu_l Q_l + Q_l Z^{-1} \int_{ml-1}^{ml} w(m) dm}{\frac{1}{2} \sum_{i=1}^{l-1} \sum_{j=1}^{l-1} \beta_{i,j,l} Q_i Q_j - Q_l \sum_{i=1}^{l-1} \beta_{i,l} Q_i - \frac{1}{2} \beta_{l,l} Q_l^2 - Q_l \sum_{i=l+1}^s \beta_{i,l} Q_i}$$

To model algal cell coagulation in the flume, we used the sectionalized particle size distribution and fluid shear ( $\gamma = 0.09 \text{ s}^{-1}$ ) measured in the flume. Because there is less than a 20 % difference between the length of the major and minor axes, *T. pseudonana* cells are approximately spherical and can be used as a model organism for particle interaction studies. A fractal coagulation kernel having a fractal dimension of 2.33 (Burd and Jackson 1997) was used for all higher order (where  $l > 1$ ) particle interactions. Otherwise, individual *T. pseudonana* cells ( $l = 1$ ) were defined as having a curvilinear collision function. Cell division in size classes larger than that of individual phytoplankton was likely insignificant (for  $l > 1$ ,  $\mu = 0$ ) due to the short duration of this experiment and the relatively short distance an aggregate needed to settle out of the mass balance measurement



grid. Furthermore, significant coagulation of algal cells occurred during the maintenance and senescent phases, periods when cell division rates were low. As a result, all size classes except for the smallest class (containing individual cells) excluded phytoplankton division. Algal cell division, as determined experimentally, was assumed to only occur in size class 1, which contained individual *T. pseudonana* cells. Gravitational settling, the third term within the numerator (eq. 1.5), was assumed to occur only in the size classes larger than the size class used for the growth term. In this study, the distribution of volume concentration was simplified into 10 size classes. While size class 1 contained individual cells, size classes 2-10 contained all other measured algal particles.

### 1.3 RESULTS

Although two separate mesocosm experiments were used to replicate our sticking efficiency analysis, extensive physiological parameters were only collected during the second experiment and are reported in this study. As described in the *Methods*, there are two mechanisms of algal particle interaction in the annular flume; differential sedimentation and fluid shear. A cross-section of the fluid shear rate within the annular flume is shown in figure 1.2 A. The spatially averaged shear rate of the flume cross-section is

$0.05 \text{ s}^{-1}$ . However, there are two primary regions of increased rates of fluid shear; the bottom and the top of the flume channel. Along both the top and the bottom of the flume, the highest rates of shear are found at the intersection with the sidewalls. The maximum shear rate,  $1.6 \text{ s}^{-1}$ , was measured at the top of the LDV sample grid - near the counter-rotating top of the flume. This is the region of maximum shear generation within the flume. The highest shear rate measured at the bottom of the LDV sampling grid, near the bottom of the flume, was  $0.29 \text{ s}^{-1}$ . Along the bottom of the flume, the region of increased shear ( $> 0.1 \text{ s}^{-1}$ ) did not extend more than 1.5 cm to 2 cm above the flume bottom. Our lowest sampling location (fig. 1.2 A, at 1.5 cm above the flume bottom) within the flume occurred within the upper reaches of this region of increased shear. In the middle of the flume channel, the minimum shear rate measured was  $0.002 \text{ s}^{-1}$ . Assuming that the fluid shear rates of the unmeasured areas (white portions near the edges of the cross-section in figure 1.2) of the flume were greater than  $0.1 \text{ s}^{-1}$ , 89.3 percent of the flume cross-section area had a fluid shear rate less than  $0.1 \text{ s}^{-1}$ . Shear rate within the annular flume is much lower than the rates of fluid shear used in previously published studies (fig. 1.1 and table 1.1) of phytoplankton sticking efficiency. The overall low rate of fluid shear within

the annular flume allowed coagulation processes to occur both at low energy levels and with minimal physical disruption to the aggregates.

As the number of sinking aggregates increased, there was an uneven distribution of settled material at the bottom of the flume. The direction of the flow field vectors, near the bottom of the flume (fig. 1.2 A), corresponds with the observed increase in accumulation of material towards the outer wall of the flume bottom (fig. 1.3 F). The mean magnitude of the cross-channel flow field vectors is  $7.6 \times 10^{-4} \text{ m s}^{-1}$  and is three orders of magnitude smaller than the mean along channel horizontal velocity,  $0.13 \text{ m s}^{-1}$ .

Consequently, the mean along channel velocity of the flume was used as the characteristic velocity value ( $u = 0.13 \text{ m s}^{-1}$ ) to estimate the Reynolds number of the fluid environment surrounding an individual phytoplankton cell in the experiment ( $Re = (uL)\nu^{-1}$ ). While the kinematic viscosity ( $\nu$ ) was approximated as  $1 \times 10^{-6} \text{ m}^2 \text{ s}^{-1}$ , the characteristic length scale of *T.*

*pseudonana* is the mean ESD ( $L \sim 4 \times 10^{-6} \text{ m}$ ). The resultant Reynolds number, 0.50, indicates that the low energy environment of the flume is dominated by viscous forces and the flow is nearly laminar. This estimate of the Reynolds number is quite conservative because the velocity of an individual phytoplankton cell relative to the surrounding seawater - resulting

in an even smaller Reynolds number - is likely much smaller than the abovementioned horizontal velocity.

The spatially weighted mean TKE dissipation rate of the flume was  $8.8 \times 10^{-7} \text{ m}^2 \text{ s}^{-3}$ . A TKE dissipation rate of this magnitude is comparable to the top 20 meters of the ocean's surface on a calm day (Petersen et al. 1998). Figure 1.2 B, a cross-section of TKE dissipation rate within the flume, shows the maximum ( $\epsilon = 1.36 \times 10^{-5} \text{ m}^2 \text{ s}^{-3}$ ) at the top of the water column (near the counter-rotating top) near the outer wall of the flume. Otherwise, 78 percent of the flume had TKE dissipation rate values with an order of magnitude equal to or less than  $10^{-7} \text{ m}^2 \text{ s}^{-3}$ .

As the number of cells and aggregates within the flume changed over the duration of the 23 - day experiment, the various stages of bloom development and collapse were evident (fig. 1.3 A-F). The concentration of *T. pseudonana* cells increased between days 0–6 (fig. 1.4 A) through exponential growth and into the early part of the stationary phase. After remaining in stationary phase for about 1 week, the phytoplankton bloom transitioned from late stationary (day 15) to senescent phase (day 23). During the decline of the bloom from days 15 to 23, there was a noticeable accumulation of algal cell material on the bottom of the flume channel (fig. 1.3 E & F). The accumulated material on the bottom of the flume was

distinctly separate from the water column. A nepheloid-like layer was not observed between the accumulated material at the bottom of the flume and the remainder of the water column. Coupling this observation with the shear cross-sections of figure 1.2 indicates that re-suspension of algal cells from the bottom of the flume was undetectable and was unlikely to have occurred. Furthermore if re-suspension of previously sedimented algal material had occurred to a significant degree, its effects would have been measured in the samples collected from 2 cm above the bottom of the flume. The replicate samples of cell concentrations for each of the three collection depths (40 cm, 20 cm, 2 cm) were consistent. Comparing each of the sample depths, the standard deviations did not vary from one another by more than 5 %.

During the initiation phase (days 1-6), photosynthetic efficiency of photosystem II, as measured by variable fluorescence ( $F_v/F_m$ ), increased from below the level of detection to between 0.5 and 0.6 (fig. 1.6). Following a decline in the photosynthetic efficiency, the phytoplankton cell concentration stopped increasing and stabilized near day 5. During the stationary, or maintenance, phase of the bloom, phytoplankton cells growth has slowed yet the cells did not rapidly settle out from the water column. The maintenance phase of the bloom was characterized by the slight decrease of both photosynthetic efficiency and cell concentration over time.

The transition from maintenance to senescent phase occurred between days 10 and 20 -when there was a concomitant decline in the slopes of cell concentration (fig. 1.5) and photosynthetic efficiency (fig. 1.6). The senescent phase of the bloom did not dominate the mesocosm until after day 20 when the photosynthetic efficiency rapidly fell from about 0.14 to near zero. Because our calculations require discrete time steps, we defined the end of the maintenance phase as occurring at the mid point of the steady decline in cell concentration, approximately days 15-16. The senescent phase of the bloom lasted from day 16 until the photosynthetic efficiency approached zero on day 23. The decline of the bloom during the senescent phase was distinctly visible in the flume from days 17 to 23 (fig. 1.3).

Another indicator of cell physiology, oxidative stress (as indicated by SOD expression), increased prior to the crash of the bloom (fig. 1.6). Oxidative stress was most visible in the algal cells accumulated on the bottom of the flume but was not observed in cells that remained suspended in the water column as the bloom transition from early to mid senescence around day 20. Concurrent with the changes in cellular oxidative stress, there was also an increase in the activity of enzymes responsible for the initiation of apoptotic pathways. Caspase-8 activity, normalized to protein concentration, increased through the senescent phase (fig. 1.6). The peak in

Caspase-8 activity coincided with the largest increase in TEP between two sample points. Overall, there was also a slight increase in the relative concentration of TEP as the bloom aged (fig. 1.6).

Both cell concentration and cell volume fraction (the fraction of a volume of water that was occupied by algal particles) measurements were used as an indicator of physical changes within the phytoplankton bloom. Cell volume fraction will approximate cell concentration, but will deviate if aggregation occurs such as was observed during the senescent phase (fig. 1.4). The deviation between volume fraction and cell concentration results from the fractal nature of phytoplankton aggregation (Li and Logan 1995). An increase in the mean particle volume may particularly be attributed to aggregation when large increases in mean particle volume occur while photosynthetic efficiency of the phytoplankton is decreasing during the senescent phase of the bloom. For example, during the initiation phase of the experiment, mean particle volume remained stable at about  $31 \mu\text{m}^3$  (data not shown) while photosynthetic efficiency was highest during bloom initiation. A volume of  $31 \mu\text{m}^3$  approximates an individual *T. pseudonana* cell of  $3.9 \mu\text{m}$  ESD. This is slightly larger than the measured mode ESD of  $3.5 \mu\text{m}$  because rapidly dividing algal cells skew the volume concentration distribution due to their slight increase in volume prior to cellular division.

Throughout the maintenance phase both the cell concentration and the cell volume fraction (fig. 1.4) along with photosynthetic efficiency (fig. 1.6) steadily declined. Yet, during the maintenance phase there was not a visibly discernible change of the bloom within the annular flume (fig. 1.3 C-D). However, as the *T. pseudonana* cells entered the senescent phase near days 15-17, changes in both the particle size distribution (fig. 1.4) and in the optical clarity of the bloom (fig. 1.3 D-E) were apparent. Additionally, algal cell aggregation became apparent as the mean particle volume increased until days 21 -22 to an ESD of 9  $\mu\text{m}$ .

In addition to measuring the mean particle number and fraction volume, we also estimated the number of aggregated phytoplankton as a fraction of the total bloom population. The fraction of aggregated phytoplankton cells was highest during the transition from the end of the maintenance phase through the beginning of the senescent phase (fig. 1.5). There was a notable decrease in the fraction of aggregated cells on approximately the same day as the largest mean particle volume. This would suggest that while many aggregates settled out of the water column between days 20 and 22, the number of suspended (and subsequently measured) individual cells remained relatively stable. Supporting this interpretation is the apparent growth rate of *T. pseudonana*. The apparent growth rate is the



balance between an increase in biomass due to cell division and the loss of biomass due to the settling of individual cells. In the framework of our experiment and analysis, the loss of algal biomass due to settling is partitioned into two terms – individual algal cells (biomass losses from size class 1) and aggregates (biomass losses from size classes 2-10). Where the apparent growth rate is positive, such as in the initiation phase, individual cells are dividing more rapidly than they are settling out of the water column. Conversely, during the end of the maintenance and into the senescent phase of the bloom, the apparent growth rate decreases and ultimately becomes negative as individual algal cells settle downward either as individuals or as they are scavenged from the water column by larger particles.

Increased bacterial abundance and hydrolytic enzyme activity has also been observed with phytoplankton aggregation (Smith et al. 1992). Indeed, during our experiment, total bacterial counts were highest during the end of the maintenance and the beginning of the senescent phase, when phytoplankton aggregates were prevalent in the flume (fig. 1.5). The peak in bacterial population coincided with the time period having the largest fraction of aggregated *T. pseudonana* cells.

After determining the growth rate and settling velocities, as described in *methods*, the sticking efficiency for each phase of the *T. pseudonana* bloom was estimated (fig. 1.5 & fig. 1.6) by applying equation 5 to the initiation and senescent phases of both of the mesocosm experiments and to the maintenance phase of only the second experiment (due to sampling error, data were collected at only one depth during the maintenance phase of the first experiment). As a result, the initiation, maintenance, and senescent phases of the *T. pseudonana* bloom had respective sticking efficiencies of  $0.08 \pm 0.03$ , 0.26, and  $0.73 \pm 0.16$ .

#### 1.4 DISCUSSION

Measurements of particle aggregation dynamics at low shear are critically important because they reflect the conditions under which fragile marine snow is formed in nature. Phytoplankton blooms occur as nutrient-replete water columns stratify and the mixed layer depth shallows allowing algal cells to remain in the euphotic zone. As the phytoplankton bloom matures nutrients in the upper mixed layer are depleted and the phytoplankton population begins to senesce. During these latter stages of the bloom marine snow becomes evident. Accordingly, aggregates are formed when cell concentrations are high and rates of shear are low. Our laboratory

manipulations mimic this sequence of events and provide a physiological basis for such bloom dynamics.

#### *1.4.1 algal cell physiology and sticking efficiency*

Significant changes in *T. pseudonana* physiology occurred in concert with an increase in the sticking efficiency of the cells. The goal of this study was to examine particle interactions and the concordant changes in cell physiology in a low shear environment more characteristic of natural bloom conditions. During our low-shear mesocosm bloom we observed an increase in the sticking efficiency of algal cells as the population aged and began to senesce. The increase in the sticking efficiency was mirrored by declines in the photosynthetic efficiency, which explained 66% of the variation in the fraction of aggregated cells. As evidenced by the slow decline of the photosynthetic efficiency of PSII without a concomitant decline in irradiance, during the maintenance phase the diatom bloom in this mesocosm began its demise from maintenance into senescence due to a slow draw down of inorganic nutrients.

Plants and algae generate reactive oxygen species (ROS) as metabolic byproducts of the electron transport during respiration and photosynthesis. Under adverse environmental conditions an increase in ROS production

leads to the induction of various antioxidant enzymes such as superoxide dismutase (SOD), catalase, and ascorbate peroxidase to detoxify harmful damage to lipids, thiol proteins and nucleic acids (Butow et al. 1997).

Induction of a biochemical cascade leading to cell death occurs once ROS production exceeds the antioxidant cellular capacity. Previous studies have shown a similar mechanism in the demise of the dinoflagellate *Peridinium gatunense* bloom which was initiated by CO<sub>2</sub> limitation that led to the accumulation of ROS (Vardi et al. 1999). The rise in antioxidant enzymatic activities and in the fraction of ROS-positive cells towards the peak of the bloom corroborate this observation. Additionally, induction of oxidative stress played a central role in triggering a coordinated cell death of the entire *P. gatunense* population (Vardi et al. 2007).

Autocatalytic programmed cell death (PCD) has recently been demonstrated in major classes of phytoplankton in response to environmental stresses, such as nutrient and light deprivation, UV, allelochemicals and viral infection (Bidle and Falkowski 2004). This self-destructive cellular mechanism was proposed to play a critical role in the demise of a phytoplankton bloom independent of zooplankton grazing. A specific family of cysteine aspartate-specific proteases (caspases) constitutes a ubiquitous biochemical hallmark of triggering the execution phase of the

PCD pathway in metazoans (Segovia et al. 2003). Recently, caspase activities have also been implicated as part of phytoplankton cell death machinery activated in response to nutrient depletion and virus infection (Berman-Frank et al. 2004).

Diatoms appear to rely primarily on a chloroplast localized MnSOD to scavenge superoxide to molecular oxygen and hydrogen peroxide (Wolfe-Simon et al. 2006). Using an antibody raised against *T. pseudonana* MnSOD (Wolfe-Simon et al. 2006) we observed the induction of MnSOD prior to bloom termination, indicating that cells experienced an oxidative stress. During this phase cells exhibited impaired photosynthetic efficiency and elevated caspase activity. The high caspase activity was coupled with an increase in TEP production and a progressively increasing sticking efficiency.

Such an increase in sticking efficiency may result from a combination of two distinct yet related processes. One reason for the increasing sticking efficiency during this transition may be the stabilization of the cell's surface area, due to decreased cellular division, relative to the cell's photosynthetic efficiency. As described by (Busch and Stumm 1968); during exponential growth, cell surfaces may be synthesized faster than they can be covered by exuded polymers. When cell growth and division slows down while

photosynthetic machinery are still efficient, the amount of the cell's surface that is covered by exuded photosynthate will increase. In our mesocosm, the rate of algal cell division stabilized as the bloom proceeded from bloom initiation into maintenance while photosynthetic efficiency continued to steadily decline through bloom maintenance and into bloom senescence. Because the cells continued to photosynthesize without rapidly dividing or growing, excess photosynthate had the opportunity to accumulate without an increase in cell surface area. Another reason for increased sticking efficiency as the bloom progressed is the increase in cellular oxidative stress and the subsequent cellular response and TEP production that was observed during the maintenance and senescent phases. Similar to the *T. pseudonana* cells of this study, Fe-stressed *Trichodesmium* cultures and natural populations were recently shown to have induced caspase activity prior to increased production of TEP (Berman-Frank et al. 2007). This link between cells undergoing PCD and an increase in the pool of TEP was observed predominantly in sinking *Trichodesmium* cells, suggesting a higher proportion of vertical export of organic matter in PCD-high TEP-releasing cells. Although previous work has shown that TEP are abiotically formed from phytoplankton-released polysaccharides (Passow et al. 1994), until now there has been little quantitative evidence of a coupling of the cellular

physiological status and TEP. Such a coupling of cellular physiology and TEP production, as shown in this study, may have important implications for the fate of organic matter produced during a phytoplankton bloom.

Accordingly, such an explanation requires TEP to act as the adhesive holding algal cells together upon collision. Indeed, both algal exudates (Myklestad 1974) and bacterial activity (Smith et al. 1995) tend to increase during the maintenance phase of a phytoplankton bloom. Although not mutually exclusive, the increase in the sticking efficiency may be a result of either algal cell exudates or an increase in “background particles” such as transparent exopolymer particles (TEP) or bacteria. Background particles such as TEP (Engel 2000), or bacteria (Smith et al. 1995) have been demonstrated to play a crucial role in the sticking efficiency of algal cells (Hill 1992). If TEP serve as an adhesive during phytoplankton coagulation, then an increase in the number of aggregates will lag an increase in the concentration of TEP itself. When the aggregated fraction of cells could be reliably estimated (concentration  $> 10^5$  cells per ml), significant variability between the number of aggregated cells and TEP was explained when aggregation lagged TEP by 1 day ( $n = 8$ ,  $p < 0.001$ ,  $r^2 = 0.70$ ). On the other hand, TEP concentration was not able to explain variation in the abundance of bacteria with ( $n = 12$ ,  $p = 0.003$ ,  $r^2 = 0$ ) or without ( $n = 12$ ,  $p = 0.002$ ,  $r^2 =$

0.013) a lag of 1 day. However, bacterial abundance variability is explained by concomitant changes in the fraction of algal cells bound in aggregates ( $n = 8$ ,  $p = 0.001$ ,  $r^2 = 0.720$ ). The strong correlation between TEP prior to aggregation supports the hypothesis of TEP acting as “background particles” to increase the rate of algal cell aggregation. Meanwhile, bacteria appear to have colonized the aggregates in this mesocosm and may play a role in the strength of adhesion once an aggregate has been formed. Additionally, because turbulence is inversely proportional to bacterial production in the ocean (Moeseneder and Herndl 1995), the role of bacteria on subsequent algal aggregate sticking efficiency may be enhanced under low shear conditions.

Despite the possible role of non-algal particles, our estimates of increasing sticking efficiency with the age of the bloom, which range from near 0 to about 0.73, are comparable to previous studies (table 1.1). Yet, given the general agreement between this study and previously published values of sticking efficiency, the maximum sizes of aggregates in the flume were much smaller than are observed under similar oceanic conditions. Under calm oceanic conditions, aggregation due to differential sedimentation is dominant compared to shear coagulation (Hunt 1980a). For example, the level of energy in our experiment was comparable to the levels



observed in the ocean by Riebesell (Riebesell 1991), (Riebesell 1992) and Kiørboe et al. (Kiørboe et al. 1998). However, the maximum size of algal cell aggregates in our flume were between 30 $\mu\text{m}$  and 40 $\mu\text{m}$  (ESD) while the above cited field studies observed centimeter sized aggregates. The primary reason for this discrepancy in maximum observed particle size; while oceanic particles have many meters over which differential sedimentation collisions may occur, the flume provided only 42cm for differential sedimentation. The short settling path length of the flume prevented the formation, due to differential sedimentation, of larger aggregates.

As the mesocosm bloom progressed, differential sedimentation played an increasingly important part in the coagulation of algal cells. Following Hunt's (Hunt 1980b) simplifications, and assuming that *T. pseudonana* cells (mean ESD = 3.5  $\mu\text{m}$ ) in our flume interacted with the mean algal particle size during each of the three phases of the bloom (mean ESD during; initiation = 3.5  $\mu\text{m}$ , maintenance = 4.3  $\mu\text{m}$ , senescence = 6.5  $\mu\text{m}$ ) the magnitude of the collision kernels was calculated (where  $\gamma = 0.05 \text{ s}^{-1}$  and  $\Delta\rho = 0.028 \text{ g cm}^{-3}$ ). Because the interacting particles during the initiation phase are very similar in size, coagulation due to differential sedimentation approached zero ( $\beta_D = 0 \text{ cm}^3 \text{ s}^{-1}$ ) – allowing shear interactions ( $\beta_S = 2.9 \times 10^{-18} \text{ cm}^3 \text{ s}^{-1}$ ) to dominate. While each of the two collision functions during

the maintenance phase were nearly equal in influence ( $\beta_D = 4.5 \times 10^{-18} \text{ cm}^3 \text{ s}^{-1}$ ,  $\beta_S = 3.9 \times 10^{-18} \text{ cm}^3 \text{ s}^{-1}$ ), differential sedimentation was the dominant mechanism of coagulation during the senescent phase ( $\beta_S = 3.6 \times 10^{-17} \text{ cm}^3 \text{ s}^{-1}$ ,  $\beta_S = 8.3 \times 10^{-19} \text{ cm}^3 \text{ s}^{-1}$ ). Similar to prediction and observations of the ocean, phytoplankton aggregation due to differential sedimentation dominated the late stages of this mesocosm bloom. And, while differential sedimentation plays an increasingly important role in aggregate formation during a phytoplankton bloom, changes in sticking efficiency will affect the overall rate of coagulation.

#### *1.4.2 sticking efficiency and export flux*

In an overview of coagulation in marine systems, Jackson and Lochmann (Jackson and Lochmann 1993) analyzed an algal cell coagulation model with a two-stage variable sticking efficiency at low shear. They found that a two-phase sticking efficiency model had the same timing and a slightly larger biomass export compared to a model with a constant sticking efficiency. However, when we applied a variable sticking efficiency ( $\alpha_{\text{initiation}} = 0$ ,  $\alpha_{\text{maintenance}} = 0.25$ ,  $\alpha_{\text{senescence}} = 1$ ) to each of the three phases (three stage sticking efficiency) of a modified version of Jackson's (Jackson 1990) coagulation model, both the timing and magnitude of the export event

were different compared to the export modeled with a constant sticking efficiency (fig. 1.7). A series of model blooms with both static ( $\alpha = 1$ ) and the above-described dynamic sticking efficiency were numerically simulated for the approximate length of the phytoplankton bloom observed in the mesocosm experiments. The duration of the initiation, maintenance, and senescent phases of the model runs were based on the observed lengths of each phase in the mesocosm experiments. One difference between the model and the experimental observations is the overall length of the bloom. In the numerical models, the export flux during the senescent phase stabilized by day 21 for each simulated bloom. As a result, the numerical simulations were run for 21 days (1 model day = 1 model time step) instead of the 23 observed in the mesocosms. The variable sticking efficiency increased the export flux by nearly a factor of two for all of the simulated oceanic conditions except for a less pronounced increase in export among large diatoms in a coastal simulation (fig. 1.8).

When a phytoplankton bloom is initiated, a low sticking efficiency will allow biomass to increase such that cells reach a relatively high *critical concentration* ( $C_{cr}$ ); the cell concentration at which biomass loss due to coagulation and settling is balanced by biomass gains due to cellular division (Jackson 1990). In a phytoplankton bloom having three phases, the rate of

coagulation rises as a result of the combination of a high concentration of cells and the gradually increasing sticking efficiency. The punctuated event illustrated in figure 1.7 indicates that aggregates rapidly formed as the cell number reached the critical cell concentration. Because sticking efficiency is difficult to parameterize, extremely small values ( $\alpha < 0.01$ ) are likely to be unreliable. And, because the maximum value is 1, the sticking efficiency is capable of altering the critical concentration of a phytoplankton bloom by up to 2 orders of magnitude. With this relative insensitivity in mind, using  $C_{cr} = \mu' (10.4 \alpha \gamma r^3)^{-1}$  (Jackson and Burd 1998), the  $C_{cr}$  during each of the bloom phases in this mesocosm was calculated (table 1.3) using the estimated dynamic sticking efficiency of the flume and the often assumed static value of sticking efficiency ( $\alpha = 1$ ). In both the dynamic and static calculations of  $C_{cr}$ , cellular physiology precluded a critical concentration of *T. pseudonana* cells during the initiation and maintenance phases of the bloom. In essence, the size of the bloom was limited by physiological constraints and not physical aggregation processes during the initiation and maintenance phases. However, after the physiological aging of *T. pseudonana*, physical coagulation processes dominated the senescent phase of the bloom as the critical concentration of algal particles was reached. During the senescent phase, as the concentration of algal particles fell below the critical

concentration because of the high sticking efficiency, coagulation dynamics played an increasingly important role in the export flux from the bloom.

Consequently, phytoplankton blooms modeled using a dynamic sticking efficiency have similar dynamics to natural blooms. Using a dynamic sticking efficiency, similar to the estimated values of this study, increases the critical concentration such that cellular physiology is the bloom-limiting factor during bloom initiation and maintenance phases. And, the increased sticking efficiency attained during the later stages of a bloom will shift the bloom dynamics from physiological to physical forcing. Simulating phytoplankton dynamics that shift a bloom from being physiologically limited to physically controlled results in simulated phytoplankton blooms that share the pulsed nature of particulate flux that is characteristic of sediment trap data from both the Pacific (Karl et al. 1996) and the Atlantic Oceans (Steinberg et al. 2001). When considering models of export flux, such as the one used in this study, it is crucial to note that changes in the duration of each bloom phase primarily affects the degree to which the particle flux of each phase approaches a steady state. For example, when primary productivity is low but sustained, such as in oligotrophic systems, the small but constant flux of particles from the surface ocean approximate a steady state where primary production is more or less

balanced by export flux from the surface. Comparatively, the nature of particle formation and mesopelagic processes are responsible for ecosystems having a pulsed export flux that can be 26% to 35% more efficient compared to an ecosystem having a constant “rain” of particles out of the euphotic zone (Buessler et al. 2007).

## 1.5 TABLES

Table 1.1, Rates of Fluid Shear and Estimated Sticking Efficiency in Phytoplankton Aggregation Studies.

Shear Rate (s <sup>-1</sup> )	Sticking Efficiency ( $\alpha$ )	Device
50	0.05 - 0.12	Oscilating Grid <sup>1</sup>
0.03 - 0.05	0.88	Settling Chamber <sup>2</sup>
10	0 - 0.98	Couette Chamber <sup>3</sup>
5.7	0.001 - 0.13	Couette Chamber <sup>4</sup>
30	0.01 - 0.6	Couette Chamber <sup>5</sup>
3 - 30	8 x 10 <sup>5</sup>	Couette Chamber <sup>6</sup>
1.3	10 <sup>-4</sup> - 0.37	Rotating Propeller <sup>7</sup>
5 - 10	0.03 - 0.8	Couette Chamber <sup>8</sup>
8 - 10	0 - 0.7	Couette Chamber <sup>9</sup>
5	~0 - 0.03	Couette Chamber <sup>10</sup>
10	0 - 0.40	Couette Chamber <sup>11</sup>
0.86	< 0.1 - 1	Couette Chamber <sup>12</sup>
0.86	0.04 0.18	Modeled <sup>13</sup>
0.05	0 - 0.73	Annular Flume <sup>14</sup>

1(Kiørboe et al. 1990), 2 (Alldredge and McGillivray 1991), 3 (Kiørboe and Hansen 1993), 4 (Drapeau et al. 1994), 5 (Kiørboe et al. 1994), 6 (Passow et al. 1994), 7 (Ackleh et al. 1995) The shear rate was estimated based on published data; where collision velocity was 0.11 cm s<sup>-1</sup> and the distance between the colliding particles was 2-3 cm., 8 (Dam and Drapeau 1995)

Samples used in the Couette chamber were taken from the same mesocosm as Ackleh et al. (1995)., 9 (Hansen and Kiørboe 1997), 10 (Waite et al. 1997), 11 (Kiørboe et al. 1998), 12 (Engel 2000), 13 (Engel et al. 2004) Sticking efficiency was estimated based on a linear regression of Couette chamber data from Engel 2000, 14 (Kahl et al. 2008)



Table 1.2, Table of Mathematical Symbols

Parameter	Description	Units
$C$	Concentration of cells	cells (cm) <sup>-3</sup>
$C_{cr}$	Critical concentration of cells	cells (cm) <sup>-3</sup>
$i, j, l$	Particle size distribution section indices	
$L$	Characteristic length scale	m
$Q$	Sectional particle volume	cm <sup>3</sup>
$R_e$	Reynolds number	
$s$	Number of sections	
$u$	Horizontal fluid velocity	m (sec) <sup>-1</sup>
$u'$	Variation in horizontal fluid velocity	m (sec) <sup>-1</sup>
$W$	Particle settling velocity	m (sec) <sup>-1</sup>
$w'$	Variation in vertical fluid velocity	m (sec) <sup>-1</sup>
$Z, z$	Height above bottom of flume channel	m
$\alpha$	Sticking efficiency	
$\beta$	Coagulation coefficient	cm <sup>3</sup> (cell) <sup>-1</sup> (sec) <sup>-1</sup>
$\Delta\rho$	Excess density of cells compared to seawater	g cm <sup>-3</sup>
$\varepsilon$	Mechanical Turbulent Kinetic Energy	m <sup>2</sup> (sec) <sup>-3</sup>
$\gamma$	Fluid Shear Rate	(sec) <sup>-1</sup>
$\mu$	Cell growth rate	(day) <sup>-1</sup>
$\nu$	Kinematic Viscosity	m <sup>2</sup> (sec) <sup>-1</sup>

Table 1.3, Predicted and measured  $C_{cr}$  during the second mesocosm flume experiment using generally assumed values ( $\alpha = 1$ ) of sticking efficiency and a comparison with values estimated from the experiment.

Bloom Phase	Estimated $C_{cr}$	Measured $C_{max}$	$\mu'$	$\alpha$
Initiation	$3.7 \times 10^6$	$1 \times 10^6$	1.8	1
Maintenance	$9.7 \times 10^5$	$1 \times 10^6$	0.47	1
Senescence	$2.0 \times 10^4$	$1 \times 10^5$	0.01	1
Initiation	$4.7 \times 10^7$	$1 \times 10^6$	1.8	0.08
Maintenance	$3.8 \times 10^6$	$1 \times 10^6$	0.47	0.26
Senescence	$2.8 \times 10^4$	$1 \times 10^5$	0.01	0.73

## 1.6 FIGURES

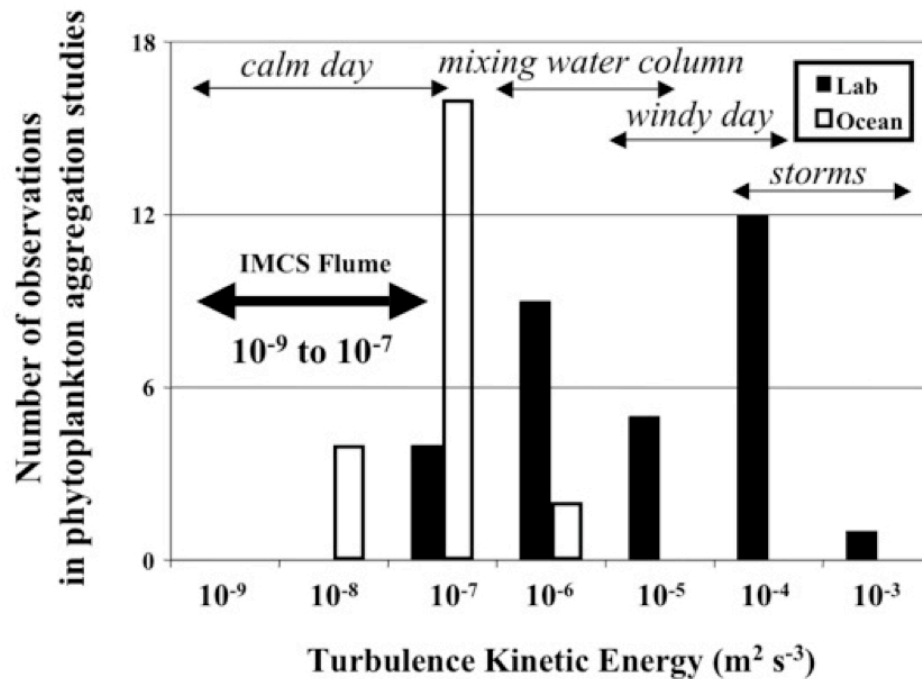


Figure 1.1, A comparison of estimated energy levels during phytoplankton aggregation experiments in the lab and in the sea. Energy levels used in controlled environments (lab studies) during aggregation studies were compiled from published data (Kiørboe et al. 1990, Riebesell 1991, Kiørboe & Hansen 1993, Drapeau et al. 1994, Kiørboe et al. 1994, Kiørboe et al. 1998, Passow et al. 1994, Alldredge et al. 1995, Dam & Drapeau 1995, Hansen & Kiørboe 1997, (Karp-Boss and Jumars 1998), Engel 2000, Engel et al. 2004. Ocean energy levels from field data (Alldredge et al. 1990,

Passow & Alldredge 1994, Alldredge et al. 1995, Passow 2000, Passow 2002, Jackson 1995, (Logan and Kilps 1995), Kiørboe et al. 1998) during aggregation studies were estimated using equation 4 from Riebesell 1992.

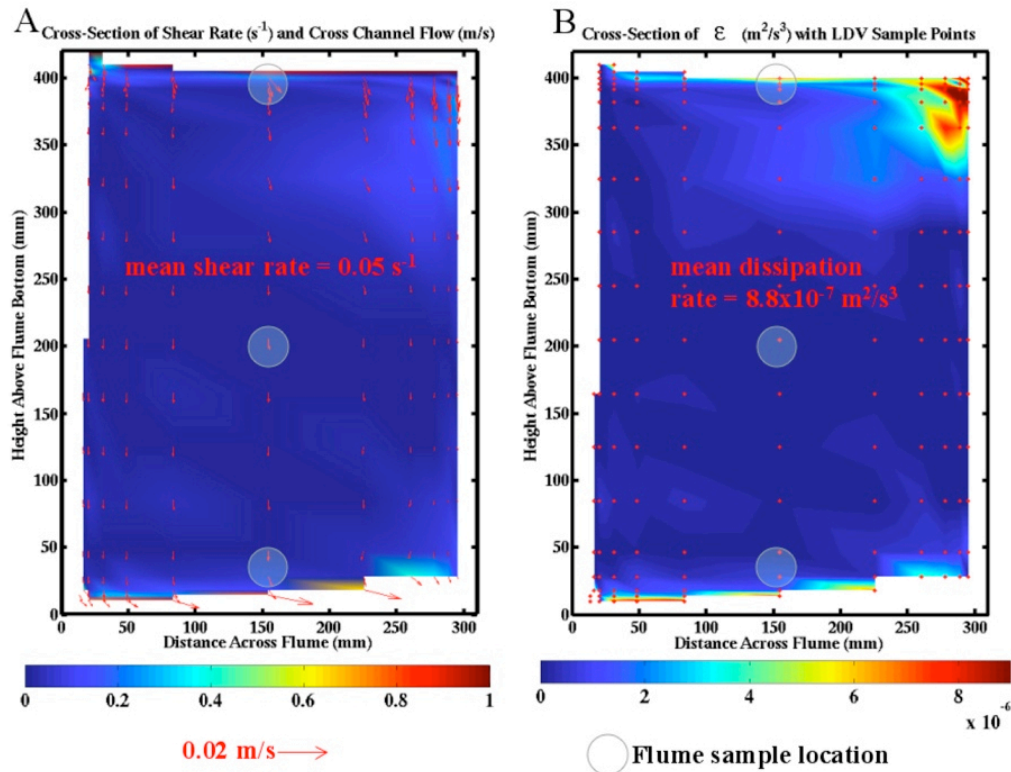


Figure 1.2, Channel cross-section of flow characteristics of the annular flume at the Institute of Marine and Coastal Sciences, Rutgers University.

(A) Shear-rate, cross channel flow vectors, and sample collection locations.

(B) Turbulence Kinetic Energy Dissipation Rate, Laser Doppler Velocimeter measurement points, and sample collection locations.

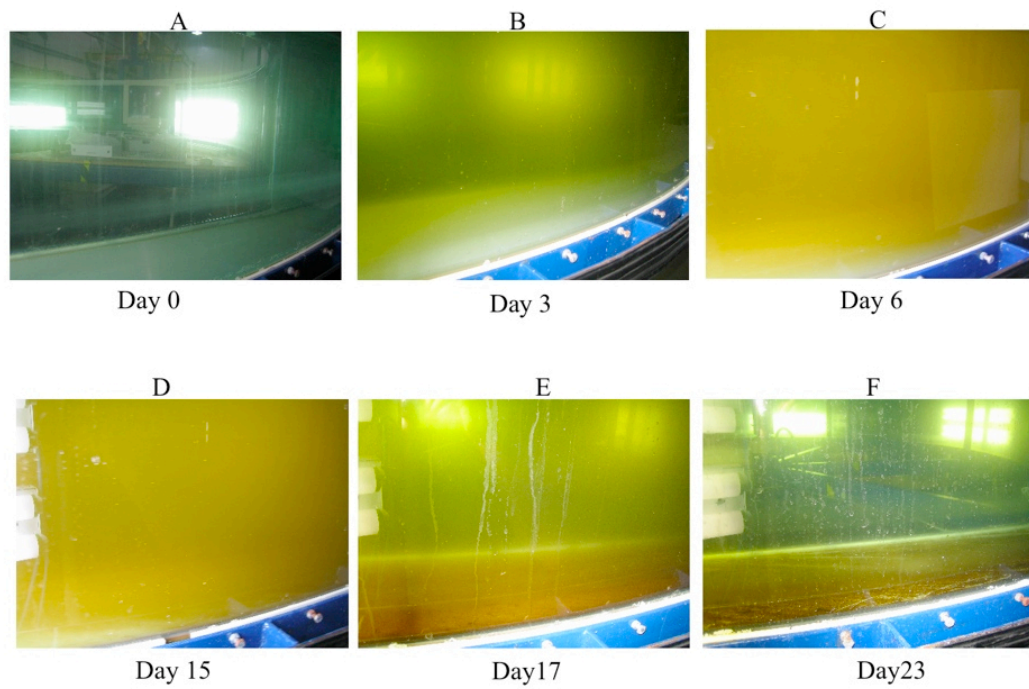


Figure 1.3 Time lapse images of the *Thalassiosira pseudonana* bloom in the annular flume.

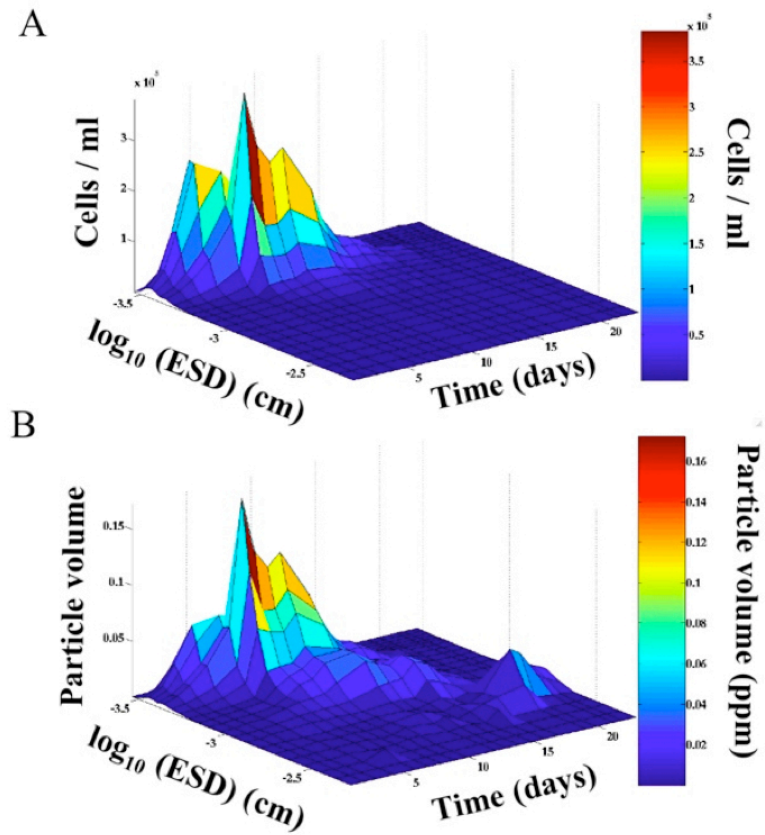


Figure 1.4, Particle size evolution during a *T. pseudonana* mesocosm experiment. A) cell concentration B) fraction volume of water occupied by cells.

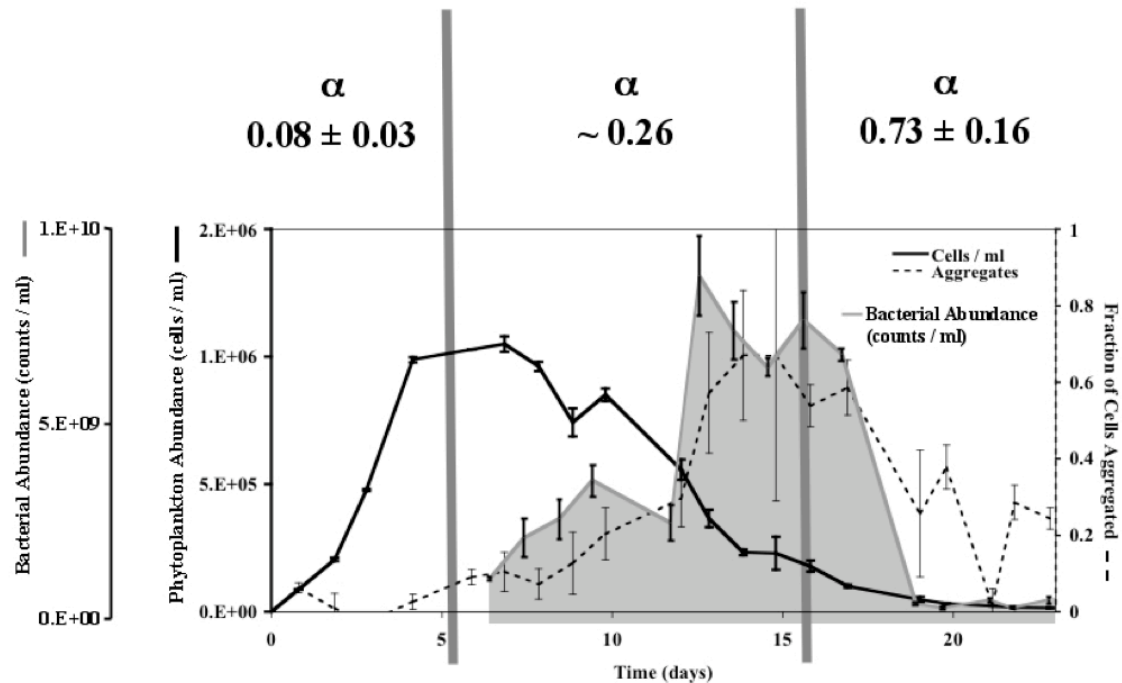


Figure 1.5, The sticking efficiency of the mesocosm was measured during the three physiologically defined phases; Initiation, Maintenance, Senescence. The cell concentration and subsequently calculated aggregated cell fraction were tracked throughout the mesocosm experiment. Enumeration of bacteria within the mesocosm was not started until the Maintenance phase.



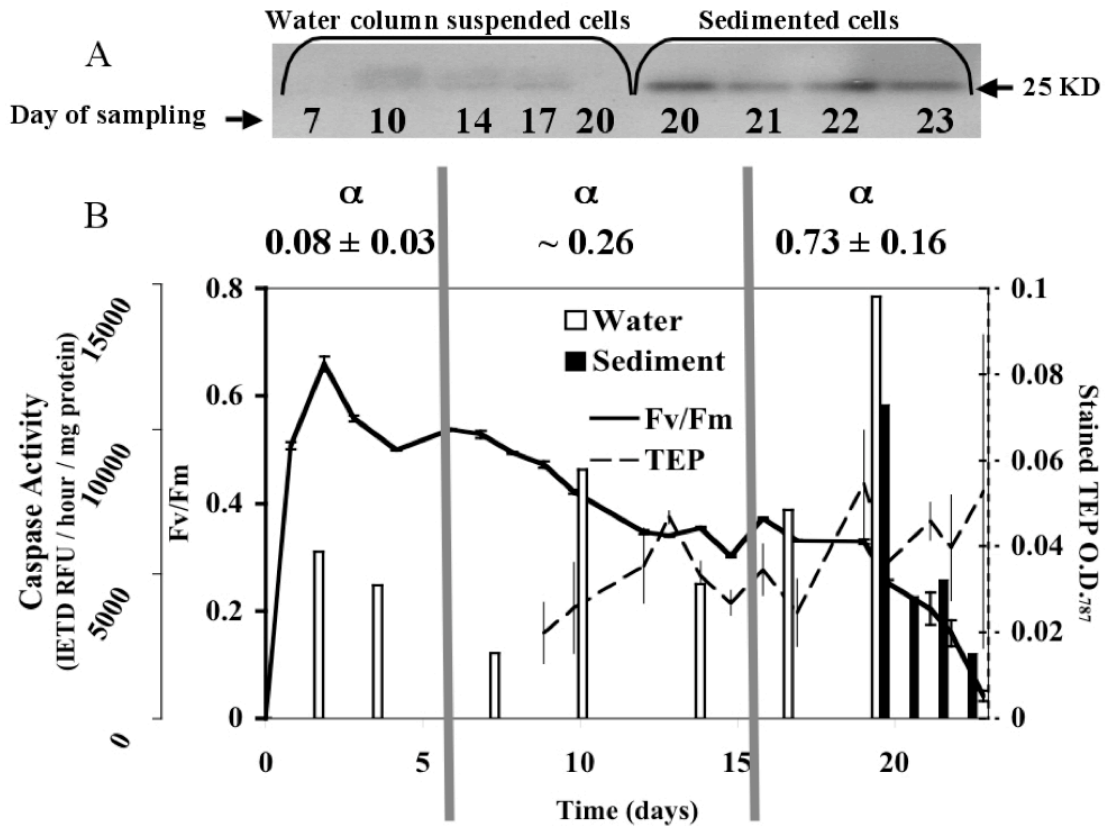


Figure 1.6, From the same mesocosm; A) a Western Blot of S.O.D. protein (band at 25kD) expression for the both water column suspended and sedimented diatom cells, and B) sticking efficiency ( $\alpha$ ) of each bloom phase is aligned with Caspase activity (for both the water column suspended and sedimented diatom cells), photosynthetic efficiency (Fv/Fm of water column suspended cells), and relative spectrophotometric TEP staining (water column only).

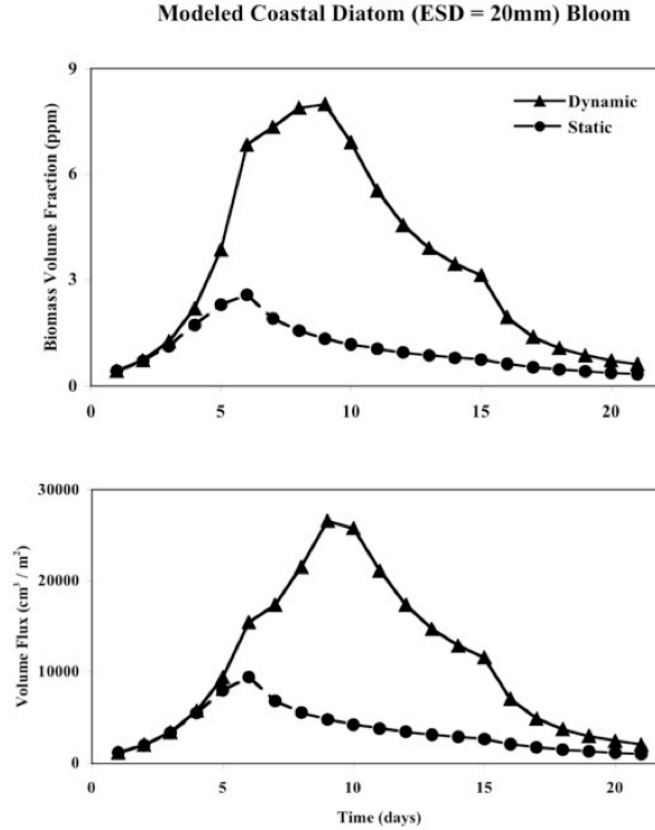


Figure 1.7, (A) volume fraction of the water occupied by phytoplankton and (B) volume export flux for a dynamic ( $\alpha = 0, 0.25, 1$ ;  $\mu = 1.8, 0.47, 0 \text{ day}^{-1}$ ) and a static ( $\alpha = 0.37$ ;  $\mu = 0.40 \text{ day}^{-1}$ ) 1-D particle aggregation model.

Growth rate and sticking efficiency were similar to our experimentally determined values from the annular flume. For each of the models, we used a rate of shear ( $\gamma = 0.1 \text{ s}^{-1}$ ) similar to the value measured in the annular flume.

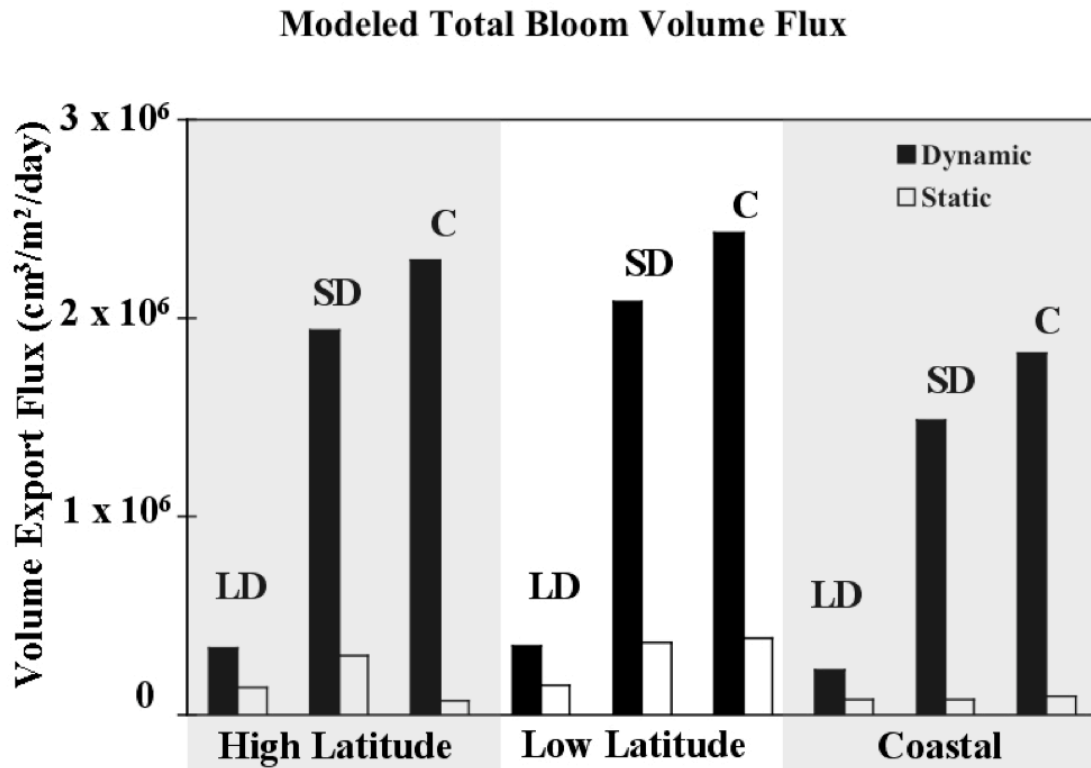


Figure 1.8, A comparison of biomass export flux between static and dynamic sticking efficiency for three phytoplankton groups in different environments.

In both the dynamic and static models, each type of phytoplankton had a size dependent growth rate that varied with the phase of the bloom (initiation, maintenance, senescence). Large Diatoms = LD ( $\mu = 0.67 \text{ day}^{-1}$ ,  $0.17 \text{ day}^{-1}$ ,  $0 \text{ day}^{-1}$ ), Small Diatoms = SD ( $\mu = 1.8 \text{ day}^{-1}$ ,  $0.47 \text{ day}^{-1}$ ,  $0 \text{ day}^{-1}$ ), Coccolithophores = C ( $\mu = 1.8 \text{ day}^{-1}$ ,  $0.47 \text{ day}^{-1}$ ,  $0 \text{ day}^{-1}$ ). For all three phytoplankton groups in the dynamic model, sticking efficiency varied with bloom phase ( $\alpha = 0, 0.25, 1$ ). Physical conditions representative of typical ocean conditions were also tested such that High Latitude ( $\gamma = 0.1 \text{ s}^{-1}$ ), and

Low Latitude ( $\gamma = 0.05 \text{ s}^{-1}$ ), Coastal ( $\gamma = 1 \text{ s}^{-1}$ ), phytoplankton blooms each had different rates of shear. Additionally, coccolithophore cells ( $\Delta\rho = 0.0355 \text{ g cm}^{-3}$ ) had a higher  $\Delta\rho$  than diatom ( $\Delta\rho = 0.0288 \text{ g cm}^{-3}$ , see Methods) cells because coccolithophore ballast ( $\text{CaCO}_3$ ) is approximately 1.23 times more dense than diatom ballast (silica).

## 2 The Nature and Role of Phytoplankton Exudate

### 2.1 BACKGROUND

Flocculation processes are enhanced by glue-like dissolved organic matter released by phytoplankton and bacteria (Alldredge et al. 1993). The rate at which phytoplankton release this dissolved organic matter is known to be variable and appears to change with the overall physiological state of the cell (Myklestad and Haug 1972). While the polymers present in large flocculated particles have variable composition, they are by-and-large composed of polysaccharides, simple sugars, proteins, and amino acids. The bulk of extracellular polysaccharides accumulate towards the later stages of the bloom during cell senescence (Guillard and Wangersky 1958) due to their continued release during all stages of the phytoplankton life cycle (Fogg 1962). These accumulating polysaccharides are altered over time due to bacterial utilization of low molecular weight algal exudates (Nalewajko and Lean 1972). However, the dynamic changes associated with the changing nature of the released dissolved organic matter, and their feed-back on the flocculation of particles remains an open question.

The degradation of polymers exuded by a diatom, *Thalassiosira pseudonana*, in batch culture was followed over each growth phase. Where previous studies have used Atomic Force Microscopy to study physical

degradation of extracellular organic matter of bulk seawater by analyzing samples at numerous depths in one location(Santschi et al. 1998), these experiments were focused on the degradation of phytoplankton exudate in laboratory controlled monospecific culture. Degradation was also followed by determination of the basic composition of the exuded organic matter during each stage of the bloom. While the specific composition of the exuded polymers may vary with growth phase (Fogg 1962), fundamental structural characteristics of polysaccharides that dominate the exudate remain independent of physiology. Considering the polymer characteristics that remain unchanged while others vary will allow for insight into the processes present over the duration of the study. This chapter brings together the impacts of the degradation of polymers exuded by phytoplankton and directly relates them to changes in algal cells with implications for the export flux of carbon from the sea surface.

## 2.2 METHODS

Measurements were made on three independent cultures of *Thalassiosira pseudonana* (CCMP 1335). The three cultures were grown sequentially over a two-month period with samples being analyzed on the same day as collection unless noted otherwise. Data were collected over the

three physiological phases (exponential, maintenance, and senescent) of the phytoplankton culture grown in F/2 (+Si) medium, using artificial seawater, under a 12:12 light:dark cycle at 17° C. The declining growth rate and stable concentration of cells, along with a slight decline in photosynthetic efficiency, together indicated the transition from exponential to maintenance phase. Beyond the exponential phase, a decline of the photosynthetic efficiency of the cultures (below 0.20) was used as the primary metric for determination of the transition from the maintenance and into the senescent phase. Mean values for each parameter from each of the three physiological phases were collected. Samples were collected for both aggregated cells at the bottom of the culture vessel and the subsequently shaken (by hand), well-mixed, cells suspended in the medium. The viscosity of both aggregated material and the well-mixed cultures were measured at least once during each physiological phase. Additionally, the sticking efficiency of two of the three cultures was measured using a Couette device during all three phases of the cultures. Low cell numbers did not allow reliable measurements of sticking efficiency during the exponential growth phase. A fourth culture was grown which was harvested to isolate and characterize organic matter released by *T. pseudonana* during the exponential, maintenance, and senescent phases of the culture. The exuded organic matter

was characterized using Fourier transform – infrared and photon correlation spectroscopies, and atomic force microscopy.

### *2.2.1 cell counts*

Phytoplankton cell counts were conducted every other day during each of the three experiments using the Multisizer 3 Coulter Counter (70  $\mu\text{m}$  aperture) as outlined in Kahl et al. (Kahl et al. 2008). Bacterial abundance was determined using the DNA stain, Acridine Orange (AO). After combining 0.5 ml of sample with 0.2 ml of AO, we filtered these stained samples onto 25 mm diameter, polycarbonate (0.22  $\mu\text{m}$  pore size) filters. These slides were observed under a mercury lighted microscope at 100x magnification.

### *2.2.2 photosynthetic efficiency*

As was done in the first chapter, each physiological phase was defined by changes in the photosynthetic efficiency of the phytoplankton cultures. Photosynthetic efficiency is often used as a proxy for the health of a phytoplankton population (Kolber and Falkowski 1993). Specifically the maximum dark-adapted efficiency of electron transport in photosystem II



( $F_v/F_m$ ) was determined using a Fluorescence Induction and Relaxation (FIRE) fluorometer (Gorbunov and Falkowski 2004).

### 2.2.3 *viscosity*

Viscosity was measured using the Couette mode of the Advanced Rheometric Expansion System (ARES). The stainless steel cup (diameter = 34 mm) rotated clockwise relative to the stainless steel bob (diameter = 32 mm, length = 25 mm) centered inside the cup. A 5 mm gap between the cup and bob was filled with samples taken from the phytoplankton cultures.

Viscosity of a sample is manifest as the fluid's resistance to flow in the rotating cup. A more viscous fluid will resist flow more readily than a less viscous fluid. As a result, the fluid in the rotating cup applies torque to the immersed bob that is proportional to the fluid's viscosity – or resistance to flow. Consequently, samples that produce more torque on the bob are more viscous than samples having comparatively less torque. The data depicting the response of the torque on the bob to the rotating cup and fluid were collected using Rheometric Scientific Instruments Orchestrator software.

Approximately 12.4 ml of aggregated and well-mixed samples were measured every 4-6 days during each experiment. The cup and bob of the Couette mode were each cleaned with acetone, milliQ water, ethanol, milliQ

water, and filtered artificial seawater prior to each measurement. Each measurement consisted of rotating the cup such that the samples were subjected to strain-controlled steady rate sweep test. The steady rate sweep test was comprised of increasing rates of shear ( $50 \text{ s}^{-1}$ ,  $100 \text{ s}^{-1}$ ,  $150 \text{ s}^{-1}$ ,  $250 \text{ s}^{-1}$ ). The viscosity at each level of shear was measured for 60 seconds and the average recorded. This measurement was repeated 3 times for every sample. Excess viscosity, the viscosity of the cultures normalized to the viscosity of filtered artificial seawater, was determined according to (Seuront et al. 2006). A xanthan gum versus viscosity standard curve was used to estimate the Xanthan Gum equivalent concentration (Passow and Alldredge 1995b) of exuded polysaccharides in each sample.

#### *2.2.4 sticking efficiency*

Following (Kiørboe and Hansen 1993) we estimated the sticking efficiency ( $\alpha$ ) of 2 of our batch cultures with a Couette device (Drapeau et al. 1994). Briefly, this method uses a defined rate of shear to increase the rate of particle interaction. As particles collide and stick to one another, individual cells form aggregates. The ability of these individual cells to adhere to one another is defined by either mechanical or physico-chemical interactions. While mechanical means such as inter-locking spines are

defined by cellular morphology, the physiology of the cell plays a large role in determining the state and composition of organic matrix coating the extracellular surface of the individual phytoplankton. Cells having a “sticky” surface will more readily aggregate compared to less “sticky” cells. When subjected to constant shear over time, the formation of aggregates from individual cells alters the slope of the particle size distribution (PSD) due to both the loss of individual cells to aggregation and the increasing number of subsequently formed larger aggregates. Accordingly, when measured at the same rate of shear, the PSD of a stickier phytoplankton will be altered more rapidly compared the PSD of less sticky phytoplankton. And because high rates of shear have been shown to break apart algal aggregates (Engel 2000), a shear rate of  $5 \text{ s}^{-1}$  was used in the Couette device. *T. pseudonana* cells used in this study had an equivalent spherical diameter (ESD) between 3 and 5  $\mu\text{m}$ . It is not known how rapidly phytoplankton sticking efficiency can change in response to changes in cell physiology or environmental conditions. However, we estimated  $\alpha$  using the measurements of the PSD made at 45, 60, and 90 minutes under the previously described culture conditions. Measurements of  $\alpha$  made during the exponential phase were unreliable because small changes in the PSD were not discernible from the measurement error at relatively low concentrations of cells.

### 2.2.5 exudate isolation and characterization

Exudate from a fourth series of *T. pseudonana* cultures was isolated during the exponential, maintenance, and senescent phases. For each phase, one liter of culture was centrifuged at 30,000x G for 20 minutes. The supernatant was combined with ethanol (1:3) and allowed to sit overnight before being centrifuged at 270x G for 4 minutes. The supernatant was removed and precipitate resuspended using 100 ml of milliQ water. The resuspended precipitate was then combined with ethanol (1:3) and subsequently centrifuged at 270x G for 4 minutes. The resulting precipitate was then freeze-dried over night and stored in a dark, cool, and dry environment until being prepared for characterization. Prior to characterization, the isolated exudate was screened for protein content (kit and standards from Pierce Biotechnology) and DNA after rehydration in milliQ deionized water (1% m:v). While the AO stain was negative (using the same AO staining methods as previously described in *cell counts*), the protein assay showed trace amounts of protein at concentrations less than the lowest standard.

Fourier–transform infrared attenuated total reflectance (FTIR-ATR) spectroscopy was used to assess the presence of functional groups in the

isolated phytoplankton exudates. In FTIR spectroscopy, a split beam of infrared light is recombined to produce an interferogram. The interferogram is reflected off the sample surface wherein the sample interacts with specific frequencies of energy. The resultant interferogram is unique to the molecules present in the sample and is analyzed using a Fourier transformation. The solid samples used in this experiment were analyzed in the solid state by placing them on an ATR crystal. Compacted, dry exudate isolate was placed on an ATR crystal in a Thermo Nicolet 670 FTIR Spectrometer (Thermo Electron Corporation). For all other methods, the isolated and freeze-dried exudate from each phase was re-hydrated with milliQ water using a mass to volume ratio of 0.1%. Subsequent to re-hydration, each of the samples was also filtered using 0.7  $\mu\text{m}$  (GF/F) syringe filters. Small amounts of salt were allowed to persist in the isolated samples to allow for more complete renaturation of the algal polysaccharides. The bulk salt concentration of each re-hydrated and filtered sample was measured and found to be: exponential = 4 parts per thousand, maintenance = 5.6 parts per thousand, and senescent phases 6 parts per thousand.

Photon correlation spectroscopy (dynamic light scattering) was used to approximate the effective diameter of the re-hydrated phytoplankton exudate. In photon correlation spectroscopy, monochromatic light is

scattered as it passes through the liquid sample medium. If the particles in the medium are smaller than the wavelength of the monochromatic light, the time-dependent scattering intensity of the monochromatic light can be autocorrelated to estimate the size distribution of the particles responsible for the light scattering. Each sample was scanned ten times for 1 minute (Brookhaven Instruments Corporation 90 plus) to calculate the average effective diameter of the algal exudates during each phase of the bloom (temperature = 25 C, scattering angle = 90°). Phase contrast atomic force microscopy (AFM) was used to a) verify the size, b) structural morphology, and c) surface characteristics of the polymers exuded by phytoplankton during the exponential and senescent phases. AFM uses a cantilever with a microscale tip which is moved across a thin film surface. The microscale tip is deflected from the surface of the film, as a result of van der Waals, electrostatic and other small-scale forces. The deflected microscale tip produces movement of the cantilever that is subsequently used to map the nanoscale topography of the film surface. Films of the isolated exudates were made by using the solution-dipping method for 1h. Silicon wafers were employed as a solid substrate to form thin films after being cleaned with piranha solution (three parts sulfuric acid per one part hydrogen peroxide). The AFM measurements were carried out in tapping mode with a

NanoScope IIIa Multimode Atomic Force Microscope (Digital Instruments, Veeco). A tapping mode etched silicon probe (TESP) silicon cantilever with a nominal spring constant 40N/m was employed to scan the surface morphology.

## 2.3 RESULTS AND DISCUSSION

All three *Thalassiosira pseudonana* batch cultures exhibited similar bloom dynamics with a peak in cell concentration coinciding with maximum photosynthetic efficiency during the exponential growth phase. At the peak of the exponential growth phase, rates of cellular division reached  $0.6 \text{ day}^{-1}$  in each of the cultures. After reaching peak concentrations the cultures entered the maintenance and then senescent phases of the bloom. During both of these latter phases the photosynthetic efficiency declined and the number of bacteria increased (fig. 2.1). Sedimented flocs of *T. pseudonana* cells began accumulating at the bottom of the culture vessels during the maintenance phase and continued to increase in concentration through the senescent phase. Rheologically, flocculated algal cells are much different than their well-mixed and suspended counterparts. The accumulated algal flocs were approximately 30% more viscous than suspended *T. pseudonana* cells (fig. 2.2). Such a noticeable increase is not unexpected. For example,

when compared to other diatoms (such as *Cylindrotheca closterium* and *Skeletonema costatum*) *T. pseudonana* is known to have the highest rate (more than ten-fold greater) of extracellular polysaccharide release (Urbani et al. 2005). Furthermore because of the poor correlation between cell concentration and viscosity ( $r^2 = 0.17$ ), and preliminary experiments using glass beads (approximately 2-10  $\mu\text{m}$  in diameter), this increase in viscosity reflects the accumulation of phytoplankton exudates in the culture medium. The highest rates of polysaccharide production in *T. pseudonana* were during the transition from exponential to stationary phase.

Coincident with elevated viscosities in the latter stages of the *T. pseudonana* bloom, was an increase in the sticking efficiency of the cells (fig. 2.2). This increase in sticking efficiency was accompanied by an increase in the accumulation of flocculated phytodetritus on the bottom of the culture vessels. Increasingly, such changes in sticking efficiency are hypothesized to be a result of changes in the quantity or quality of dissolved organic matter released by phytoplankton (Passow et al. 1994).

For the flocculated samples, the viscosity decreased as shear increased; while the data are not so clear for well-mixed samples (fig. 2.3). Fluids having a constant viscosity, such as the experimental control of clean artificial seawater (fig. 2.3) are considered to be *Newtonian*. Conversely,



fluids that become less viscous as shear increases are considered to be pseudoplastic or shear thinning. In the case of phytoplankton exudates, such shear thinning is due to the weak aggregation among copolymers rather than the breaking apart of the glycoside backbone of the exudates (Ramus and Kenney 1989). The weak aggregation of phytoplankton exudate is a result of divalent cation ( $\text{Ca}^{2+}$  or  $\text{Mg}^{2+}$ ) bridging between exuded polymers (Alldredge et al. 1993). As increased levels of shear overcome the weak cation bridging that holds together aggregated exudate, the viscosity of the solution decreases and approaches the viscosity of clean seawater. This and other work on non-Newtonian behavior in phytoplankton blooms suggests that visco-elastic properties might be used to estimate bulk bio-rheological attributes of seawater (Jenkinson 1986). Because the *thinning* or non-Newtonian behavior of seawater containing phytoplankton exudates is proportional to polysaccharide concentration, the measured viscosity of gum xanthan was used to form a standard curve to estimate the range of concentration of the unknown acidic polymer exudates responsible for the increase in culture viscosity (fig. 2.3). Despite gum xanthan being a relatively stiff polymer, it was used for the standard curve because of its widely accepted use in standard curves for the Alcian Blue staining technique for TEP (technique described in chapter 1). As a result, *T.*

*pseudonana* released approximately 1 mg of polysaccharide per liter of seawater per week over the duration of the experiment. Although our data do not show whether this rate remained constant throughout the bloom, the accumulation of these polysaccharides lead to the significantly increased viscosity of flocculated algal cells compared to the well-mixed culture (fig. 2.3). These concentrations of algal exudates fall within the range of previously reported values in both cultures and nature (Mykkestad 1995). Despite its comparatively stable viscosity, there was a statistically significant increase in the viscosity of the well-mixed culture towards the end of the bloom. However, using the viscosity of the *T. pseudonana* cultures, compared to the standard curve of xanthan gum, revealed that only relatively large changes in polysaccharide concentration can produce measurable changes in viscosity (fig. 2.3). This may prove useful in scenarios where phytoplankton exudation is much higher than can be reliably measured using other traditional methods such as Alcian Blue staining.

In addition to their effect on the rheology of the surrounding medium, the composition of the isolated exudates was also assessed. Exudates from each growth phase were analyzed by Eric Andrianasolo using mass spectroscopy. The exudates from each of the three phases were comprised of

polymers with molecular masses less than 800 Daltons (Fig 2.4). These data are in agreement with previous work showing that the majority of algal exudates have a molecular mass less than 900 Daltons (Jensen 1983). Using FT-IR, the isolated exudates (fig. 2.5) show the C-O stretching in alcohols ( $1200 - 950 \text{ cm}^{-1}$ ) and H-bonded O-H stretching ( $3400 \text{ cm}^{-1}$ ) characteristic of polysaccharides (Leandro et al. 2003). The peaks near  $2400 \text{ cm}^{-1}$  are likely a result of the principally sulfonic, and perhaps uronic acids present in the polysaccharide isolates. Of particular importance when comparing the spectra from each of the three growth phases is the loss of  $\beta$ -glycoside linkages (vibration bands ca.  $880 - 900 \text{ cm}^{-1}$ , Synytsya et al. 2003), which were present during the exponential phase but were not detectable in isolated polysaccharides taken from the maintenance or senescent phases (fig. 2.5). Similarly,  $\alpha$ -glycoside linkages (vibration bands ca.  $825 - 860 \text{ cm}^{-1}$ , Synytsya et al. 2003) were also present during the exponential phase yet were barely detectable during the latter bloom phases. Both  $\alpha$ - and  $\beta$ -glycoside linkages bond sugars to one another and other molecules forming the backbone of many polymers. Such deterioration is likely responsible for the transition from discrete large particles of exuded polysaccharide (fig. 2.6, *Exponential Phase*) into a less discernible organic matrix (fig. 2.6, *Senescent Phase*). Marine bacteria associated with aggregates of phytoplankton and

marine snow use hydrolytic ectoenzymes such as  $\alpha$ - and  $\beta$ - glucosidases to break down and utilize phytoplankton exudates (Karner and Herndl 1992). The bacterial degradation and utilization of these polymers is can account for both the increase in bacterial cells (fig. 2.1) and the reduction in viscosity (in flocculated cells) from maintenance to senescence (fig. 2.2). Together with the loss of predictability of the non-Newtonian behavior during the transition from maintenance to senescent phase, these AFM images indicate that *T. pseudonana* exudates were altered from discrete structures into a film composed of degraded polymer. The morphology of diatom exudates is diverse and can range from discrete structures such as stalks, pads, tubes, or fibrils to amorphous films (Hoagland et al. 1993). The exponential phase *T. pseudonana* exudates studied resembled pads that subsequently degraded to an amorphous film by the senescent phase. Such an amorphous film may provide the foundation for marine polymer gels. Marine polymer gels (such as transparent exopolymer products, or TEP) can spontaneously assemble from free dissolved organic matter polymers, resulting in an increase in particle size over time as gels aggregate and anneal – while bulk concentration remains constant (Chin et al. 1998).

Because of the severely degraded surface of the amorphous exopolymer imaged using AFM during the senescent phase, photon

correlation spectroscopy was used to approximate the size of the polymers. As the bloom aged, the size of the exuded polymers increased from having an effective diameter of  $449 \pm 15$  nm (exponential phase) to an effective diameter of  $774 \pm 192$  nm (senescent phase) (fig. 2.7). Together with the AFM imagery, it is not clear from these data whether or not the senescent phase polymer is composed of a) larger amorphous particles having a rougher or more degraded surface, or b) if the senescent phase is composed of multitudes of smaller particles interacting as larger amorphous particles. In either case, the bulk behavior of the senescent phase polymers, and their interaction with particles is the same. And, despite the increase in polymer size, the concentration of exuded polymer in the artificial seawater medium remained relatively constant from the maintenance to the stationary phase. The relatively stable polysaccharide concentration in the well-mixed samples and increasing size of exuded polymers observed in this experiment fit the model of marine gel formation.

Changes in viscosity and sticking efficiency are related to wide-spread changes in the rheological properties of the environment surrounding phytoplankton cells. The rheology of the medium changed as a result of both the accumulation and composition of the exudate. Consequently, algal exudates may be able to attenuate the export flux of carbon from the sea

surface by altering the rheology of the surrounding medium. In particular, the Stoke's settling velocity of particles could be affected by changes in the viscosity of the ocean.

In the well-mixed culture, viscosity increased 8% from bloom initiation into senescence. Using a simple 1-dimensional particle interaction – export flux model (Jackson 1990), parameterized as in (Kahl et al. 2008) the impact of an 8% increase in viscosity of seawater was estimated. When applied to the 1-D export flux model, the observed changes in the viscosity of well-mixed phytoplankton cultures, resulted in a 7% decrease in the export flux from coastal (high shear) and a 25% decrease in open ocean (low shear) conditions. The decrease in export flux as viscosity increases is a result of the resultant reduction of particle-particle interactions arising from differential settling. The net effect of an increase in viscosity is to reduce the difference in settling speed between small and large particles. Where the Stokes settling velocity is inversely proportional viscosity (Stokes' settling  $\propto (\text{particle diameter})^2 (\text{fluid viscosity})^{-1}$ ), an increase in the viscosity causes a small change in settling speed for a small particle, and a large change in settling speed for a large particle. As viscosity increases, and the settling speed between two different sized particles converges, the probability of the two particles coagulating due to differential settling also declines. As a

result, in a low shear environment where differential settling is the dominant form of particle interactions, viscosity variability can have significant effects on export flux.

Illuminating the changing nature and characteristics of phytoplankton exudates allows for a mechanistic understanding of the processes governing the ocean's biological pump. As phytoplankton release discrete polymers into the surrounding medium, the polymer-exudates are degraded by bacteria, resulting in a morphological change in the exudate. The phase-transition of polymer-exudates from discrete particles into web-like marine gel enables entrainment of other particles. Rather than the polymer-exudates being sticky upon their introduction into the extracellular medium, it is their degradation that results in improved particle entrainment. This increasing ability to *catch* other particles is manifest as an increase in the apparent sticking efficiency of phytoplankton. In addition to affecting bloom dynamics and export flux via altering the sticking efficiency, the algal exudates also attenuate export flux by reducing the settling velocity of smaller particles via an increase in seawater viscosity. And, while overall ocean carbon export dynamics can be either compounded or diminished by the release of exudates by phytoplankton, and understanding of these small-scale dynamics will be crucial as we move towards further understanding

and potential regulation of sequestering carbon from the atmosphere to the bottom of the ocean.



## 2.4 FIGURES

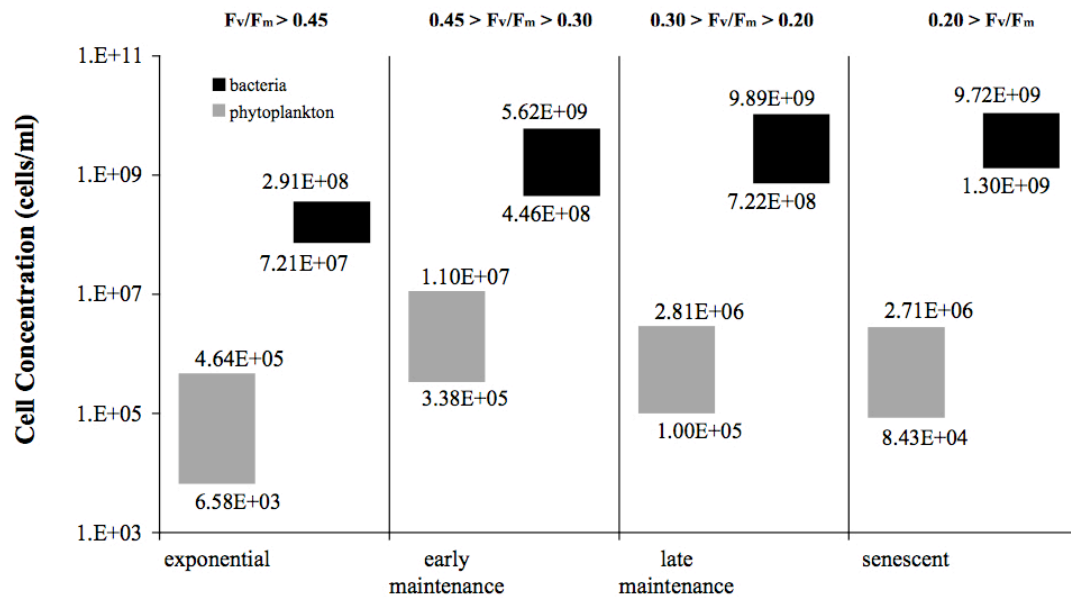


Figure 2.1, Combined results of three *Thalassiosira pseudonana* batch cultures. Each phase of the cultures were classified into characteristic bloom stages based on growth rate, cell concentration, and the photosynthetic efficiency (variable fluorescence normalized to maximum fluorescence,  $F_v/F_m$ ) of *T. pseudonana*. The range, including minimum (below color bars) and maximum (above color bars) values, of cell counts for both bacteria and *T. pseudonana* are presented.

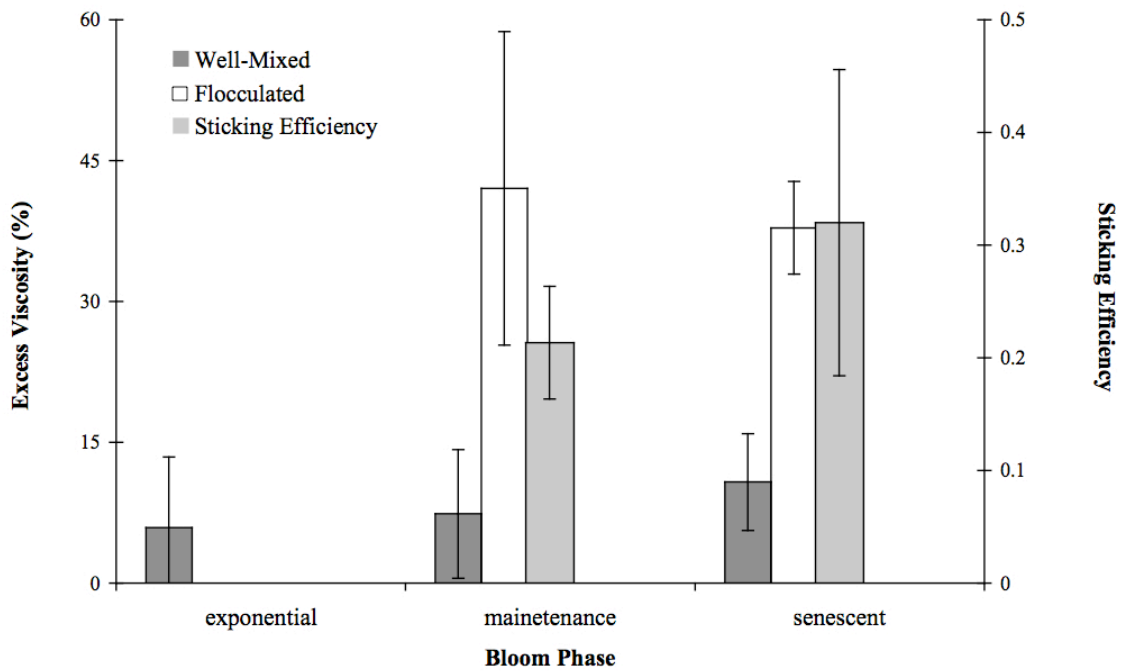


Figure 2.2, Sticking efficiency (measured at  $5 \text{ s}^{-1}$  in a Couette device) of the well-mixed *Thalassiosira pseudonana* culture increased as the bloom progressed from the maintenance to the senescent phase (d.f. = 6,  $P = 0.077$ ). Excess viscosity (viscosity of cultures normalized to clean artificial seawater) of the well-mixed *T. pseudonana* culture (measured at  $50 \text{ s}^{-1}$ ) increased during the end of the senescent phase (d.f. = 6,  $P = 0.068$ ). Flocculated *T. pseudonana* cells were significantly more viscous than both clean seawater and well-mixed samples of the same cultures during the maintenance (d.f. = 13,  $P < 0.001$ ) and senescent phases (d.f. = 4,  $P =$

0.002 ). Measurement of flocculated cells during the exponential phase was precluded by the onset of cell flocculation during the maintenance phase.

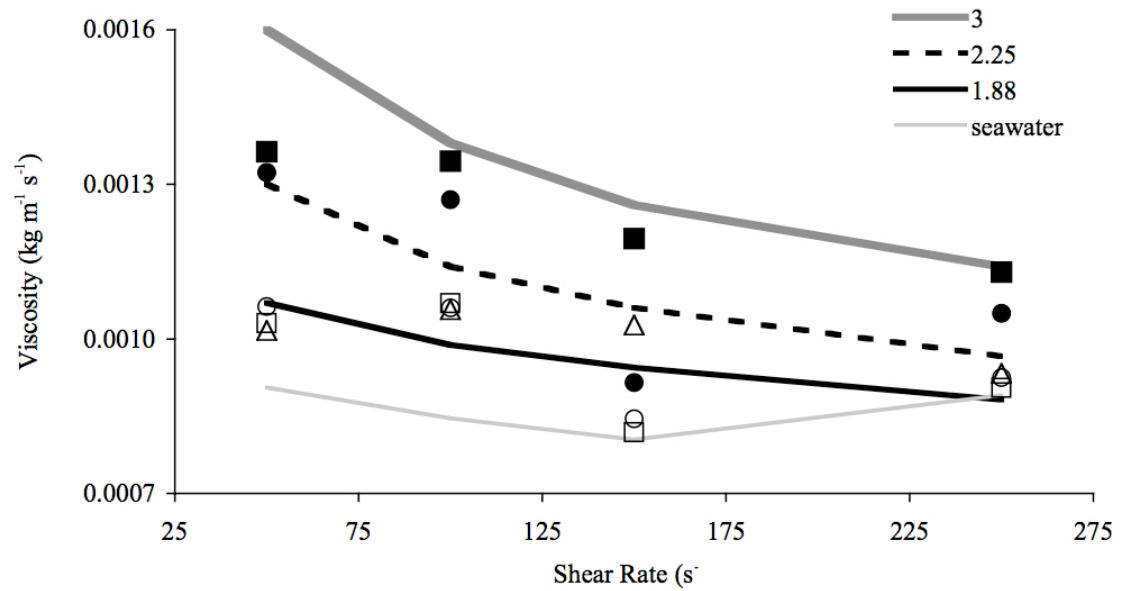


Figure 2.3, Rheology of *Thalassiosira pseudonana* exudates (well-mixed culture:  $\triangle$  = exponential,  $\square$  = maintenance,  $\circ$  = senescent; and flocculated cells:  $\blacksquare$  = maintenance,  $\bullet$  = senescent) compared to a clean artificial seawater control and Xanthan gum standards (1.88, 2.25, and 3.00 mg liter<sup>-1</sup>). Both the phytoplankton exudate and Xanthan standards exhibited non-Newtonian behavior (viscosity varies with shear rate).

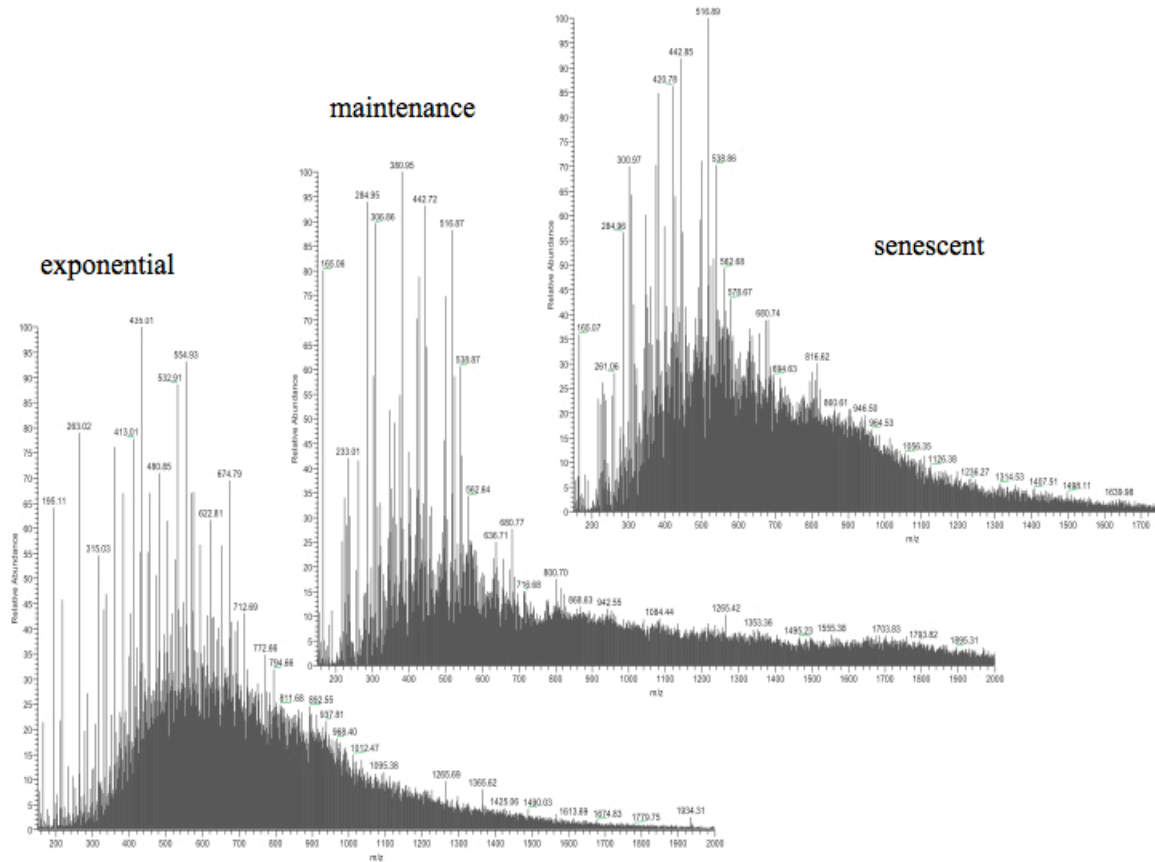


Figure 2.4, Mass spectrometry of isolated *Thalassiosira pseudonana* exudates sampled during the exponential, maintenance, and senescent phases.

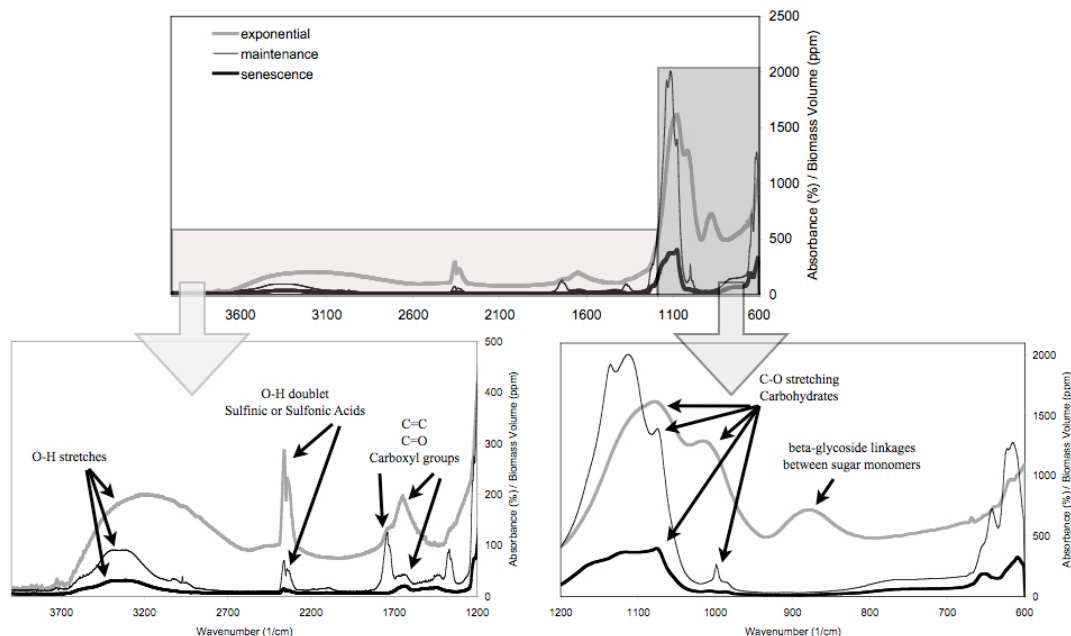


Figure 2.5, Fourier-Transform Infrared Spectroscopy spectra of the exudates isolated from *Thalassiosira pseudonana* during the exponential, maintenance, and senescent growth phases. Beta-glycoside linkages between monomers are present in exudates during the exponential growth phase but were not detected during the maintenance or senescent phases.

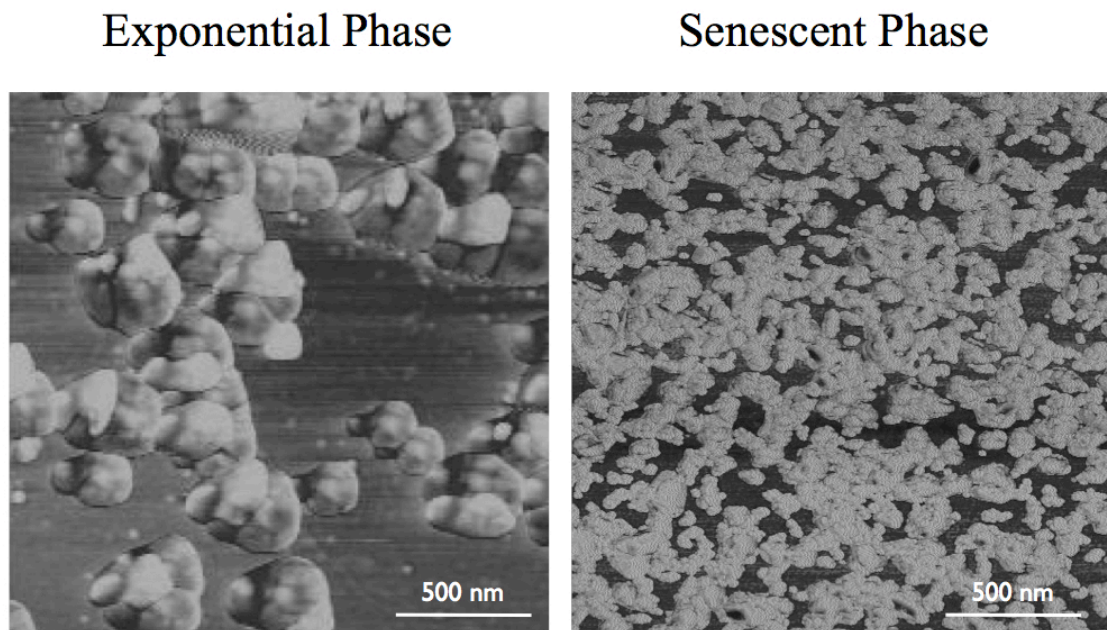


Figure 2.6, Atomic Force Microscopy images comparing the size and morphology of *Thalassiosira pseudonana* exudate during the beginning (Exponential Phase) and end (Senescent Phase) of a typical bloom progression. Early in the bloom, during the Exponential Phase, exudates are comprised of discrete polysaccharide particles. By the end of the bloom, during the Senescent Phase, the discrete particles have been degraded into a net-like organic matrix.

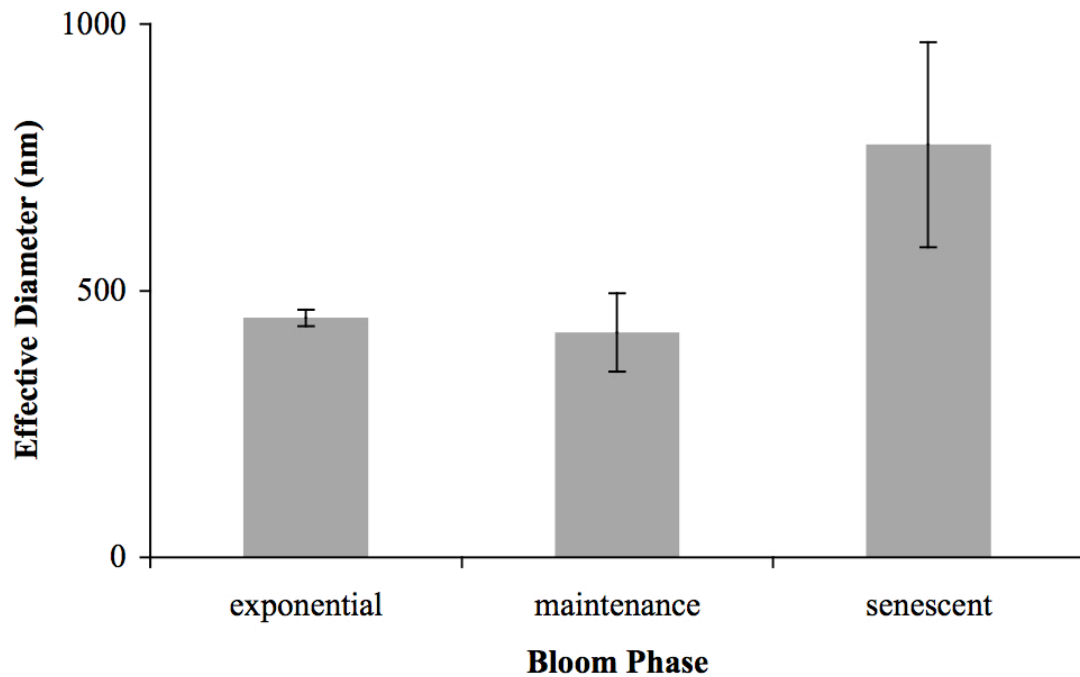


Figure 2.7, The effective diameter of isolated algal exudates, from *Thalassiosira pseudonana*, changed from smaller more uniformly distributed particles ( $449 \pm 15$  nm) to a larger apparent particle size having a more heterogeneous ( $775 \pm 192$  nm) distribution as the culture aged (d.f. = 9,  $P < 0.001$ ).



### **3 Physiology and Exudation, a Model**

#### **3.1 BACKGROUND**

The efficiency of phytoplankton aggregation, or “stickiness”, and the magnitude of the subsequent flux of carbon is affected by phytoplankton physiology (Kiørboe et al. 1990). The mechanisms underlying these physiological changes are not well understood but are presumed to be a result of an imbalance between photosynthesis and nutrient availability. Both light (Fogg et al. 1965) and nutrient stress (Myklestad and Haug 1972) are well-known triggers of increased dissolved organic carbon (DOC) release by phytoplankton. As explored in the first two chapters, the DOC released by phytoplankton is subsequently responsible for controlling the cell’s sticking efficiency. Without an understanding of both the mechanism and associated physiology of dissolved organic matter release, it is difficult to gauge the true effect of phytoplankton sticking efficiency and its subsequent impact on carbon dynamics (via aggregation/ sedimentation or simply the loss of dissolved organic carbon to the water column). There are two simple mechanistic models that describe the release of organic matter from phytoplankton; the overflow and leakage models. (Nagata 2000). The overflow model predicts that organic matter is released from cells as a result of carbon fixation that exceeds the rate of incorporation into cellular material

while the leakage model suggests a concentration gradient-driven passive permeation of low molecular weight materials across the cell wall (Stadelmann 1962). The leakage and overflow models apply to the loss of intracellular simple sugars, amino acids, and other low molecular weight molecules via diffusion through the cell plasmalemma (Hellebust 1974). Larger molecules such as polysaccharides, or proteins are likely liberated from the cell via more complicated excretion schemes possibly involving the Golgi complex (Ramus and Robins 1974) and/or the fusion of intracellular vesicles (Chin et al. 2004).

The overflow and leakage models are simple and mechanistic, and can be thought of as passive mechanisms of organic matter release from phytoplankton. Conversely secretion or exocytosis is an active mechanism of organic matter release from phytoplankton. The accuracy and/or relative roles of the two passive mechanisms, and the possible role of at least one active mechanism, of organic matter release by phytoplankton are not known. As a result, previous phytoplankton physiology models acknowledge the need for, but do not explicitly define, the loss of DOC from the cell (Flynn and Martin-Jézéquel 2000) (Geider et al. 1998). The goal of this chapter is to explore a hitherto ignored facet of phytoplankton physiology models. The chapter also aims to provide a basic framework, despite its

obvious shortcomings, within which to construct a more complete model of phytoplankton physiology and exudation which for future empirical comparison.

### 3.2 MODEL DESCRIPTION

As a first step towards assessing the viability of either of the passive models of organic matter released by phytoplankton, a two – box model was devised to represent the carbon budget of a single phytoplankton cell over time (fig. 3.1 and table 3.1). The carbon budget of the cell is balanced by the assimilation of carbon as biomass and the loss of carbon via respiration and excretion. Inorganic carbon assimilation relies on the rates of both photosynthesis and bioavailable nitrogen uptake. And, while respiration is set at a constant value, excretion (or exudation) is driven by the intra-to extra- cellular concentration gradient of organic carbon.

#### *3.2.1 carbon pathways into and out of the cell*

The equation for photosynthesis ( $f_L$ ) – converting inorganic extracellular carbon into phytoplankton biomass (Herzig and Falkowski 1989), with units of mol carbon assimilated per time, is written as equation 3.1:

$$(3.1) \quad f_L = a^* \cdot \frac{Chl}{PQ} \cdot PAR \cdot \phi_{\max} \tanh\left(\frac{\alpha \cdot E_{\mu}}{P_{\max}}\right)$$

Where  $a^*$  is the spectrally averaged optical absorption cross-section normalized to Chl a; Chl is the mass of Chlorophyll per cell;  $PAR$  is the Photosynthetically Available Radiation between 400-700nm;  $\phi_{\max}$  is the maximum quantum yield;  $\alpha'$  is the light utilization efficiency or slope of the PE curve;  $E_{\mu}$  is the incident growth irradiance;  $P_{\max}$  is the photosynthetic capacity (see table 3.2 for overview of symbols). For this study,  $E_{\mu}$  followed a 14:10 hour, daily light:dark cycle. Furthermore, as the particle, or cell, concentration ( $P$ ) within the model increased above the critical particle concentration value ( $P_{crit} = 10^5 \text{ cells (ml)}^{-1}$ ), the  $E_{\mu}$  becomes increasingly limited (eq. 3.2).

$$(3.2) \quad E_{\mu} = E_0 \left[ 1 - \sin\left(\left(1 - \frac{P_{crit}}{P}\right) \frac{\pi}{2}\right) \right]$$

Nutrient uptake (eq. 3.3) was modeled using Michaelis-Menten uptake kinetics parameterized as in (Klausmeier et al. 2004).

$$(3.3) \quad f_N = \frac{V_{\max,N} \cdot N_{in}}{N_{in} + K_N}$$

The maximum uptake rate of nitrogen ( $V_{\max,N}$ ) in the model is  $\mu\text{mol N cell}^{-1} \text{ day}^{-1}$ . Where  $N_{in}$  is the input nitrogen concentration assigned at the

beginning of the model ( $\mu\text{mol N L}^{-1}$ ) and the nitrogen half-saturation constant ( $K_N$ ) is  $0.86 \mu\text{mol N L}^{-1}$ .

Because of the simplicity of the cell in this model, it is not possible to incorporate a more complex model of exocytosis of polysaccharides. Rather, a simple formulation for the passive release of exudates (eq. 3.4) follows the model proposed by (Bjørnsen 1988). This model provides a *leakage*, or excretion, rate that is proportional to the concentration of the *Reserve* box relative to the extracellular concentration of organic carbon.

$$(3.4) \quad f_E = \Delta C \cdot \frac{SA}{V} \cdot k_p$$

Where  $\Delta C$  is the concentration of polysaccharides outside and inside the cell ( $C_M - C_R$ ),  $k_p$  is the permeability coefficient of the cell wall ( $10^{-7} \text{ cm (s)}^{-1}$ , Raven 1984), and the middle of the equation is the surface area (SA) to volume (V) ratio of the cell. Additionally, if the *Structure* of the cell is not maintained at its initial value, the permeability coefficient linearly increases in proportion to the loss of cell structure integrity. Conversely, the *Structure* of the cell can be repaired if light and nitrogen are sufficient. As a result, as external nitrogen is depleted, or light becomes diminished, and the model progresses into nutrient or light stressed conditions (external concentration  $< 5 \mu\text{mol}$  and/or light  $< 1500 \mu\text{E m}^2 \text{ sec}^{-1}$ ), the cell becomes increasingly leaky. However, this reduced cellular integrity and subsequent leakiness can

be ameliorated or repaired under replete nitrogen and ample light conditions. Increased rates of extracellular release are characteristic of phytoplankton when photosynthesis is depressed (Zlotnik and Dubinsky 1989).

### 3.2.2 carbon pathways within the cell

Within the cell, carbon resides in either the Structure ( $C_S - C_L$ ) or the Reserves ( $C_R$ ). Each of these pathways are shown in figure 3.1, and are defined as (where  $dt = t_2 - t_1$ );

Cell structure (eq. 3.5)

$$(3.5) \quad C_S - C_L \geq f_{BS}(dt) \text{ where } \begin{cases} f_{BS}(dt) = (f_N + f_{PB} + f_{RB})(dt) \\ f_{PB}(dt) \leq f_L(dt) \\ f_{RB}(dt) \leq (f_{BS} - (f_{PB} - f_{RB}))(dt) \end{cases}$$

Cell reserves (eq. 3.6):

$$(3.6) \quad C_R = (f_{PR} - f_{RB} - f_E)(dt) \text{ where } \begin{cases} f_{PR}(dt) = (f_L - f_{PB})(dt) \\ f_{PB}(dt) \leq f_L(dt) \\ f_{RB}(dt) \leq C_R \\ f_E(dt) \leq C_R - f_{RB}(dt) \end{cases}$$

The model is driven by loss of carbon ( $C_L$ ) from the cell Structure ( $C_S$ ) which also includes the cell membrane. The initial size of  $C_S$  is based on empirical measurements of total cellular protein. Because protein in a cell

does not significantly vary with irradiance, an empirical value of 120 pg per cell was used to initialize the biomass of the cell (Post et al. 1985). Typically cellular proteins contain about 77% carbon and 22% nitrogen (Spoher and Milner 1949). Accordingly, for nutrient uptake, the model assumes 3.5 mol carbon per 1 mol nitrogen (molar C:N = 3.5).

The loss of carbon from the cell structure due to respiration ( $C_L$ ) is constant, and equal to the amount of carbon that could be fixed at a nitrogen concentration of 5  $\mu\text{mol}$  and with incident growth irradiance at 1500  $\mu\text{E (m}^2 \text{ sec)}^{-1}$ . While this minimum uptake quota is maintained, the cell can grow, accumulate excess fixed carbon the *Reserve* and potentially divide. As a result, if the external nutrient supply matches the minimum uptake quota, (5  $\mu\text{mol}$  nutrients and 1500  $\mu\text{E (m}^2 \text{ sec)}^{-1}$ ) the cell carbon budget will remain at a steady state. Deviation from these conditions causes a perturbation in the intra-cellular carbon budget. When light and nutrients are both adequate, and the cell has replaced  $C_L$ , any excess photosynthate is placed into the *Reserve* wherein it is either *leaked* from the cell or utilized by the cell during less favorable light conditions (fig. 3.2).

The maximum fixed carbon quota of the *Reserve* is two times that of the *Structure*. When light and nutrients are ample, the integrity of the cell *Structure* is not compromised, and the *Reserve* maximum quota is met the

model cell divides into two cells (eq. 3.7). With the equivalent of three times the biomass of an individual cell between them, each subsequent cell thus begins with an equal allocation of the maximum *Structure* carbon quota and a *Reserve* containing  $\frac{1}{4}$  the maximum *Structure* carbon quota.

$$(3.7) \quad P(t) = P_0 2^{ft}$$

Where  $P_0$  is the initial population size ( $10^3$  cell  $\text{ml}^{-1}$  in this study),  $P(t)$  is the population (cells  $\text{ml}^{-1}$ ) at time  $t$ , and  $f$  is the frequency of cell division ( $\text{time}^{-1}$ ). The frequency of cell division is regulated by cell size. In particular,  $f$  is proportional to the surface area to volume ratio of the cell such that smaller cells divide more rapidly than larger cells. As a result, the maximum abundance of phytoplankton cells was constrained to scale inversely with cell size (Belgrano et al. 2002).

The above-described physiology/exudate model was used to assess bloom exudation characteristics of large (equivalent spherical diameter = 20  $\mu\text{m}$ ) and small (equivalent spherical diameter = 5  $\mu\text{m}$ ) cells. Blooms of each cell size were modeled under each combination of high/low light and high/low nutrients (fig. 3.3 - fig. 3.10). High light was defined as having a maximum irradiance of  $2500 \mu\text{E m}^{-2} \text{s}^{-1}$  while low light irradiance was  $1500 \mu\text{E m}^{-2} \text{s}^{-1}$ . The initial bioavailable nitrogen concentration of the high



nutrient models was 30  $\mu\text{mol}$  while the low nutrient scenario had an initial concentration of 15  $\mu\text{mol}$ .

### 3.3 RESULTS AND DISCUSSION

Phytoplankton typically release 10% to 32% of their total organic carbon into the surrounding medium (Biddanda and Benner 1997). By comparison, the coupled physiology and exudate model predicted maximum fractions of cellular carbon release ranging from between 7% and 21% of total cell carbon (table 3.3). In all four sets of conditions, small cells had a higher fraction of extracellular release of their total cellular carbon.

Additionally, small cells ( $15\% \pm 5\%$ ), on average, had a higher fraction of exudate than large cells ( $9\% \pm 2\%$ ). One reason small cells in the coupled model released more carbon than large cells was because large cells tend to self-shade their chloroplasts. The phenomenon of self-shading was manifest in the  $a^*$  of large cells ( $0.01 \text{ m}^2 (\text{mg Chl a})^{-1}$ ) being 2.5 times less than that of small cells ( $0.025 \text{ m}^2 (\text{mg Chl a})^{-1}$ ). The smaller  $a^*$  of large cells leads to less efficient utilization of PAR. As a result, large cells assimilate extracellular carbon at a lower rate than small cells. A slower rate of carbon assimilation has two primary effects on cellular physiology; slower growth rates and less excess carbon available for the intracellular *Reserve* pool.

Accordingly, in the model, simulations with higher rates of carbon assimilation drew down external nutrients much faster than slower growing populations (fig. 3.3 & fig. 3.4).

The *Structure* of the cell begins to degrade when external nutrients fall below the minimum uptake quota. And, because the external nutrient supply does not meet the minimum uptake quota, *Structure* degradation begins at an earlier point during the bloom of the faster growing small cells. The earlier (and irreversible – due to nutrients only being supplied at the beginning of the bloom) onset of *Structure* degradation caused small cells to leak a higher fraction of their *Reserve* pool compared to large cells (table 3.3). These results reflect the oft-cited imbalance between light and nutrients as the cause for an increased DOC to biomass or particulate organic carbon (POC) fraction (Nalewajko and Lean 1972).

In addition to the high rate of carbon assimilation in small cells, the results of this model also indicate that cell size (i.e. surface area to volume ratio) is important. Under identical light and nutrient conditions, as the cell's *Structure* is prematurely compromised due to a nutrient-light imbalance, small cells release more DOC when compared to larger cells (fig. 3.3 - fig. 3.10). Small cells are increasingly susceptible to higher rates of DOC loss because of their higher surface area to volume ratio. These results mirror

observations that DOC release by phytoplankton is not proportional to biomass production (Smith and Wiebe 1976). Indeed, within oligotrophic systems which tend to be dominated by small cells, a larger fraction of fixed carbon resides as DOC rather than particulate organic carbon (POC) when compared to more productive waters that tend to be dominated by larger cells (Watt 1966). Small cells commonly found in oligotrophic waters, such as *Trichodesmium*, rapidly respond to stress by producing extracellular DOC (Berman-Frank et al. 2007). These data would imply that *less productive* waters have higher percentage of fixed carbon released as DOC because of the higher surface area to volume ratio of small cells, that tend to dominate oligotrophic systems. However, despite earlier chapters' emphasis on the role of extracellular DOC in improving export flux efficiency, the relative fraction of fixed carbon released as DOC by smaller cells may not necessarily translate into a more efficient biological pump.

Because phytoplankton exudates are precursors to aggregate inducing TEP, a population of cells producing large quantities of exudate will aggregate more efficiently (Passow 2000). However, as discussed in Chapter 1, the timing and rate of aggregation are fundamental to the successful export of carbon from the sea surface. The effects of coupled cell growth and exudation (as predicted in the coupled physiology/exudate model) were

subsequently used to initialize the growth rates and sticking efficiency of the 1-D export flux model (Jackson 1990). As explored in Chapter 2, the relationship between sticking efficiency and exudate depends on both the quality and concentration of phytoplankton-released extracellular DOC. Because the ratio between exuded DOC and phytoplankton is a primary factor in the onset of flocculation in phytoplankton blooms (Passow and Alldredge 1995b), the cumulative fraction of cellular carbon exuded during each physiological phase of the bloom was used to parameterize sticking efficiency (table 3.4). Physiology – exudation models typical of two contrasting ocean export flux study sites, were used to assess the coherence of predicted model dynamics with those observed in the ocean. Large cells exposed to high light and high nutrients (fig. 3.3) are characteristic of the north central Pacific station K2, while small cells under high light and low nutrients typify the tropical Pacific site at station ALOHA (fig. 3.8).

Despite the K2 simulation leading to a flux (at 65 meters depth) of carbon that was 125 times larger than that simulated for ALOHA, both simulations roughly paralleled observed patterns of particle size distribution volume flux at both stations (fig. 3.11 & fig. 3.12, note that the z-axis color scales are different). Where K2 is typified by a pronounced export flux event consisting of larger aggregates, and ALOHA exports carbon via a more

steady particulate rain, there is only a 2.5 – fold difference in export efficiency (Buessler et al. 2007). Although the specific timing of the events is likely inaccurate, the similarity of the simulated and real-world environments indicates that the underlying mechanisms are somewhat realistic. Similar to Chapter 1, the interplay between cell concentration, and the variability of phytoplankton sticking efficiency are primarily responsible for the variability in export flux between the two stations. The early onset of a high sticking efficiency regulates the critical concentration of phytoplankton cells such that biomass is prevented from accumulating via a slow and steady rain of small aggregates. Meanwhile, a delayed increase in sticking efficiency allows biomass to increasingly accumulate prior to a large flocculation event anteceded by a spike in carbon export. The specific nature of each type of event is characterized by the mean settling velocity, as determined by the average size of aggregated cells, over the course of the simulations. The settling velocity of the K2 simulation clearly spikes at the same time as the peak in the volume flux (fig. 3.11). On the contrary, the settling velocity of the ALOHA simulation peaks at the beginning and declines initially before stabilizing for the duration of the bloom (fig. 3.12).

Although the agreement in underlying dynamics of export flux at each site, comparatively, the simulations present a more exaggerated difference in

volume flux between the north central and tropical Pacific. One possible reason that the K2 simulation is two orders of magnitude too high, relative to the ALOHA simulation, is because the oligotrophic parameterization used in this study over-predicts the sticking efficiency during the early stages of the bloom. A lower initial sticking efficiency during the exponential phase of the ALOHA simulation would have allowed biomass to increase which would in turn lead to increased export flux. However, estimating the amount by which to decrease the initial sticking efficiency of the ALOHA simulation would require the incorporation of yet another complex mechanism.

At station ALOHA, the high fraction of fixed carbon as DOC, provides a tight coupling between primary production and heterotrophic bacteria. Because heterotrophic bacteria rely on extracellular DOC from phytoplankton as a primary energy source (Azam et al. 1983), station ALOHA would have a smaller fraction of fixed carbon as DOC than these simulations predict. Incorporating DOC heterotrophy by bacteria into the model would likely improve relative agreement between the simulations and observed values of export flux.

A rudimentary but realistic cellular physiology and exudation model was devised to explore the role of light and nutrients in the release of

extracellular DOC by large and small cells. While both light and nutrients are important drivers of phytoplankton exudation, the model revealed that cell size also plays a crucial role in linking these processes to the surrounding ecosystem. The linkages between these processes will be further studied in the next version of this model by substituting Lambert Beer's Law for equation 3.2. In particular, empirically derived specific light attenuation coefficients (Huisman 1999) for phytoplankton will be employed to better reflect phytoplankton/light interactions and the subsequent effects on phytoplankton growth.

Coupling the physiology-exudation model with a basic 1-D export flux model predicted the underlying patterns of carbon export from the sea surface at two contrasting ocean sites. Despite the significant discrepancy in total volume flux between the simulations and in situ, the ability of the models to accurately characterize the export flux provides confidence that the mechanics of the model are an accurate reflection of the simulated ecosystems. Although only a first step, this model of phytoplankton physiology and exudation provides a basic framework within which changes in cell physiology can be used to better explain the mechanisms that drive sequestration of carbon in the world's oceans.

### 3.4 TABLES

Table 3.1, Table of parameters shown in Figure 3.1.

Cell Model Parameters	Definition
Photosynthesis	Carbon assimilated due to photosynthesis
Biosynthesis	Carbon that can be immediately utilized by the cell
Structure ( $C_L$ )	Cellular carbon respired at each time step (does not vary).
Structure ( $C_S$ )	Cellular carbon dedicated to cell structure
Reserves ( $C_R$ )	Cellular carbon not being immediately utilized by the cell
$f_L$	Inorganic carbon assimilation rate
$f_N$	Inorganic nutrient uptake rate
$F_E$	Exudation rate
$F_{BS}$	Carbon needed for cell structure (from Biosynthesis to Structure)



$F_{PB}$	Carbon needed for Biosynthesis coming from Photosynthesis
$F_{RB}$	Carbon needed for Biosynthesis coming from intra-cellular Reserves
$F_{PR}$	Excess assimilated carbon being moved from Photosynthesis to Reserves

Table 3.2, Table of parameter symbols used in the photosynthesis model. 1 Schofield (pers. comm), 2 (Herzig and Falkowski 1989), 3 Morel and Smith, 1974, 4 (Falkowski and Raven 1997), 5 (Post et al. 1985), 6 Gorbunov (pers. comm.),

Symbol	Model Value	Units	Source
$a^*$	0.01 – 0.025	$\text{m}^2 (\text{mg Chl a})^{-1}$	1
Chl	0.15	$\text{pg (cell)}^{-1}$	2
PQ	1.18	$\text{mol O}_2 \text{ evolved (mol CO}_2 \text{ assimilated)}^{-1}$	2
PAR	$2.374 \times 10^3$	$\text{mol photons m}^{-2} (\text{sec})^{-1}$	3
$\phi_{\text{max}}$	0.18	$\text{mol O}_2 \text{ evolved (mol photons)}^{-1}$	4
$\alpha'$	0.0095	$(\mu\text{mol O}_2 (\text{mg Chl a})^{-1} \text{ min}^{-1}) / (\mu\text{E (m}^2 \text{ sec)}^{-1})$	5
$E_{\mu}$	1500 - 2500	$\mu\text{E (m}^2 \text{ sec)}^{-1}$	
$P_{\text{max}}$	5-7.5	$\mu\text{mol O}_2 (\text{mg Chl a})^{-1} \text{ min}^{-1}$	2

Table 3.3, Cell model results for large and small cells each under high and low light and nutrient conditions.  $\mu_{\max}$  is the maximum growth rate during the model bloom.  $P_{\max}$  is the maximum population size of cells. Bloom Length is the duration of the bloom, and the Maximum Total Cell Carbon Exudation is the maximum fraction of total cellular carbon exuded during the model bloom. Each of these simulations are summarized in Figure 3.3 - Figure 3.10.

	Light	Nutrients	$\mu_{\max}$ (day <sup>-1</sup> )	$P_{\max}$ (cells ml <sup>-1</sup> )	Bloom Length (days)	Total Cell Carbon Exuded (%)
Large Cells	High	High	1.64	4 x 10 <sup>6</sup>	29	12
		Low	1.64	4 x 10 <sup>6</sup>	24	7
	Low	High	1.64	4 x 10 <sup>6</sup>	30	8
		Low	1.22	3 x 10 <sup>6</sup>	24	10
Small Cells	High	High	1.86	8 x 10 <sup>6</sup>	22	17
		Low	1.86	8 x 10 <sup>6</sup>	19	11
	Low	High	1.71	8 x 10 <sup>6</sup>	24	12
		Low	1.71	4 x 10 <sup>6</sup>	20	21

Table 3.4, Growth rate ( $\mu$ ) and sticking efficiency ( $\alpha$ ) values used to couple the phytoplankton physiology/exudation model with a 1-D export flux model at locations characterized by the north central (K2) and tropical (ALOHA) Pacific.

	<b>Station K2</b>		<b>Station ALOHA</b>	
	Large Cell		Large Cell	
	High Light		High Light	
	High Nutrients		High Nutrients	
	$\mu$	$\alpha$	$\mu$	$\alpha$
	(day <sup>-1</sup> )		(day <sup>-1</sup> )	
Exponential Phase	1.64	0	1.86	0.27
Maintenance Phase	0.04	0.08	0	0.57
Senescent Phase	0	0.44	0	0.76

## 3.5 FIGURES

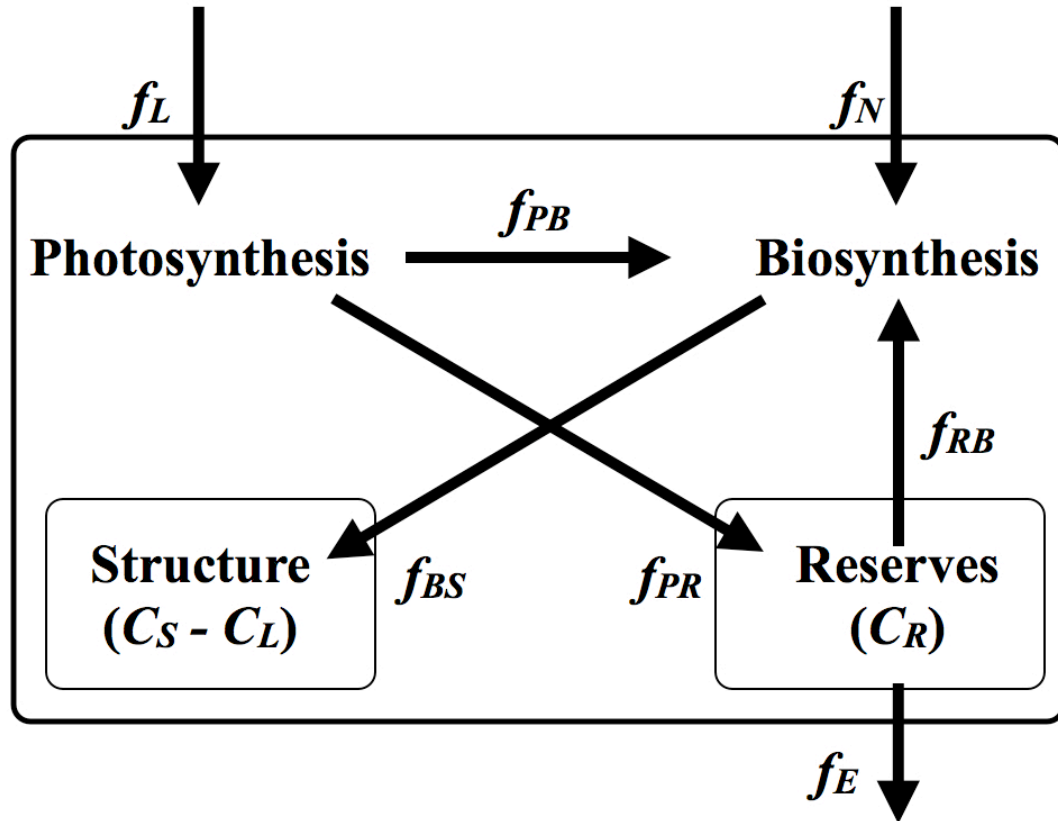


Figure 3.1, The box model of a single cell, assimilating ( $f_L$ ) and releasing ( $f_E$ ) carbon, and taking up nutrients ( $f_N$ ). See Table 3.1 for a list of parameters and symbols.

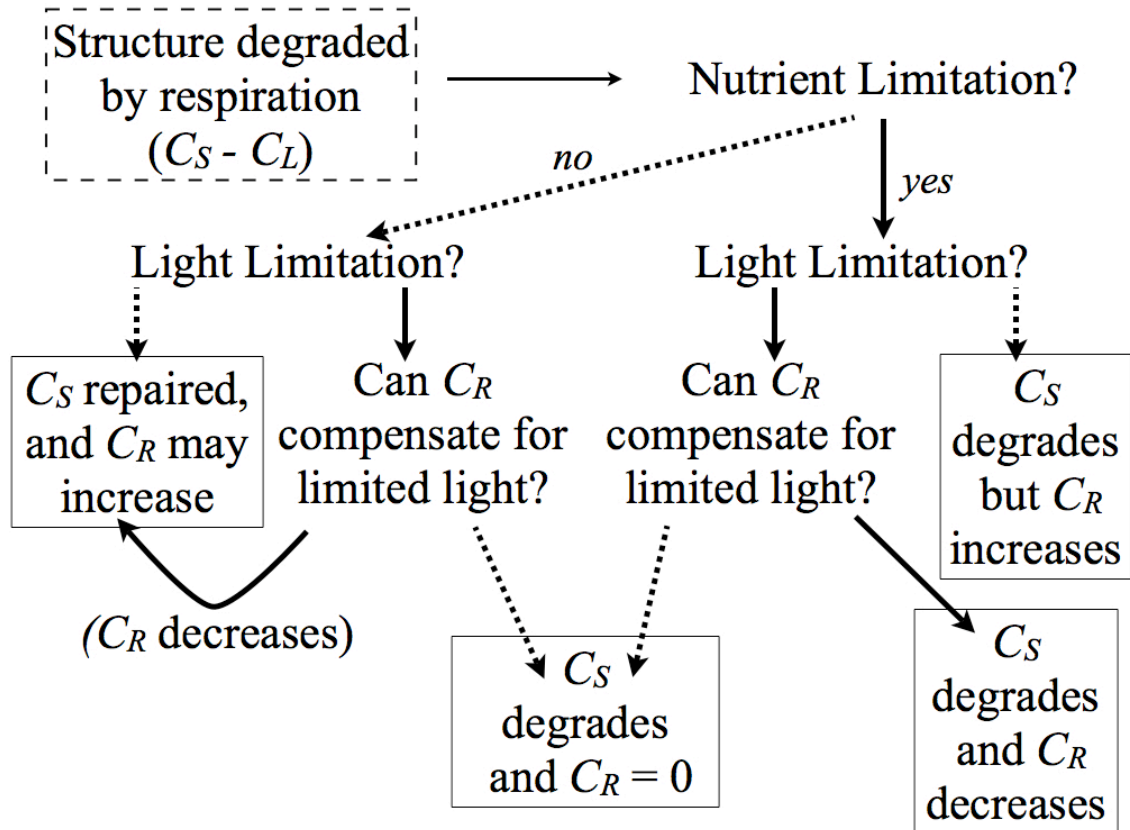


Figure 3.2, The allocation and transfer of intracellular carbon in this model.

The dashed square represents the initiation of each time step. The solid boxes represent the final state of the cell at the end of each time step. Solid arrows indicate a *yes* response and a dashed arrows indicate a *no* response at a given decision point in the model.

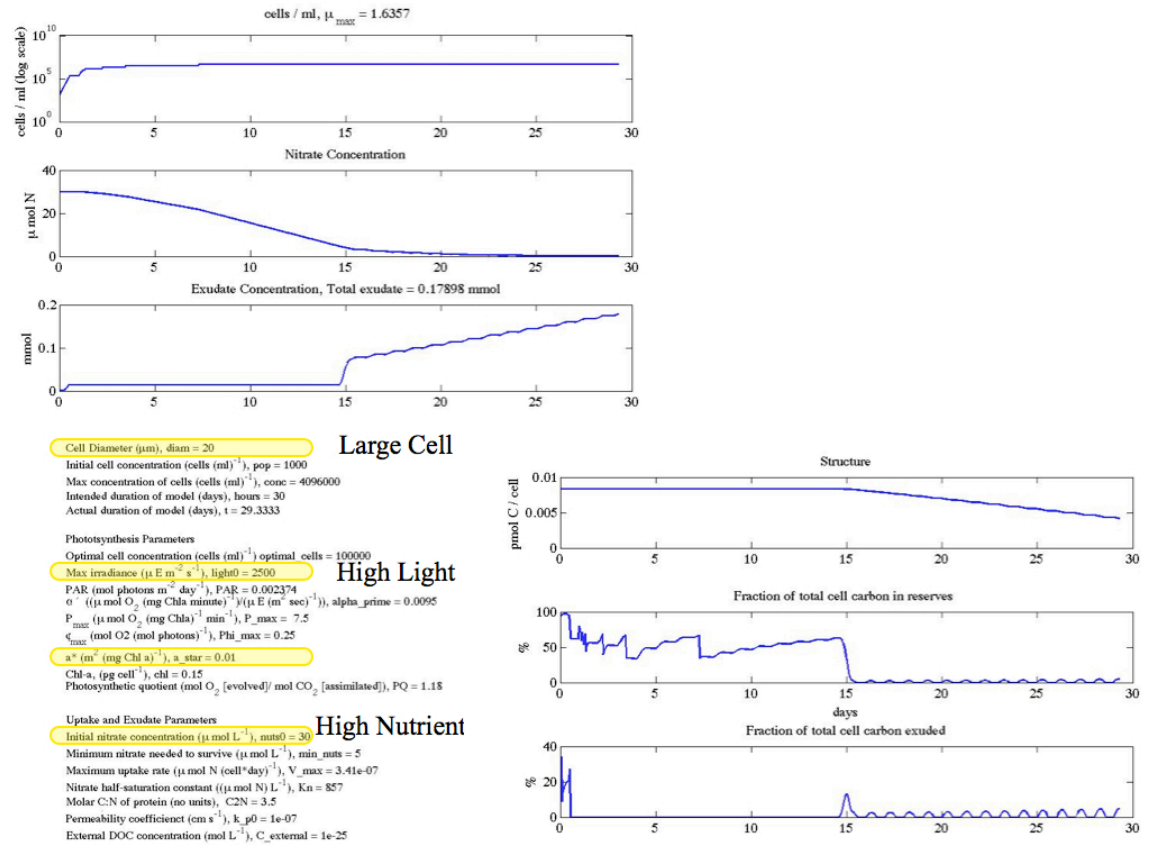


Figure 3.3, Cell Diameter = 20  $\mu\text{m}$ , Initial Light = 2500  $\mu\text{E (m}^2 \text{sec)}^{-1}$  Initial Nutrients = 30  $\mu\text{mol}$ ,  $a^* = 0.025 \text{ m}^2 \text{ (mg Chl a)}^{-1}$

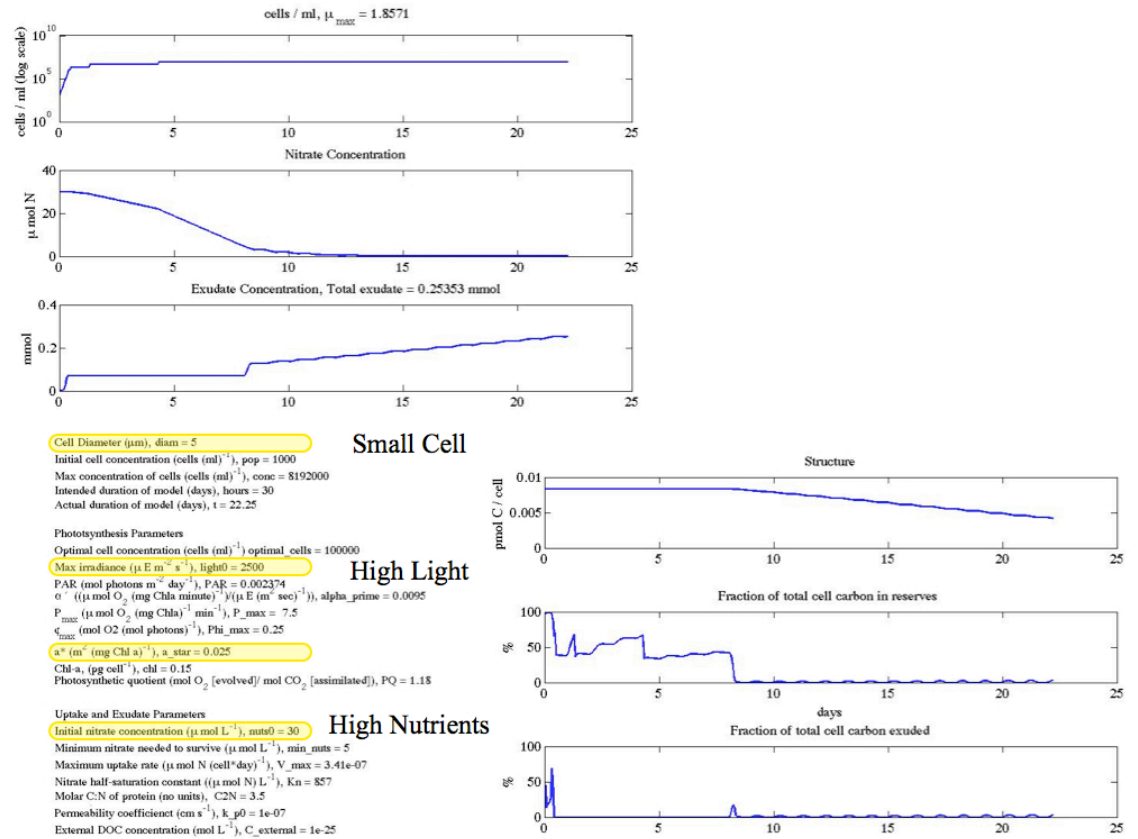


Figure 3.4, Cell Diameter = 5  $\mu\text{m}$ , Initial Light = 2500  $\mu\text{E (m}^2 \text{sec)}^{-1}$  Initial  
Nutrients = 30  $\mu\text{mol}$ ,  $a^* = 0.025 \text{ m}^2 \text{ (mg Chl a)}^{-1}$



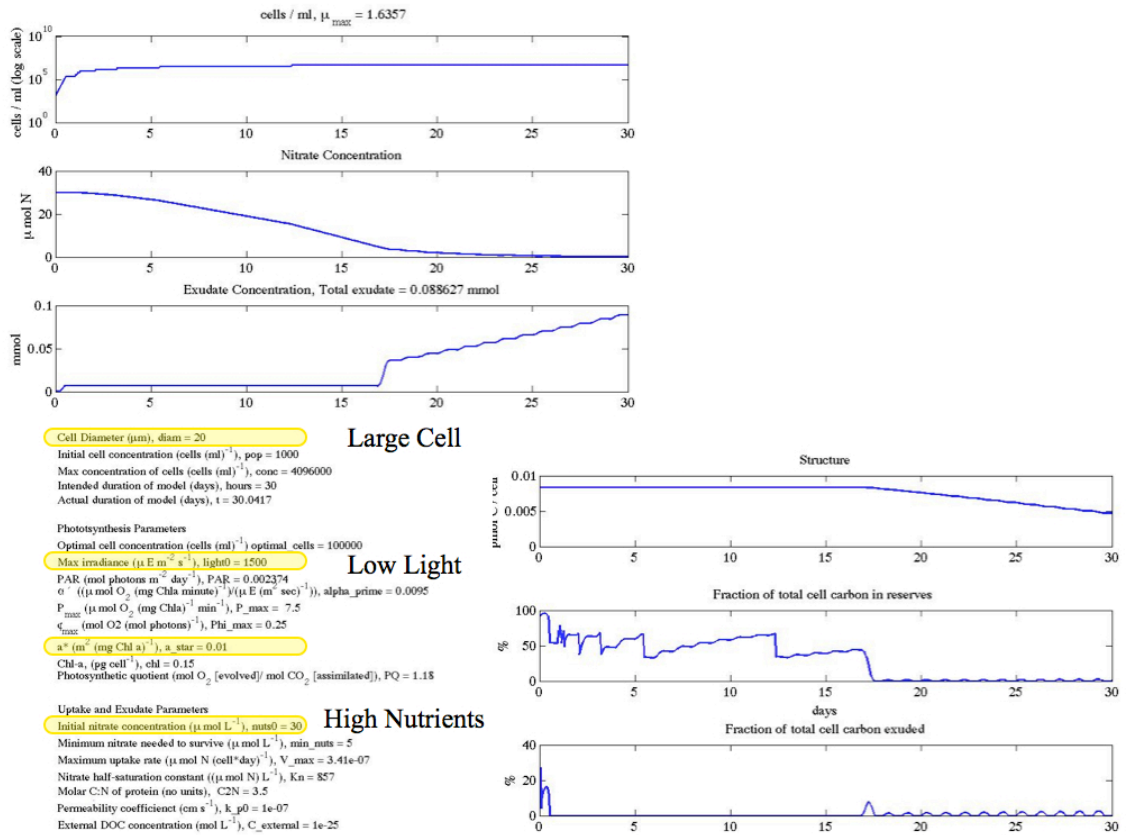


Figure 3.5, Cell Diameter = 20  $\mu\text{m}$ , Initial Light = 1500  $\mu\text{E (m}^2 \text{sec)}^{-1}$  Initial Nutrients = 30  $\mu\text{mol}$ ,  $a^* = 0.025 \text{ m}^2 \text{ (mg Chl a)}^{-1}$

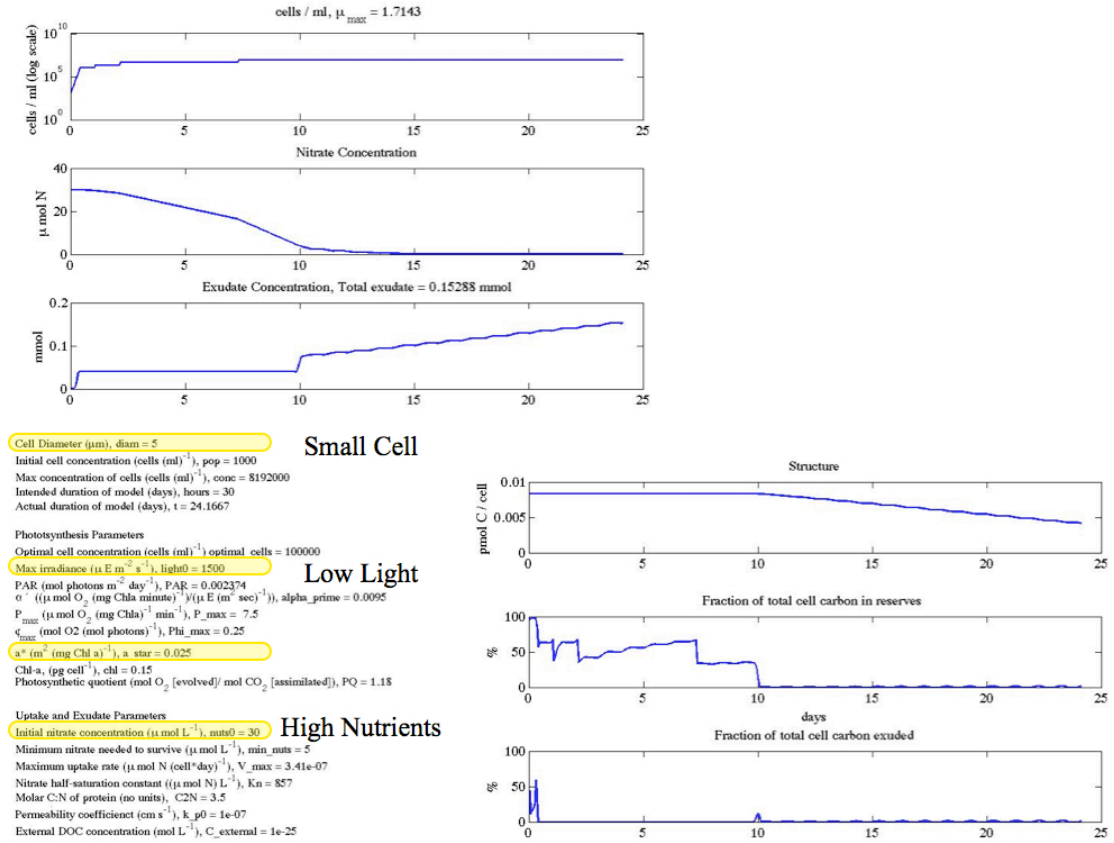


Figure 3.6, Cell Diameter = 5  $\mu\text{m}$ , Initial Light = 1500  $\mu\text{E (m}^2 \text{sec)}^{-1}$  Initial Nutrients = 30  $\mu\text{mol}$ ,  $a^* = 0.025 \text{ m}^2 \text{ (mg Chl a)}^{-1}$

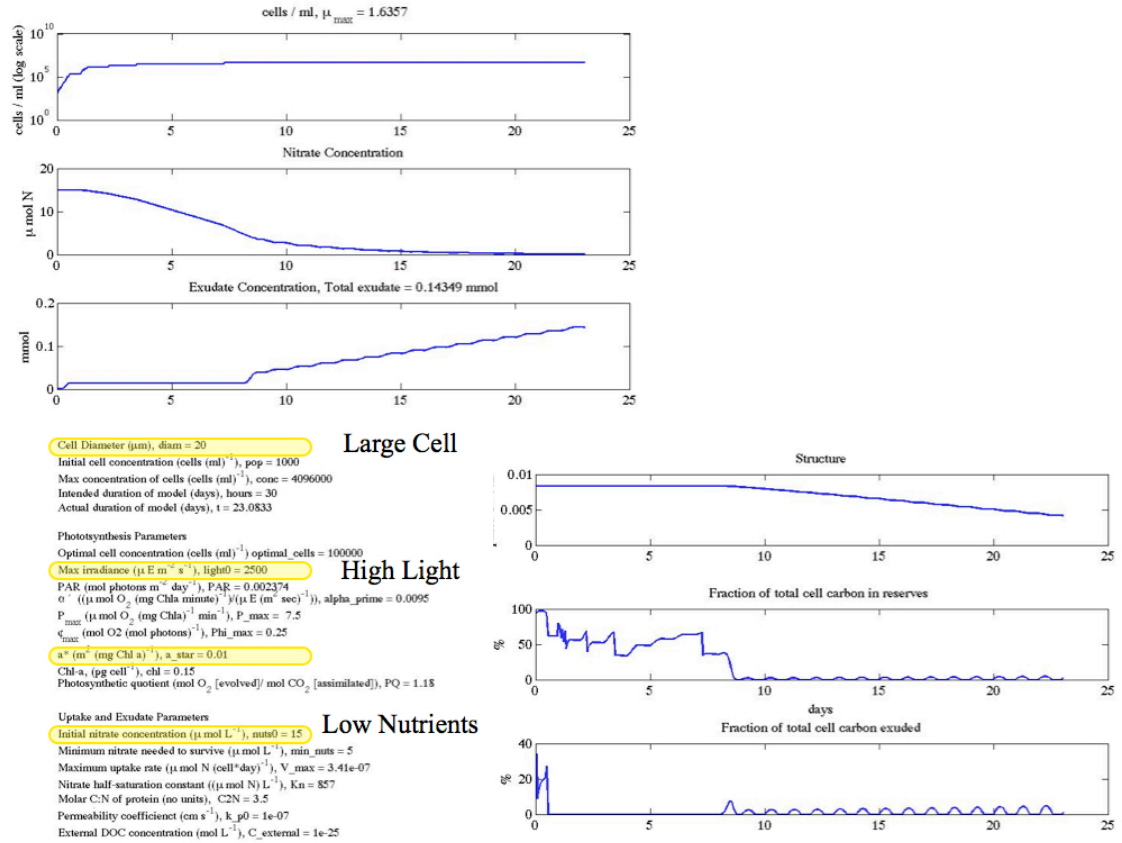
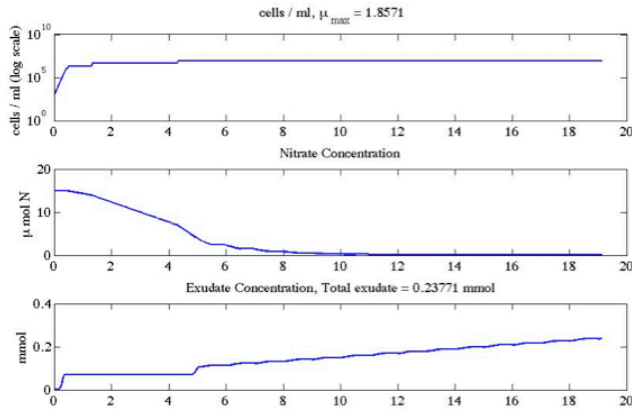


Figure 3.7, Cell Diameter = 20  $\mu\text{m}$ , Initial Light = 2500  $\mu\text{E (m}^2 \text{sec)}^{-1}$  Initial Nutrients = 15  $\mu\text{mol}$ ,  $a^* = 0.025 \text{ m}^2 (\text{mg Chl a})^{-1}$



**Small Cell**

Cell Diameter ( $\mu\text{m}$ ), diam = 5  
 Initial cell concentration (cells  $\text{ml}^{-1}$ ), pop = 1000  
 Max concentration of cells (cells  $\text{ml}^{-1}$ ), conc = 8192000  
 Intended duration of model (days), hours = 30  
 Actual duration of model (days), t = 19.1667

**High Light**

Photosynthesis Parameters  
 Optimal cell concentration (cells  $\text{ml}^{-1}$ ) optimal\_cells = 100000  
 Max irradiance ( $\mu\text{E m}^{-2} \text{s}^{-1}$ ), light0 = 2500  
 PAR (mol photons  $\text{m}^{-2} \text{day}^{-1}$ ), PAR = 0.002374  
 $Q$  ( $\mu\text{mol O}_2$  (mg Chl a  $\text{minute}^{-1}$ )  $(\mu\text{E m}^{-2} \text{sec}^{-1})^{-1}$ ), alpha\_prime = 0.0095  
 $P$  ( $\mu\text{mol O}_2$  (mg Chl a  $\text{min}^{-1}$ ),  $P_{max} = 7.5$   
 $\phi_{max}$  (mol O2 (mol photons  $\text{mol}^{-1}$ ),  $\phi_{max} = 0.25$   
 $a^*$  ( $\text{m}^2$  (mg Chl a  $\text{L}^{-1}$ )),  $a_{star} = 0.025$   
 Chl-a, (pg  $\text{cell}^{-1}$ ), chl = 0.15  
 Photosynthetic quotient (mol O<sub>2</sub> [evolved]/ mol CO<sub>2</sub> [assimilated]), PQ = 1.15

**Low Nutrients**

Uptake and Exudate Parameters  
 Initial nitrate concentration ( $\mu\text{mol L}^{-1}$ ), nitro0 = 15  
 Minimum nitrate needed to survive ( $\mu\text{mol L}^{-1}$ ), min\_nuts = 5  
 Maximum uptake rate ( $\mu\text{mol N (cell}^{-1} \text{day}^{-1})$ ),  $V_{max} = 3.41\text{e-}07$   
 Nitrate half-saturation constant ( $(\mu\text{mol N L}^{-1})$ ),  $K_n = 857$   
 Molar C:N of protein (no units), C2N = 3.5  
 Permeability coefficient ( $\text{cm s}^{-1}$ ),  $k_{p0} = 1\text{e-}07$   
 External DOC concentration ( $\text{mol L}^{-1}$ ),  $C_{external} = 1\text{e-}25$

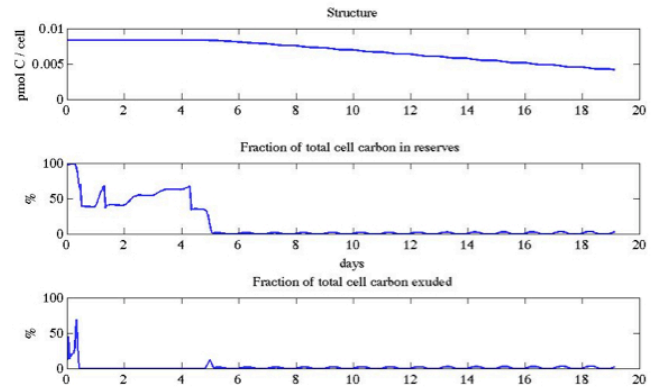


Figure 3.8, Cell Diameter = 5  $\mu\text{m}$ , Initial Light = 2500  $\mu\text{E (m}^2 \text{sec)}^{-1}$  Initial Nutrients = 15  $\mu\text{mol}$ ,  $a^* = 0.025 \text{ m}^2 \text{ (mg Chl a)}^{-1}$

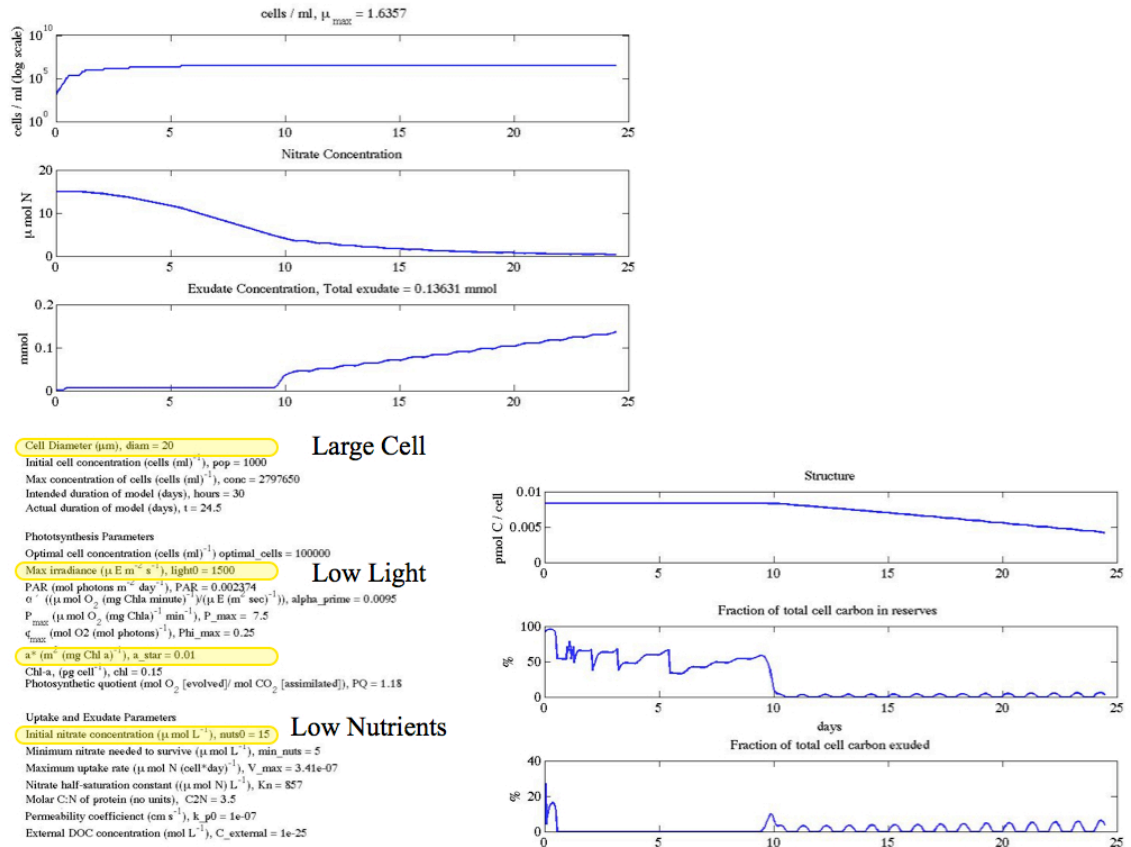


Figure 3.9, Cell Diameter = 20  $\mu\text{m}$ , Initial Light = 1500  $\mu\text{E (m}^2 \text{sec)}^{-1}$  Initial Nutrients = 15  $\mu\text{mol}$ ,  $a^* = 0.025 \text{ m}^2 \text{ (mg Chl a)}^{-1}$

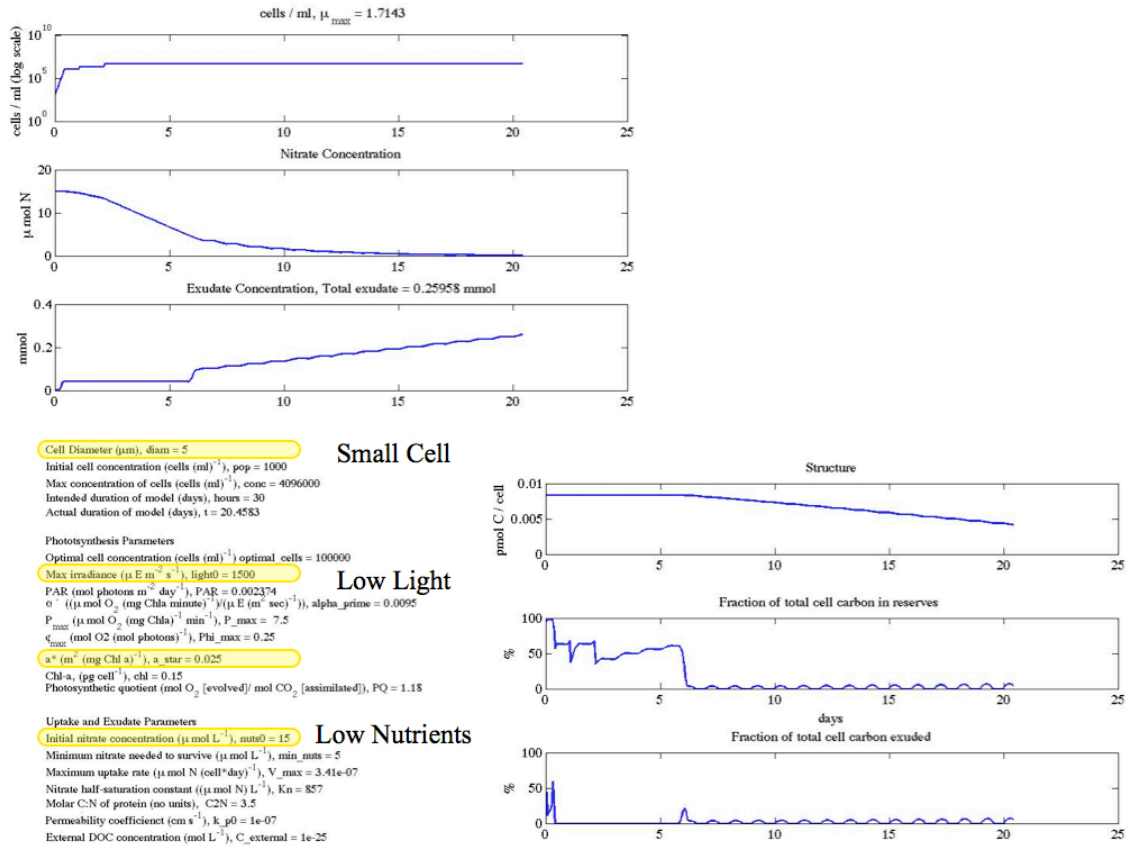


Figure 3.10, Cell Diameter = 5  $\mu\text{m}$ , Initial Light = 1500  $\mu\text{E (m}^2 \text{sec)}^{-1}$  Initial Nutrients = 15  $\mu\text{mol}$ ,  $a^* = 0.025 \text{ m}^2 \text{ (mg Chl a)}^{-1}$

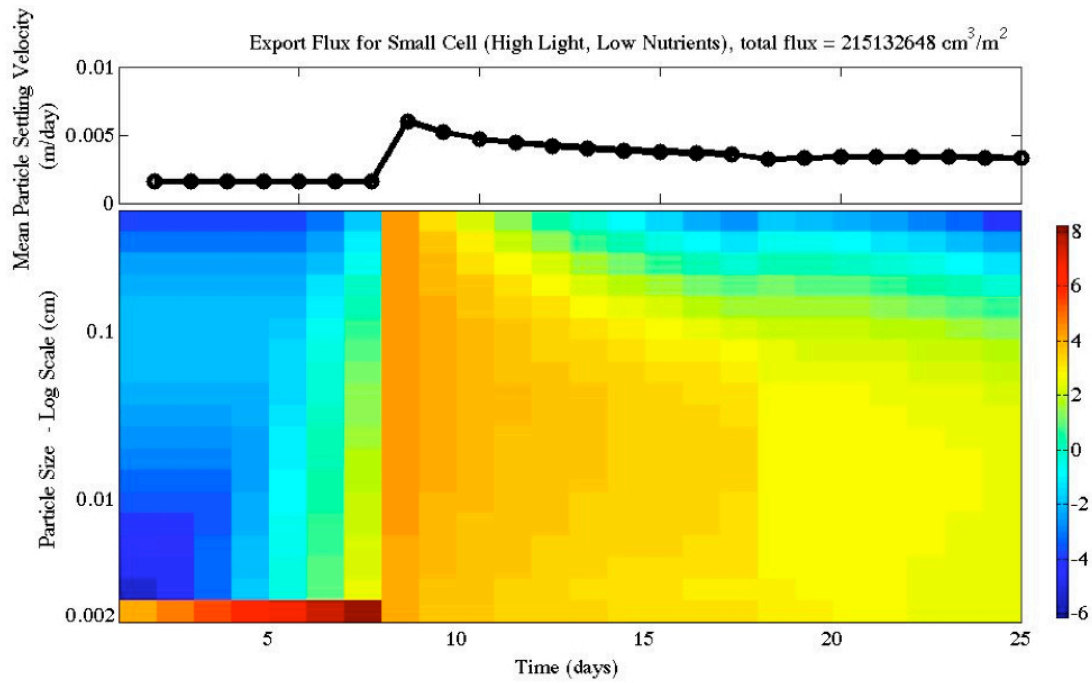


Figure 3.11, Mean particle settling velocity and volume flux spectrum ( $\text{cm}^3 \text{ m}^{-2} \text{ day}^{-1}$ ) over the duration of a model bloom parameterized by station K2 in the north central Pacific.

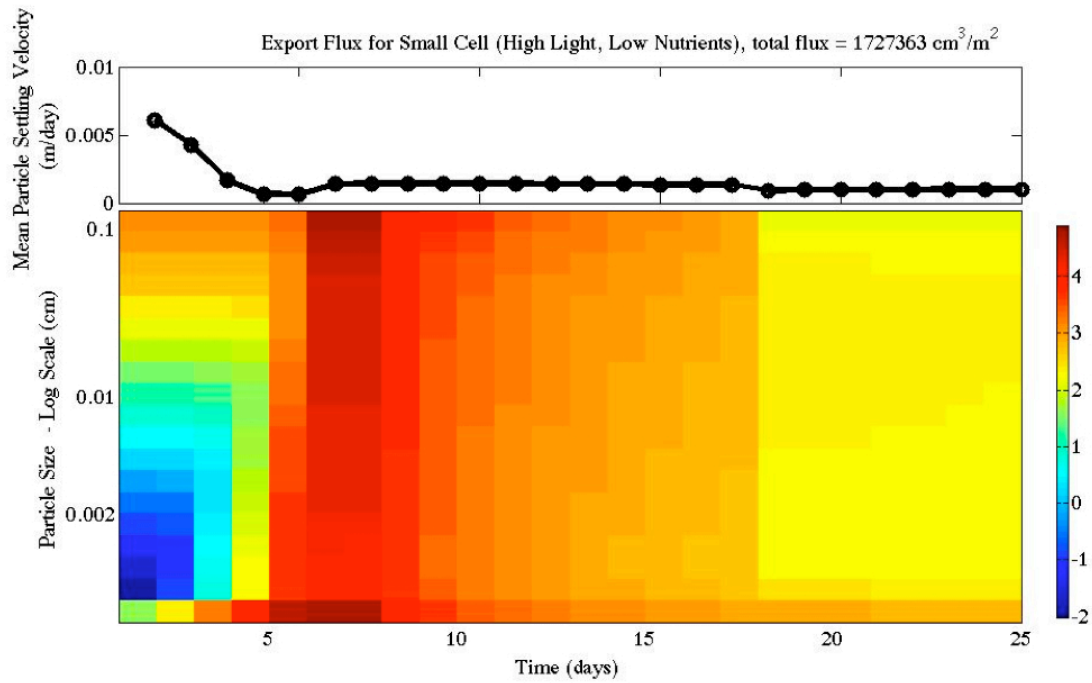


Figure 3.12, Mean particle settling velocity and volume flux spectrum (cm<sup>3</sup> m<sup>-2</sup> day<sup>-1</sup>) over the duration of a model bloom parameterized by station ALOHA in the tropical Pacific.



## Conclusion

The world's oceans harbor the most dynamic and efficient means of natural fixation and long-term carbon sequestration - termed the Biological Pump - of atmospheric carbon dioxide. Yet, while plans abound to sequester atmospheric carbon dioxide by exploiting the biological pump via wide-spread fertilization of the world's oceans, the underlying mechanics driving the efficiency of the Biological Pump are ill-understood. And because the Biological Pump is driven by photosynthetic plankton, these seemingly innocuous single celled plants hold the key to understanding the oceans' role in changing our planet's climate and also in helping to predict the effects of large scale geo-engineering efforts such as carbon sequestration via ocean fertilization. The data in this thesis aimed to improve our understanding of the processes that drive the underlying mechanics of carbon sequestration via the Biological Pump. By employing a new method and an analysis based on long-standing theoretical arguments, the sticking efficiency of algal cells was estimated in situ at low shear. Simultaneously, changes in cell physiology provided a foundation for understanding the role of intra- and inter-cellular processes in driving phytoplankton bloom dynamics. The exudate released as a result of these physiological changes underwent a

documented change in their structure which subsequently influenced their role as the glue behind the formation of phytoplankton aggregates that rapidly settle from the surface to the sediments of the sea. These data reveal the importance of phytoplankton physiology in the downward flux of carbon during phytoplankton bloom succession. From the perception of stress by a single cell to large biogeochemical processes in the ocean, cellular mechanisms that regulate phytoplankton growth and mortality act as a framework for the interplay between the biology and physics of a bloom and its subsequent effects on carbon export in the ocean.

## References

- Ackleh, A. S., T. G. Hallam, and H. C. Muller-Landau. 1995. Estimation of sticking and contact efficiencies in aggregation of phytoplankton: The 1993 SIGMA tank experiment. *Deep Sea Research II* 42: 185-201.
- Allredge, A. L., and C. C. Gotschalk. 1988. In Situ Settling Behavior of Marine Snow. *Limnology and Oceanography* 33: 339-351.
- . 1989. Direct observations of the mass flocculation of diatom blooms: characteristics, settling velocities and formation of diatom aggregates. *Deep Sea Research* 36: 159-171.
- Allredge, A. L., C. C. Gotschalk, U. Passow, and U. Riebesell. 1995. Mass aggregation of diatom blooms: Insights from a mesocosm study. *Deep Sea Research Part II: Topical Studies in Oceanography* 42: 9-27.
- Allredge, A. L., and P. McGillivray. 1991. The attachment probabilities of marine snow and their implications for particle coagulation in the ocean. *Deep Sea Research* 38: 431-443.
- Allredge, A. L., U. Passow, and B. E. Logan. 1993. The abundance and significance of a class of large, transparent, organic particles in the ocean. *Deep Sea Research* 40: 1131-1140.
- Allredge, A. L., and M. W. Silver. 1988. Characteristics, dynamics and significance of marine snow. *Progress in Oceanography* 20: 41-82.
- Azam, F., T. Fenchel, J. G. Field, J. S. Gray, L. A. Meyer-Reil, and F. Thingstad. 1983. The ecological role of water-column microbes in the sea. *Marine Ecology Progress Series* 10: 257-263.
- Belgrano, A., A. P. Allen, B. J. Enquist, and J. F. Gilooly. 2002. Allometric scaling of maximum population density: a common rule for marine phytoplankton and terrestrial plants. *Ecology Letters* 5: 611-613.
- Berman-Frank, I., K. D. Bidle, L. Haramaty, and P. G. Falkowski. 2004. The demise of the marine cyanobacterium, *Trichodesmium* spp., via an autocatalyzed cell death pathway. *Limnology and Oceanography* 49: 997-1005.
- Berman-Frank, I., G. Rosenberg, O. Levitan, L. Haramaty, and X. Mari. 2007. Coupling between autocatalytic cell death and transparent exopolymeric particle production in the marine cyanobacterium *Trichodesmium*. *Environmental Microbiology* 9: 1415-1422.
- Biddanda, B., and R. Benner. 1997. Carbon, Nitrogen, and carbohydrate fluxes during the production of particulate and dissolved organic

- matter by marine phytoplankton. *Limnology and Oceanography* 42: 506-518.
- Bidle, K. D., and P. G. Falkowski. 2004. Cell death in planktonic photosynthetic microorganisms. *Nature Reviews, Microbiology* 2: 643-655.
- Bidle, K. D., L. Haramaty, J. Barcelos E Ramos, and P. G. Falkowski. 2007. Viral activation and recruitment of metacaspases in the unicellular coccolithophore, *Emiliana huxleyi*. *Proceedings of the National Academy of Sciences* 104: 6049-6054.
- Bjørnsen, P. K. 1988. Phytoplankton exudation of organic matter: Why do healthy cells do it? *Limnology and Oceanography* 33: 151-154.
- Brunk, B. K., D. L. Koch, and L. W. Lion. 1998. Observations of coagulation in isotropic turbulence. *Journal of Fluid Mechanics* 371: 81-107.
- Buessler, K. O. and others. 2007. Revisiting carbon flux through the ocean's twilight zone. *Science* 316: 567-570.
- Burd, A. B., and G. A. Jackson. 1997. Predicting particle coagulation and sedimentation rates for a pulsed input. *Journal of Geophysical Research* 102: 10545-10561.
- Busch, P. L., and W. Stumm. 1968. Chemical interactions in the aggregation of bacteria bioflocculation in waste treatment. *Environmental Science and Technology* 2: 49-53.
- Butow, B. J., D. Wynne, and E. Tel Or. 1997. Superoxide dismutase activity in *Peridinium gatunense* in Lake Kinneret: Effect of light regime and carbon dioxide concentration. *Journal of Phycology* 33: 787-793.
- Chin, W. C., M. V. Orellana, I. Quesada, and P. Verdugo. 2004. Secretion in unicellular marine phytoplankton: Demonstration of regulated exocytosis in *Phaeocystis globosa*. *Plant Cell Physiology* 45: 535-542.
- Chin, W. C., M. V. Orellana, and P. Verdugo. 1998. Spontaneous assembly of marine dissolved organic matter into polymer gels. *Nature* 391: 568-572.
- Dam, H. G., and D. T. Drapeau. 1995. Coagulation efficiency, organic-matter glues and the dynamics of particles during a phytoplankton bloom in a mesocosm study. *Deep Sea Research II* 42: 111-123.
- Drapeau, D. T., H. G. Dam, and G. Grenier. 1994. An improved flocculator design for use in particle aggregation experiments. *Limnology and Oceanography* 39: 723-729.
- Engel, A. 2000. The role of transparent exopolymer particles (TEP) in the increase in apparent particle stickiness ( $\alpha$ ) during the decline of a diatom bloom. *Journal of Plankton Research* 22: 485-497.

- Engel, A., S. Thoms, U. Riebesell, E. Rochelle-Newall, and I. Zondervan. 2004. Polysaccharide aggregation as a potential sink of marine dissolved organic carbon. *Nature* 428: 929-932.
- Field, C. B., M. J. Behrenfeld, J. T. Randerson, and P. G. Falkowski. 1998. Primary Production of the biosphere: Integrating terrestrial and oceanic components. *Science* 281: 237-240.
- Flynn, K. J., and V. Martin-Jézéquel. 2000. Modeling Si-N-limited growth of diatoms. *Journal of Plankton Research* 22: 447-472.
- Fogg, G. E. 1962. Extracellular Products, p. 475-491. *In* R. A. Lewin [ed.], *Physiology and Biochemistry of Algae*. Academic Press.
- Fogg, G. E., C. Nalewajko, and W. D. Watt. 1965. Extracellular products of phytoplankton photosynthesis. *Proc. R. Soc. Lond. B, Biological Sciences* 161: 517-534.
- Fowler, S. W., and G. A. Knauer. 1986. Role of large particles in the transport of elements and organic compounds through the oceanic water column. *Progress in Oceanography* 16: 147-194.
- Geider, R. J., H. L. Macintyre, and T. M. Kana. 1998. A dynamic regulatory model of phytoplankton acclimation to light, nutrients, and temperature. *Limnology and Oceanography* 43: 679-694.
- Gelbard, F., Y. Tambour, and J. H. Seinfeld. 1980. Sectional representations for simulating aerosol dynamics. *Journal of Colloid and Interface Science* 76: 541-556.
- Gibbs, J. R. 1982. Floc stability during Coulter counter analysis. *Journal of Sedimentary Petrology* 52: 657-670.
- Gorbunov, M. Y., and P. G. Falkowski. 2004. Fluorescence induction and relaxation (FIRE) technique and instrumentation for monitoring photosynthetic processes and primary production in aquatic ecosystems. *In* A. van der Est and D. Bruce [eds.], *Proc. 13th International Congress of Photosynthesis*, Aug.29-Sept.3, 2004. Allen Press.
- Guillard, R. R. L., and P. J. Wangersky. 1958. The production of extracellular carbohydrates by some marine flagellates. *Limnology and Oceanography* 3: 449-454.
- Hansen, J. L. S., and T. Kiørboe. 1997. Quantifying interspecific coagulation efficiency of phytoplankton. *Marine Ecology Progress Series* 159: 75-79.
- Hellebust, J. A. 1974. Extracellular products, p. 838-863. *In* W. D. P. Stewart [ed.], *Algal Physiology and Biochemistry*. University of California Press.

- Hentschel, B. T. 2004. Sediment resuspension and boundary layer flow dramatically increase the growth rates of interface-feeding spionid polychaetes. *Journal of Marine Systems* 49: 209-224.
- Herzig, R., and P. G. Falkowski. 1989. Nitrogen limitation in *Isochrysis galbana* (Haptophyceae). I. Photosynthetic energy conversion and growth efficiencies. *Journal of Phycology* 25: 462-471.
- Hill, P. S. 1992. Reconciling aggregation theory with observed vertical fluxes following phytoplankton blooms. *Journal Geophysical Research* 97: 2295-2308.
- Hill, P. S., and A. R. M. Nowell. 1990. The potential role of large, fast-sinking particles in cleaning nepheloid layers: discussion. *Philosophical Transactions of the Royal Society of London: A, Mathematical and Physical Sciences* 331: 103-117.
- Hoagland, K. D., J. R. Rosowski, M. R. Gretz, and S. C. Roemer. 1993. Diatom extracellular polymeric substances: function, fine structure, chemistry, and physiology. *Journal of Phycology* 29: 537-566.
- Huisman, J. 1999. Population dynamics of light-limited phytoplankton: Microcosm experiments. *Ecology* 80: 202-210.
- Hunt, J. R. 1980a. Coagulation in continuous particle size distributions; theory and experimental verification. PhD. thesis, Cal-Tech.
- . 1980b. Particulates in Water: Characterization, fate, effects, and removal. *In* M. C. Kavanaugh and J. O. Leckie [eds.]. *Advances in Chemistry Series*. American Chemical Society.
- . 1980c. Particulates in Water: Characterization, fate, effects, and removal. *In* M. C. Kavanaugh and J. O. Leckie [eds.]. American Chemical Society.
- . 1982. Self-similar particle-size distributions during coagulation: theory and experimental verification. *Journal Fluid Mechanics* 122: 169-185.
- Jackson, G. A. 1990. A model of the formation of marine algal flocs by physical coagulation processes. *Deep Sea Research* 37: 1197-1211.
- . 2005. Flocculation in Natural and Engineered Environmental Systems, p. 271-292. *In* I. Droppo, G. Leppard, S. Liss and T. Milligan [eds.]. CRC Press.
- Jackson, G. A., and A. B. Burd. 1998. Aggregation in the marine environment. *Environmental Science and Technology* 32: 2805-2814.
- Jackson, G. A., and S. E. Lochmann. 1992. Effect of coagulation on nutrient and light limitation of an algal bloom. *Limnology and Oceanography* 37: 77-89.
- . 1993. Environmental Particles, p. 387-414. *In* J. Buffle and H. P. van Leeuwen [eds.]. Lewis Publishers.

- Jackson, G. A., A. Waite, and P. W. Boyd. 2005. Role of algal aggregation in vertical carbon export during SOIREE and in other low biomass environment. *Geophysical Research Letters* 32: 1-4.
- Jenkinson, I. R. 1986. Oceanographic implications of non-Newtonian properties found in phytoplankton cultures. *Nature* 323: 435-437.
- Jensen, L. M. 1983. Phytoplankton release of extracellular organic carbon, molecular weight composition, and bacterial assimilation. *Marine Ecology Progress Series* 11: 39-48.
- Kahl, L. A., A. Vardi, and O. Schofield. 2008. Effects of phytoplankton physiology on export flux. *Marine Ecology Progress Series* 354: 3-19.
- Karl, D. M. and others 1996. Seasonal and interannual variability in primary production and particle flux at Station ALOHA. *Deep Sea Research II* 43: 539-568.
- Karner, M., and G. J. Herndl. 1992. Extracellular enzymatic activity and secondary production in free-living and marine-snow-associated bacteria. *Marine Biology* 113: 1432-1793.
- Karp-Boss, L., and P. A. Jumars. 1998. Motion of diatoms chains in steady shear flow. *Limnology and Oceanography* 43: 1767-1773.
- Kjørboe, T., K. P. Andersen, and H. G. Dam. 1990. Coagulation efficiency and aggregate formation in marine phytoplankton. *Marine Biology* 107: 235-245.
- Kjørboe, T., and J. L. S. Hansen. 1993. Phytoplankton aggregate formation: observations of patterns and mechanisms of cell sticking and the significance of exopolymeric material. *Journal Plankton Research* 15: 993-1018.
- Kjørboe, T., C. Lundsgaard, M. Olesen, and J. L. S. Hansen. 1994. Aggregation and sedimentation processes during a spring phytoplankton bloom: A field experiment to test coagulation theory. *Journal Marine Research* 52: 297-323.
- Kjørboe, T., P. Tiselius, B. Mitchell-Innes, J. L. S. Hansen, A. W. Visser, and X. Mari. 1998. Intensive aggregate formation with low vertical flux during an upwelling-induced bloom. *Limnology and Oceanography* 43: 104-116.
- Klausmeier, C. A., E. Litchman, T. Daufresne, and S. A. Levin. 2004. Optimal nitrogen-to-phosphorus stoichiometry of phytoplankton. *Nature* 429: 171-174.
- Kolber, Z. S., and P. G. Falkowski. 1993. Use of active fluorescence to estimate phytoplankton photosynthesis in situ. *Limnology and Oceanography* 38: 1646-1665.

- Leandro, S. M., M. C. Gil, and I. Delgadillo. 2003. Partial characterisation of exopolysaccharides exudated by planktonic diatoms maintained in batch cultures. *Acta Oecologica* 24: S49-S55.
- Leppard, G. G. 1995. The characterization of algal and microbial mucilages and their aggregates in aquatic systems. *The Science of the Total Environment* 165: 103-131.
- Li, X., and B. E. Logan. 1995. Size distributions and fractal properties of particles during a simulated phytoplankton bloom in a mesocosm. *Deep Sea Research Part II: Topical Studies in Oceanography* 42: 125-138.
- Logan, B. E., and J. R. Kilps. 1995. Fractal dimensions of aggregates formed in different fluid mechanical environments. *Water Research* 29: 443-453.
- Martin, J. H., G. A. Knauer, D. M. Karl, and W. W. Broenkow. 1987. VERTEX: carbon cycling in the northeast Pacific. *Deep Sea Research* 34: 267-285.
- McCave, I. N. 1984. Size spectra and aggregation of suspended particles in the deep ocean. *Deep Sea Research* 31: 329-352.
- Moeseneder, M. M., and G. J. Herndl. 1995. Influence of turbulence on bacterial production in the sea. *Limnology and Oceanography* 40: 1466-1473.
- Myklestad, S. 1974. Production of carbohydrates by marine planktonic diatoms. I. Comparison of nine different species in culture. *Journal of Experimental Marine Biology and Ecology* 15: 261-274.
- . 1995. Release of extracellular products by phytoplankton with special emphasis on polysaccharides. *The Science of the Total Environment* 165: 155-164.
- Myklestad, S., and A. Haug. 1972. Production of carbohydrates by the marine diatom *Chatoceros afinis* var. *willei* (Gran) Hustedt. I Effect of the concentration of nutrients in the culture medium. *Journal Experimental Marine Biology and Ecology* 9: 122-136.
- Nagata, T. 2000. Microbial Ecology of the Oceans, p. 121-152. *In* D. L. Kirchman [ed.]. Wiley-Liss.
- Nalewajko, C., and D. R. S. Lean. 1972. Growth and excretion in planktonic algae and bacteria. *Journal Phycology* 8: 361-366.
- Passow, U. 2000. Formation of transparent exopolymer particles, TEP, from dissolved precursor material. *Marine Ecology Progress Series* 192.
- Passow, U., and A. L. Alldredge. 1995a. A dye binding assay for the spectrophotometric measurement of transparent exopolymer particles (TEP). *Limnology and Oceanography* 40: 1326-1335.



- . 1995b. Aggregation of a diatom bloom in a mesocosm: the role of transparent exopolymer particles (TEP). *Deep Sea Research II* 42: 99-109.
- Passow, U., A. L. Alldredge, and B. E. Logan. 1994. The role of particulate carbohydrate exudates in the flocculation of diatom blooms. *Deep Sea Research I* 41: 335-357.
- Petersen, J. E., L. P. Sanford, and W. M. Kemp. 1998. Coastal plankton response to turbulent mixing in experimental ecosystems. *Marine Ecology Progress Series* 171: 23-41.
- Porter, K. G., and Y. S. Feig. 1980. The use of DAPI for identifying and counting aquatic microflora. *Limnology and Oceanography* 25: 943-948.
- Post, A. F., Z. Dubinsky, K. Wyman, and P. G. Falkowski. 1985. Physiological responses of a marine planktonic diatom to transitions in growth irradiance. *Marine Ecology Progress Series* 25: 141-149.
- Prieto, L. and others 2002. Scales and processes in the aggregation of diatom blooms: high time resolution and wide size range records in a mesocosm study. *Deep Sea Research* 49: 1233-1253.
- Ramus, J., and B. E. Kenney. 1989. Shear degradation as a probe of microalgal exopolymer structure and rheological properties. *Biotechnology and Bioengineering* 34: 1203-1208.
- Ramus, J., and D. M. Robins. 1974. The correlation of Golgi activity and polysaccharide activity in *Porphyridium*. *Journal of Phycology* 11: 70-74.
- Raven, J. A. 1984. *Energetics and Transport in Aquatic Plants*. Krieger Publishing Company.
- Riebesell, U. 1991. Particle aggregation during a diatom bloom. I. Physical aspects. *Marine Ecology Progress Series* 69: 273-280.
- . 1992. The formation of large marine snow and its sustained residence in surface waters. *Limnology and Oceanography* 37: 63-76.
- Santschi, P. H., E. Balnois, K. J. Wilkinson, J. Z. Zhang, J. Buffle, and L. Guo. 1998. Fibrillar polysaccharides in marine macromolecular organic material as imaged by atomic force microscopy and transmission electron microscopy. *Limnology and Oceanography* 43: 896-908.
- Segovia, M., L. Haramaty, J. A. Berges, and P. G. Falkowski. 2003. Cell Death in the Unicellular Chlorophyte *Dunaliella tertiolecta*. A Hypothesis on the Evolution of Apoptosis in Higher Plants and Metazoans. *Plant Physiology* 132: 99-105.

- Seuront, L., D. Vincent, and J. G. Mitchell. 2006. Biologically induced modification of seawater viscosity in the Eastern English Channel during a *Phaeocystis globosa* spring bloom. *Journal of Marine Systems* 61: 118-133.
- Smith, D. C., M. Simon, A. L. Alldredge, and F. Azam. 1992. Intense hydrolytic enzyme activity on marine aggregates and implications for rapid particle dissolution. *Nature* 359: 139-142.
- Smith, D. C., G. F. Steward, R. A. Long, and F. Azam. 1995. Bacterial mediation of carbon fluxes during a diatom bloom in a mesocosm. *Deep Sea Research Part II: Topical Studies in Oceanography* 42: 75-97.
- Smith, D. F., and W. J. Wiebe. 1976. Constant release of photosynthate from marine phytoplankton. *Applied and Environmental Microbiology* 32: 75-79.
- Spoher, H. A., and H. W. Milner. 1949. The chemical composition of chlorella; effect of environmental conditions. *Plant Physiology* 24: 120-149.
- Stadelmann, E. J. 1962. Permeability, p. 493-528. *In* R. A. Lewin [ed.], *Physiology and Biochemistry of Algae*. Academic Press.
- Steinberg, D. K., C. A. Carlson, N. R. Bates, R. J. Johnson, A. F. Michaels, and A. H. Knap. 2001. Overview of the US JGOFS Bermuda Atlantic Time-series Study (BATS): a decade-scale look at ocean biology and biogeochemistry. *Deep Sea Research II*.
- Synytsya, A., J. Copikova, P. Matejka, and V. Machovic. 2003. Fourier transform Raman and infrared spectroscopy of pectins. *Carbohydrate Polymers* 54: 97-106.
- Turner, J. T. 2002. Zooplankton fecal pellets, marine snow and sinking phytoplankton blooms. *Aquatic Microbial Ecology* 27: 57-102.
- Urbani, R., E. Magaletti, P. Sist, and A. M. Cicero. 2005. Extracellular carbohydrates released by the marine diatoms *Cylindrotheca closterium*, *Thalassiosira pseudonana* and *Skeletonema costatum*: Effect of P-depletion and growth status. *Science of the Total Environment* 353: 300-306.
- Vardi, A., I. Berman-Frank, T. Rozenberg, O. Hadas, A. Kaplan, and A. Levine. 1999. Programmed cell death of the dinoflagellate *Peridinium gatunense* is mediated by CO<sub>2</sub> limitation and oxidative stress. *Current Biology* 9: 1061-1064.
- Vardi, A. and others 2007. Synchronization of cell death in a dinoflagellate population is mediated by an excreted thiol protease. *Environmental Microbiology* 9: 360-369.

- Waite, A., S. Gallagher, and H. G. Dam. 1997. New measurements of phytoplankton aggregation in a flocculator using videography and image analysis. *Marine Ecology Progress Series* 155: 77-88.
- Waite, A., and S. Nodder. 2001. The effect of in situ iron addition on the sinking rates and export flux of Southern Ocean diatoms. *Deep Sea Research II* 48: 2635-2654.
- Waite, A., R. J. Olson, H. G. Dam, and U. Passow. 1995. Sugar-containing compounds on the cell surfaces of marine diatoms measured using concanavalin a and flow cytometry. *Journal Phycology* 31: 925-933.
- Watt, W. D. 1966. Release of dissolved organic material from the cells of phytoplankton populations. *Proc. R. Soc. Lond. B* 164: 521-551.
- Wolfe-Simon, F., V. Starovoytov, J. Reinfelder, O. Schofield, and P. G. Falkowski. 2006. Localization and role of manganese superoxide dismutase in a marine diatom. *Plant Physiology* 142: 1701-1709.
- Zlotnik, I., and Z. Dubinsky. 1989. The effect of light and temperature on DOC excretion by phytoplankton. *Limnology and Oceanography* 34: 831-839.

## Curriculum Vitae

Leonard Alexander Kahl Jr.

### EDUCATION

1997 – 2001	B.S., Hydrologic Sciences, University of California, Santa Barbara
1997 – 2001	B.A., Geography, University of California, Santa Barbara
2002 – 2008	PhD., Rutgers University, New Brunswick, NJ

### EMPLOYMENT

2002	Cashier/Clerk, Nature's Oasis Health Foods, Durango, CO
2002 – 2008	Graduate/Teaching Assistant, Rutgers University, New Brunswick, NJ
2005 – 2008	Webmaster, Rutgers Graduate Program in Oceanography, New Brunswick, NJ
2006 – 2008	Webmaster, Rutgers Energy Institute, New Brunswick, NJ
2007 – 2008	Poll Worker, New York City Board of Elections, New York, NY

### PUBLICATIONS

Kahl, L.A., A. Vardi, O. Schofield. 2008. *Effects of phytoplankton physiology on export flux*. Marine Ecology Progress Series, 354 p. 3 – 19.